

The Effects of Annealing URu_2Si_2 on the Resistivity and Meissner Effect

by

Yang Pan

B.Sc.(Honours) First Class, Nottingham Trent University, 2007

A THESIS SUBMITTED IN PARTIAL FULFILMENT OF
THE REQUIREMENTS FOR THE DEGREE OF

MASTER OF SCIENCE

in

The Faculty of Mathematics and Sciences

Department of Physics



BROCK UNIVERSITY

August 16, 2012

2012 © Yang Pan

In presenting this thesis in partial fulfilment of the requirements for an advanced degree at the Brock University, I agree that the Library shall make it freely available for reference and study. I further agree that permission for extensive copying of this thesis for scholarly purposes may be granted by the head of my department or by his or her representatives. It is understood that copying or publication of this thesis for financial gain shall not be allowed without my written permission.

(Signature) _____

Department of Physics

Brock University
St.Catharines, Canada

Date _____

Abstract

The enigmatic heavy fermion URu₂Si₂, which is the subject of this thesis, has attracted intensive theoretical and experimental research since 1984 when it was firstly reported by Schlitz *et al.* at a conference [1]. The previous bulk property measurements clearly showed that one second order phase transition occurs at the Hidden Order temperature $T_{HO} \approx 17.5 \text{ K}$ and another second order phase transition, the superconducting transition, occurs at $T_c \approx 1 \text{ K}$. Though twenty eight years have passed, the mechanisms behind these two phase transitions are still not clear to researchers.

Perfect crystals do not exist. Different kinds of crystal defects can have considerable effects on the crystalline properties. Some of these defects can be eliminated, and hence the crystalline quality improved, by annealing. Previous publications showed that some bulk properties of URu₂Si₂ exhibited significant differences between as-grown samples and annealed samples. The present study shows that the annealing of URu₂Si₂ has some considerable effects on the resistivity and the DC magnetization. The effects of annealing on the resistivity are characterized by examining how the Residual Resistivity Ratio (RRR), the fitting parameters to an expression for the temperature dependence of the resistivity, the temperatures of the local maximum and local minimum of the resistivity at the Hidden Order phase transition and the Hidden Order Transition Width ΔT_{HO} change after annealing. The plots of one key fitting parameter, the onset temperature of the Hidden Order transition and ΔT_{HO} vs RRR are compared with those of Matsuda *et al.* [2]. Different media used to mount samples have some impact on how effectively the samples are cooled because the media have different thermal conductivity.

The DC magnetization around the superconducting transition is presented for one unannealed sample under fields of 25 *Oe* and 50 *Oe* and one annealed sample under fields of 0 *Oe* and 25 *Oe*. The DC field dependent magnetization of the annealed Sample1-1 shows a typical field dependence of a Type-II superconductor. The lower critical field H_{c1} is relatively high, which may be due to

flux pinning by the crystal defects.

Contents

Abstract	ii
Contents	iv
List of Tables	vii
List of Figures	viii
Acknowledgements	xii
1 Basic Review of URu₂Si₂	1
1.1 Space Group of URu ₂ Si ₂	1
1.2 Resistivity of URu ₂ Si ₂	2
1.3 Susceptibility of URu ₂ Si ₂	4
1.3.1 DC Susceptibility	4
1.3.2 AC Susceptibility	4
1.3.3 Elastic Neutron Scattering	6
1.3.4 Inelastic Neutron Scattering	7
1.4 Specific Heat Capacity of URu ₂ Si ₂	9
1.5 Optical Measurements of URu ₂ Si ₂	11
2 Defects in Crystals	15
2.1 Point Defects	15
2.1.1 Vacancies	16
2.1.2 Interstitial Defects	17
2.1.3 Frenkel Defect	17

2.1.4	Schottky Defect	18
2.1.5	Impurity	18
2.1.6	Phonon	19
2.1.7	Methods to create point defects	20
2.2	Line defects	20
2.2.1	Burgers Vector	20
2.2.2	Edge Dislocation	21
2.2.3	Screw Dislocation	22
2.3	Surface defects	24
2.3.1	External Surface Defects	24
2.3.2	Grain Boundaries	24
2.3.3	Twin Boundaries	27
2.3.4	Stacking Faults	27
2.4	Volume Defects	29
2.5	Czochralski Process	29
3	Annealing Samples	31
3.1	Annealing Mechanisms	31
3.1.1	Strain Energy	31
3.1.2	Recovery	32
3.1.3	Recrystallization	35
3.1.4	Grain Growth	38
3.1.5	Various Annealing Processes	42
3.2	Review of Annealing Effects on URu_2Si_2	43
4	^3He Refrigerator	49
5	Resistivity Measurement	54
5.1	Van der Pauw Method	54
5.1.1	Four Contacts in One Dimension	54

5.1.2	Four Contacts in Two Dimensions	57
5.1.3	f factor in Van der Pauw theorem	59
5.2	Experimental Methods	62
5.3	Experimental Results	66
5.4	Some Other Models of Resistivity	79
6	DC Magnetization Measurement at SC Transition	80
6.1	Meissner Effect	80
6.2	Type-I superconductor and Type-II superconductor	86
6.3	Josephson effect	88
6.4	Superconducting Quantum Interference Device	91
6.5	Experimental Methods	93
6.6	Experimental Results	94
7	Conclusions	100
	Bibliography	102

List of Tables

3.1	Effects of atomic 0.01% impurity on the recrystallization temperature of pure copper [29, p. 240]	38
3.2	Annealing Effects on Resistivity of URu ₂ Si ₂ [33]	44
5.1a	RRR, fitting parameters, local maximum and local minimum at HO and ΔT_{HO} . . .	77
5.1b	RRR, fitting parameters, local maximum and local minimum at HO and ΔT_{HO} CONT.	78

List of Figures

1.1	Crystal Structure of URu ₂ Si ₂ [5]	1
1.2	Resistivity vs Temperature for single crystal URu ₂ Si ₂ [10]	3
1.3	Low Temperature Resistivity for single crystal URu ₂ Si ₂ [10]	3
1.4	DC Susceptibility and $\frac{1}{\chi_{DC}}$ for single crystal URu ₂ Si ₂ [8]	4
1.5	Upper critical field $\mu_0 H_{c2}$ and AC susceptibility for single crystal URu ₂ Si ₂ [8] . . .	5
1.6	Hysteresis magnetization loop for single crystal URu ₂ Si ₂ [8]	5
1.7	Temperature-dependent AFM moment of URu ₂ Si ₂ under hydrostatic pressure [11] .	6
1.8	Pressure-Temperature phase diagram of URu ₂ Si ₂ [11]	7
1.9a	Inelastic scattering above T_{HO} [13]	8
1.9b	Inelastic scattering below T_{HO} [13]	8
1.10	Shifts of resonance frequencies from normal state to superconducting state in single crystal URu ₂ Si ₂ [14]	9
1.11	Specific heat capacity for polycrystal URu ₂ Si ₂ [8]	10
1.12	Magnetic Entropy S_{mag} vs Antiferromagnetic Moment μ_{ord} for some heavy fermions [15]	11
1.13a	Real part of optical conductivity above T_{HO} for single crystal URu ₂ Si ₂ [16]	11
1.13b	Real part of optical conductivity below T_{HO} for single crystal URu ₂ Si ₂ [16]	12
1.14	Real part of optical conductivity for single crystal URu ₂ Si ₂ Upper Image: Along a-axis Lower Image: Along c-axis [17]	13
2.1	Vacancy and Interstitial Defect [22, p. 92]	16
2.2	Frenkel Defect [21, p. 97]	17
2.3	Schottky Defect [21, p. 97]	18
2.4	Substitutional Impurity and Interstitial Impurity [22, p. 94]	19

2.5	Burgers vector Upper Image: Edge Dislocation Lower Image: Screw Dislocation [24]	21
2.6	Edge Dislocation [22, p. 99]	21
2.7a	Screw Dislocation [22, p. 100]	22
2.7b	Screw Dislocation Line [22, p. 100]	22
2.8	The dark lines are dislocations [22, p. 102]	23
2.9	External Surface Defects [21, p. 101]	24
2.10	Low angle grain boundary and high angle grain boundary [22, p. 103]	25
2.11	Upper Image: Tilt Boundary Lower Image: Twist Boundary [25]	25
2.12	Tilt boundary of low misorientation angle [21, p. 102]	26
2.13	Grain Boundaries [25]	26
2.14	Twin Boundary [21, p. 103]	27
2.15	Regular Stacking Sequence for FCC [26]	28
2.16	Intrinsic Stacking Fault for FCC [26]	28
2.17	Extrinsic Stacking Fault for FCC [26]	28
2.18	Three steps of the Czochralski Process [27]	29
3.1	Isothermal anneal curve of highly purified copper [29, p. 218]	32
3.2	Edge Dislocation Slip [30, p. 110]	33
3.3	Positive Dislocation Climb [29, p. 103]	33
3.4	Negative Dislocation Climb [29, p. 104]	33
3.5	Screw Dislocation Cross Slip [30, p. 111]	34
3.6	Edge Dislocation Annihilation [22, p. 202]	34
3.7	Edge Dislocation Polygonization [29, p. 225]	35
3.8	Isothermal recrystallization curve for pure copper [29, p. 230]	35
3.9	Time-Temperature recrystallization curve for zirconium (iodide) [29, p. 233]	36
3.10	Fully Recrystallized Grain Size versus Percent Elongation in α -Brass [29, p. 237] .	37
3.11	Atomic diffusion during grain growth [22, p. 224]	38
3.12	Five basic geometrical changes during grain growth [29, p. 244]	39
3.13	Growing grain diameters versus annealing time for brass [22, p. 225]	40

3.14	Retardation on grain growth in aluminum by second-phase inclusions [29, p. 251] .	40
3.15	Retardation on grain growth by pores [29, p. 252]	41
3.16	Thermal Grooving [29, p. 254]	41
3.17	Specific Heat Capacities of the annealed URu_2Si_2 and the as-grown URu_2Si_2 [34] .	45
3.18	Resistivities of the annealed URu_2Si_2 and the as-grown URu_2Si_2 [34]	46
3.19	DC magnetic susceptibility of the annealed URu_2Si_2 and the as-grown URu_2Si_2 [34]	46
3.20	Elastic Neutron Scattering of the annealed URu_2Si_2 and the as-grown URu_2Si_2 [34]	47
3.21	Resistivities of the annealed URu_2Si_2 and the as-grown URu_2Si_2 from Honma et al. [35]	48
4.1a	Cryostat Outer View [37]	49
4.1b	Cryostat Inner View [37]	49
4.2a	Bolometer Stage and Sample Stage of ^3He Refrigerator [38, p. 26]	50
4.2b	Side View of ^3He Refrigerator [39, p. 34]	51
5.1	Upper Half Complex Plane	54
5.2	W Complex Plane	57
5.3	f factor as a function of $R_{MN,OP}/R_{NO,PM}$ [45]	61
5.4	Set Up of Sample	62
5.5a	$R_{MN,OP}$	63
5.5b	$R_{NO,PM}$	63
5.6	Annealed Sample3-2 (left) and unannealed Sample1-2 mounted by five-minute epoxy (right)	65
5.7a	Resistivity vs Temperature for Sample1, Sample1-1 and Sample1-2	67
5.7b	Resistivity vs Temperature $T \leq 22.5K$ for Sample1, Sample1-1 and Sample1-2 . . .	68
5.7c	Resistivity vs Temperature $T \leq 2K$ during cooling down for annealed Sample1-1 mounted using five-minute epoxy	68
5.8a	Resistivity vs Temperature for Sample2	70
5.8b	Resistivity vs Temperature $T \leq 22.5K$ for Sample2	70
5.9a	Resistivity vs Temperature for Sample3-1 and Sample3-2	71

5.9b	Resistivity vs Temperature $T \leq 22.5K$ for Sample3-1 and Sample3-2	72
5.9c	Resistivity vs Temperature $T \leq 22.5K$ for annealed Sample3-2	73
5.10	Exponent C vs RRR	74
5.11	Hidden Order Temperature vs RRR	75
5.12	Temperature Transition Width at HO vs RRR	76
6.1	A comparison of response to applied magnetic field between ideal conductor and superconductor [54, Sec. 2.3]	80
6.2	London penetration length in a superconductor [23, p. 31]	86
6.3	Equilateral-triangle array in the vortex state [23, p. 39]	87
6.4	Magnetization curves for Type-I and Type-II superconductors [56, p. 161]	88
6.5	Two Josephson-junction loop in a applied field [58, p. 479]	91
6.6	DC-SQUID [58, p. 485]	92
6.7	Basic set up for detecting signal [59, p. 4-2]	93
6.8	Temperature dependent DC magnetization under 25 Oe and 50 Oe field for unan- nealed Sample1-2	94
6.9	Temperature dependent DC magnetization under 0 Oe field for annealed Sample1-1	95
6.10	Temperature dependent DC magnetization under 25 Oe field	96
6.11	Temperature dependent DC magnetizations for unannealed Sample1-2 and annealed Sample1-1 under 25 Oe field	97
6.12	Field dependent DC magnetization up to 10^4 Oe field	97
6.13	Field dependent DC magnetization up to 600 Oe field	98

Acknowledgements

Even though lots of difficulties appeared unexpectedly during my graduate study, I obtained help from many people. First of all I want to thank my family, who give me moral support. I am really grateful to Prof. Maureen Reedyk for supervising me to work on the challenging compound URu_2Si_2 and correcting my thesis. I want to thank Prof. Fereidoon Razavi and Prof. David Crandles, who gave me lots of help during my research. I want to thank the Machine Shop, Glass Shop and Electronic Shop for making and fixing components for our research. I want to thank Mr. David Genkin, Prof. Edward Sternin and Mr. Phil Boseglav for helping me with Linux. I want to thank ITS for fixing our computer. I want to thank Prof. Kirill Samokhin for helping me to apply for a bursary. I want to thank Prof. Shyamal Bose and Prof. Reinhard Kremer for teaching me theoretical physics. I want to thank Prof. Thad Harroun and Prof. Bozidar Mitrovic for being the members of my supervisory committee. I want to thank Dr. Hanna Dabkowska at McMaster for accepting the invitation to be the external examiner. I want to thank Mr. Frank Benko for his cooperation during my TA work and ordering supplies for our research. I want to thank Mrs. Elizabeth Horvath for her cooperation during my TA work and delivering my mail. I want to thank the graduate students Artorix Oña and Peng Xiao as well as the undergraduate student Tyler Meadows for their cooperation in our research. I also want to thank all the other graduate students and postdocs in the Department of Physics for their cooperation and for fruitful discussions in the research and the physics courses. Finally I would like to gratefully acknowledge receiving samples from Prof. Graeme Luke at McMaster and Prof. Fereidoon Razavi at Brock, which were from the time he cooperated on a study reported in reference [3].

Chapter 1

Basic Review of URu₂Si₂

1.1 Space Group of URu₂Si₂

URu₂Si₂ has a body centered tetragonal structure belonging to space group No. 139 represented by International Symbols ($I, 4/m, 2/m, 2/m$) [4].

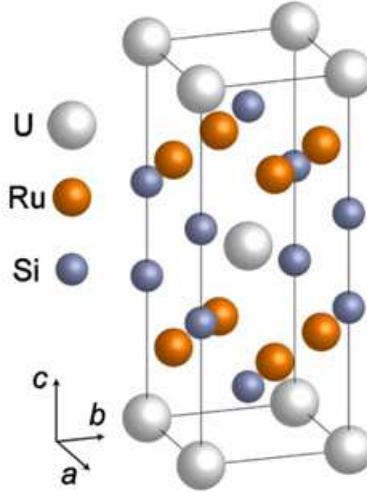


Figure 1.1: Crystal Structure of URu₂Si₂ [5]

The magnitudes of the three dimensions are related by $a = b \neq c$ and the three axes are orthogonal to each other. All possible combinations between the 32 point groups and the 14 Bravais lattices give in total 230 crystal space groups and the body centered tetragonal is labelled as No. 139. I means body centered. In $4/m$, 4 means the four-fold rotational symmetry axis, which is the c -axis, and m means a mirror symmetry plane, which is the x - y plane and perpendicular to the c -axis. In the next symbol, $2/m$, 2 means the two-fold rotational symmetry axis, the a or b axes equivalently and m means a mirror symmetry plane, the y - z plane, which is perpendicular to the a or b axis. In the last symbol, $2/m$, 2 means the two-fold rotational symmetry axis, the $\langle 110 \rangle$ axis

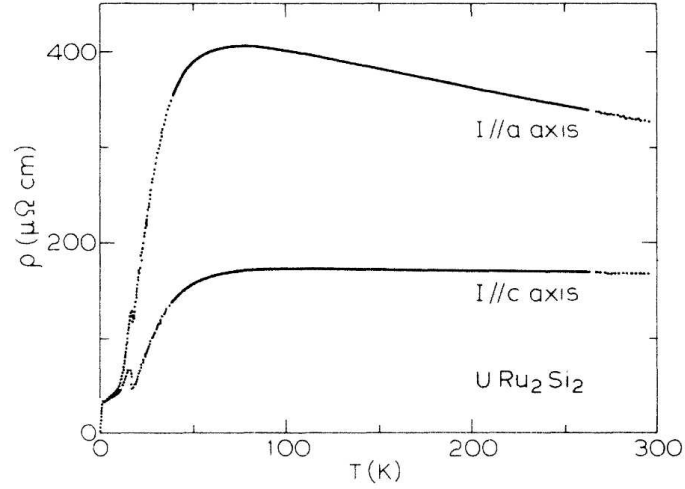
and m means a mirror symmetry plane containing the c -axis, which is perpendicular to the $\langle 110 \rangle$ axis. [6, Ch. 3, p. 4–5, p. 10]

The intersection line of any two mirror symmetry planes generates the corresponding rotation axis. The only four angles permitted between any two mirror symmetry planes are 90° , 60° , 45° and 30° . 90° generates a two-fold rotational symmetry axis. 60° generates a three-fold rotational symmetry axis. 45° generates a four-fold rotational symmetry axis. And 30° generates a six-fold rotational symmetry axis. In the body centered tetragonal structure the angle between the x - y and the y - z planes is 90° so their intersection line generates the two-fold rotational symmetry axis, the a -axis $\langle 100 \rangle$. The angle between the y - z plane and the mirror symmetry plane containing the c -axis is 45° so their intersection line generates the four-fold rotational symmetry axis, the c -axis. The angle between the x - y plane and the mirror symmetry plane containing the c -axis is 90° so their intersection line generates the two-fold rotational symmetry axis, the $\langle 110 \rangle$ axis. All of the rotational symmetry axes and mirror symmetry planes intersect at one point, the original point at which the uranium atom is. This point is the inversion center. Any two points having equal distances at opposite sides from the inversion center are duplicates but the chirality is reversed. [7]

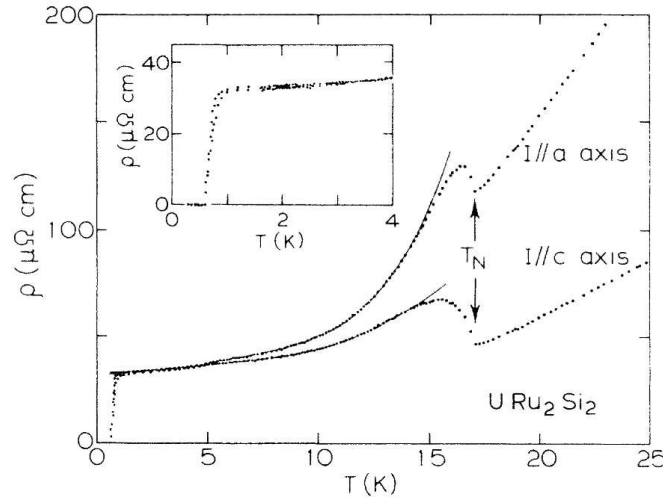
Palstra *et al.* gave the lattice constants for two as-grown single crystals, as $a = b = 4.1279(1)$ Å and $c = 9.5918(7)$ Å at 294 K, and $a = b = 4.1239(2)$ Å and $c = 9.5817(8)$ Å at 4.2 K [8]. Niklowitz *et al.* showed that in a wide temperature range below room temperature a becomes shorter as the temperature decreases while c has the same behaviour above 40 K but below 40 K becomes longer as the temperature decreases. At the Hidden Order transition the lattice constant has drastic change for both a and c axes. The magnitude of the change becomes more notable as the pressure increases from below the critical pressure, P_c , to above the critical pressure, where $P_c \approx 4.5$ kbar. [9] Using a magnetic torque technique Okazaki *et al.* showed that below the Hidden Order temperature, T_{HO} , the four-fold rotational symmetry is broken in the ab plane and thus the magnetic susceptibility becomes anisotropic in the ab plane below T_{HO} . [5]

1.2 Resistivity of URu₂Si₂

Palstra *et al.* measured the anisotropic resistivity of URu₂Si₂ [10]. It is shown in Fig. 1.2.

Figure 1.2: Resistivity vs Temperature for single crystal URu₂Si₂ [10]

The resistivities along the a axis and the c axis are highly anisotropic from 300 K down to the coherence temperature 75 K. It looks independent of temperature along the c axis while it increases along the a axis in this temperature range. Below 75 K both decrease drastically down to the superconducting transition temperature at 0.8 K. A small λ shaped cusp appears at 17.5 K, the Hidden Order temperature T_{HO} . The low temperature resistivity is shown in Fig. 1.3.

Figure 1.3: Low Temperature Resistivity for single crystal URu₂Si₂ [10]

The resistivity between 1 K and 17 K was fitted to the following equation,

$$\rho - \rho_0 = bT(1 + 2T/\Delta) \exp(-\Delta/T) + cT^2 \quad [10], \quad (1.1)$$

where ρ_0 is the residual resistivity. The term having the energy gap Δ is due to gapped spin waves in antiferromagnetism. The quadratic term is the fit for Fermi Liquid behaviour. [10] However Matsuda *et al.* showed that this equation was not adequate for the experimental data at low temperature and their fittings showed some non-Fermi liquid behaviour, which will be discussed in Sec. 5.3. [2]

1.3 Susceptibility of URu₂Si₂

1.3.1 DC Susceptibility

Palstra *et al.* measured the DC susceptibility of single crystal URu₂Si₂ under a 2 T magnetic field. Measurements were done for the field along both the a-axis and the c-axis. [8] The plots are shown in Fig. 1.4 [8].

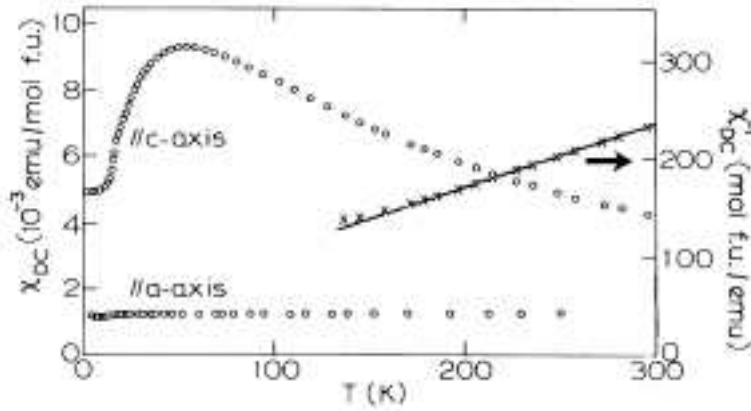


Figure 1.4: DC Susceptibility and $\frac{1}{\chi_{DC}}$ for single crystal URu₂Si₂ [8]

The c-axis is the easy axis since the susceptibility along the c-axis is higher than that along the a-axis. The maximum of $\frac{d\chi}{dT}$ is at $T_{HO} = 17.5K$. Above about 150K $\frac{1}{\chi_{DC}}$ along the c-axis can be fitted to the Curie-Weiss law but it deviates from this law at lower temperature.

1.3.2 AC Susceptibility

Palstra *et al.* also measured temperature-dependent AC susceptibility of single crystal URu₂Si₂ under different applied field. [8] The plots are shown in the inset to Fig. 1.5 [8].

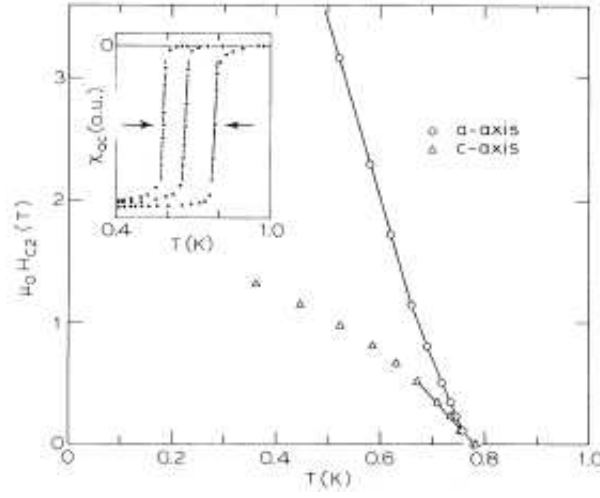


Figure 1.5: Upper critical field $\mu_0 H_{c2}$ and AC susceptibility for single crystal URu₂Si₂ [8]

The SC transition temperature is defined as the middle point of the transition width. The applied field gives the upper critical field $\mu_0 H_{c2}$ which is shown in the main figure. As the temperature decreases, the slope $-\frac{d\mu_0 H_{c2}}{dT}$ is initially the same for both directions but then decreases along the c-axis while it increases rapidly along the a-axis when the temperature is well below 0.8 K, the zero-field T_c . The inset of Fig. 1.5 [8] shows AC susceptibility along c axis under zero field, 0.52 T and 0.81 T from right to left respectively. They also measured the hysteresis magnetization loop of URu₂Si₂ in an arbitrary direction. The plot is shown in Fig. 1.6 [8].

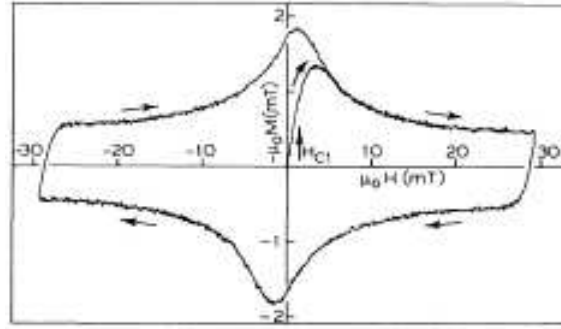


Figure 1.6: Hysteresis magnetization loop for single crystal URu₂Si₂ [8]

The field-dependent magnetization loop was measured at 0.657 K and the maximum applied field was close to 0.03 T, which is well below the upper critical field $\mu_0 H_{c2} = 0.86$ T for the same arbitrary direction at this temperature. The lower critical field determined from the virgin curve is $\mu_0 H_{c1} = 1.4$ mT. The relations among $\mu_0 H_{c1}$, $\mu_0 H_{c2}$ and Ginzburg-Landau parameter κ are discussed in Section 6.2.

1.3.3 Elastic Neutron Scattering

Butch *et al.* performed elastic neutron scattering on a single crystal of URu₂Si₂. The energy of incident neutrons was 14.7 *mV* and the corresponding wavelength λ was 2.36 Å. The plane of reflection was (100), which forbids the nuclear reflection. The plots are shown in Fig. 1.7 [11].

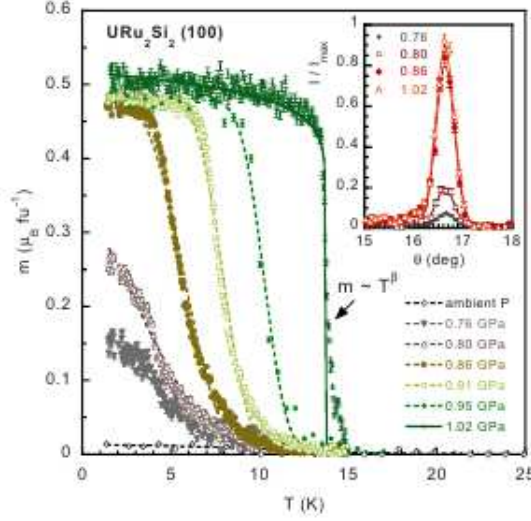


Figure 1.7: Temperature-dependent AFM moment of URu₂Si₂ under hydrostatic pressure [11]

Under ambient pressure a small magnetic moment of 0.011 $\mu_B/f.u.$ was detected below the Hidden Order temperature ($/f.u.$ means per Uranium atom, which has three $5f$ electrons). As the pressure increases, the magnitude of magnetic moment increases drastically below T_{HO} . The small ambient pressure magnetic moment becomes smaller as the sample quality has been improved compared with the earlier measurements [1, 9, 11, 12]. Thus the small magnetic moment may be due to crystal defects, which is not an intrinsic property of URu₂Si₂. With the resistivity measurements under hydrostatic pressure Butch *et al.* gave the following Pressure-Temperature phase diagram Fig. 1.8 [11]

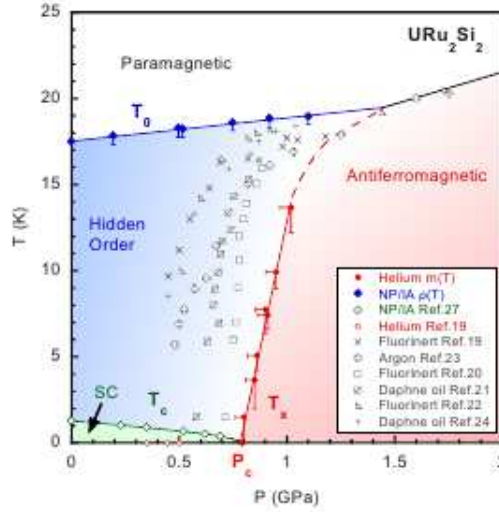


Figure 1.8: Pressure-Temperature phase diagram of URu₂Si₂ [11]

From Fig. 1.8 [11] below the critic pressure $P_c = 0.80(1)$ GPa the T_{HO} increases and the T_c of the SC transition decreases as the pressure increases. The transition temperature between the paramagnetic phase and the Hidden Order phase is $T_0 \equiv T_{HO}$. Above P_c there is a first order phase transition from the Hidden Order phase to the antiferromagnetic phase with decreasing temperature. The corresponding transition temperature at which the paramagnetic phase transfers to the antiferromagnetic phase is the Néel temperature T_N . Another feature shown is that the SC phase and the antiferromagnetic phase are excluded from each other. These results generally agree with previous publications. However variations in the phase boundary between Hidden Order and antiferromagnetism are likely due to the differing stabilities of the different methods for applying hydrostatic pressure. [11]

1.3.4 Inelastic Neutron Scattering

Bourdarot *et al.* performed inelastic neutron scattering on single crystal URu₂Si₂ in the normal state. One of the reflection planes is at (100) perpendicular to the scattering plane, which contains the wave vector $Q_0 = \langle 1, 0, 0 \rangle$. For the polarization of neutron spin along the b-axis no magnetic response was detected in the range of energy transfer explored below the Hidden Order temperature. For the polarization along the c-axis sharp resonances are found as shown in Fig. 1.9a [13] for the sample temperature above T_{HO} and in Fig. 1.9b [13] for the sample temperature below the T_{HO}

respectively.

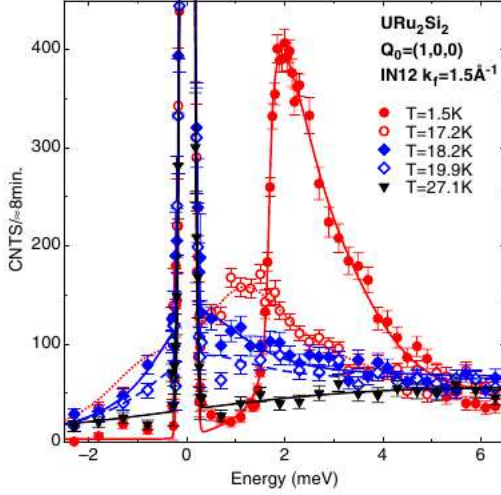


Figure 1.9a: Inelastic scattering above T_{HO} [13]

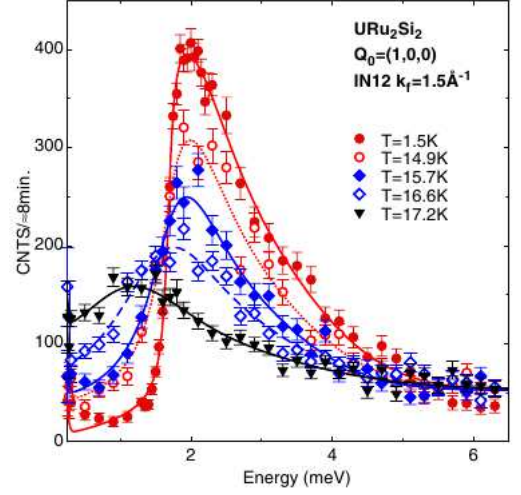


Figure 1.9b: Inelastic scattering below T_{HO} [13]

The energy axes in the two figures give the energy difference between the incident neutrons and the scattered neutrons. Above $T_{HO} = 17.5 \text{ K}$ no sharp resonance peak was detected. Below T_{HO} the sharp resonance peak shifts to higher energy and the Full Width at Half Maximum (FWHM) decreases as the temperature goes down. Below about 14 K the sharp resonance peak is fixed at about $1.7 \text{ meV} \approx 19.7 \text{ K}$ and the FWHM also approaches a constant. Besides the sharp resonance peak a broad magnetic continuum is also detected from 1.5 K to 27.1 K . In Fig. 1.9a [13] the Bragg peak at zero energy transfer corresponds to the small magnetic moment detected in the elastic neutron scattering. Bourdarot *et al.* suggest that the $5f$ electrons at Uranium sites have both localized and itinerant characteristics. [13]

Bourdarot *et al.* performed inelastic neutron scattering on an annealed single crystal of URu_2Si_2 in its superconducting state. The SC transition temperature T_c was verified to be $1.36 \pm 0.3 \text{ K}$ by AC susceptibility measurement. The reflection plane was (100). The shifts of the resonance frequencies from normal state to superconducting state are shown in Fig. 1.10 [14].

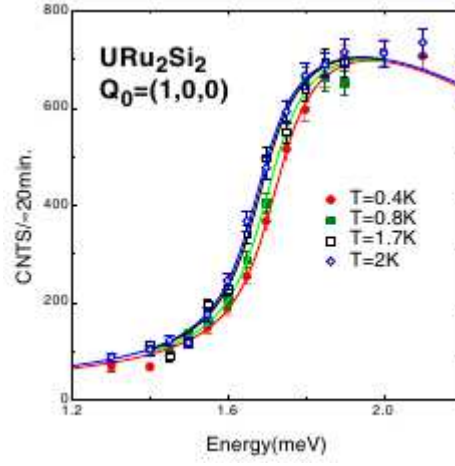


Figure 1.10: Shifts of resonance frequencies from normal state to superconducting state in single crystal URu₂Si₂ [14]

The resonance frequencies at 1.7 K and 2 K are at about 1.7 meV. Below T_c the resonance frequency shifts towards higher energy as the temperature decreases. From their fitting the resonance frequency shifts $47 \mu\text{eV} \approx 0.546 \text{ K}$ from the normal state to the temperature of absolute zero. [14]

1.4 Specific Heat Capacity of URu₂Si₂

Palstra *et al.* also measured specific heat capacity of polycrystal URu₂Si₂. The plots are shown in Fig. 1.11 [8].

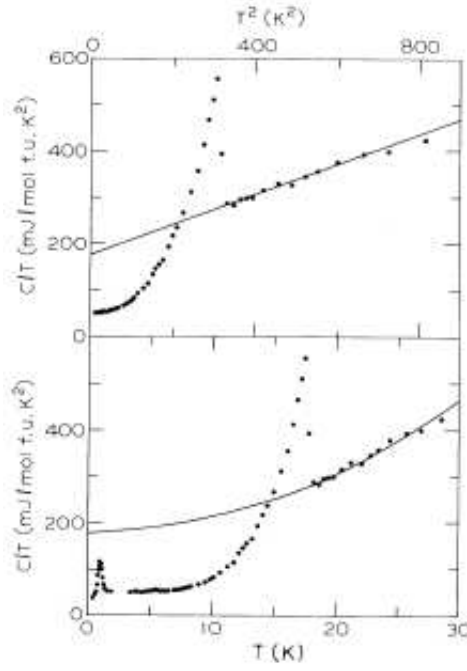


Figure 1.11: Specific heat capacity for polycrystal URu_2Si_2 [8]

Though the specific heat capacity was measured on polycrystal, at low temperature the strain energy released by crystal defects should be negligible. Around $T_{HO} = 17.5\text{ K}$ it shows a λ shaped cusp. At $T_c = 0.8\text{ K}$ another small λ shaped cusp indicates the superconducting transition. The discontinuity of the specific heat capacity measurement indicates a second order phase transition. Between 2 K and 17 K the specific heat measurement is fitted by,

$$C = \gamma T + \alpha T^3 + \delta \exp(-\Delta/T) \quad [8]. \quad (1.2)$$

The derived Sommerfeld coefficient γ is equal to $180\text{ mJ}/(K^2 \cdot \text{mol})$, which is contributed by itinerant electrons. The cubic term is the phonon contribution. The derived energy gap Δ is equal to 115 K . The derived entropy balance is about $0.2R \ln 2$ (R , Universal Gas Constant). [8] The small antiferromagnetic moment $0.02\text{-}0.04\ \mu_B/\text{U}$ detected by the elastic neutron scattering cannot explain this relatively large entropy balance if Hidden Order is due to a magnetic phase transition. This unusual relation is compared with those of other heavy fermions in Fig. 1.12 [15].

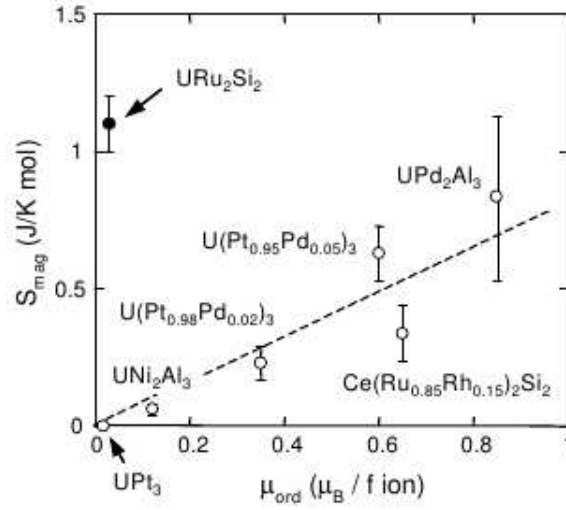


Figure 1.12: Magnetic Entropy S_{mag} vs Antiferromagnetic Moment μ_{ord} for some heavy fermions [15]

Obviously the disproportionate relation between S_{mag} and μ_{ord} for URu_2Si_2 deviates from those for other heavy fermions. [15]

1.5 Optical Measurements of URu_2Si_2

The earliest representative optical measurements were done by Bonn *et al.*. The polarization of the electric field was along the *a*-axis. The real parts of the optical conductivity for the temperature above T_{HO} and below T_{HO} are shown in Fig. 1.13a [16] and Fig. 1.13b [16] respectively.

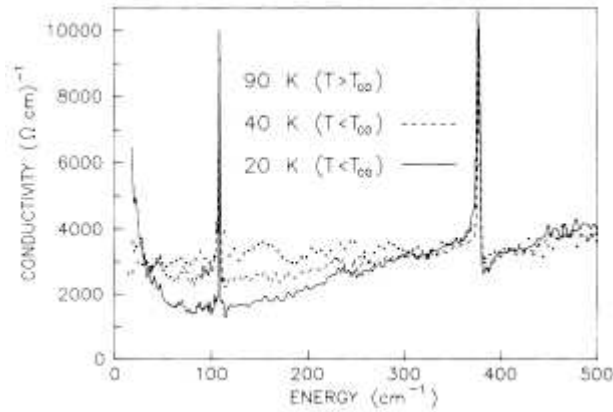


Figure 1.13a: Real part of optical conductivity above T_{HO} for single crystal URu_2Si_2 [16]

The coherence temperature T_{co} is at about 70 K. Two sharp peaks due to lattice vibrations appeared

at $108 \text{ cm}^{-1} \approx 156 \text{ K}$ and $377 \text{ cm}^{-1} \approx 543 \text{ K}$ respectively. At 90 K the optical conductivity increases with increasing photon frequency. At low frequencies the optical conductivities at 20 K and 40 K show upturns. It is much sharper at 20 K . The upturns correspond to a Drude peak resulting from the drastic decrease of the DC resistivity below T_{co} .

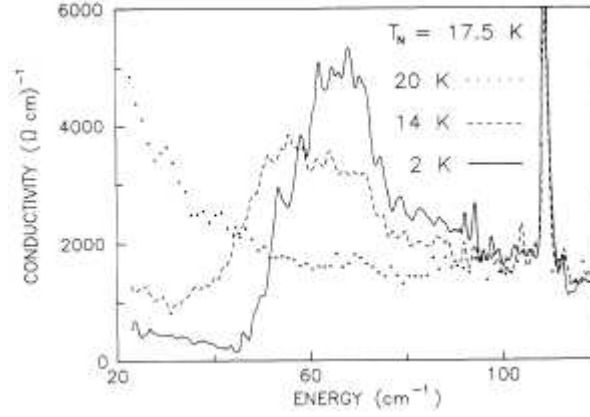


Figure 1.13b: Real part of optical conductivity below T_{HO} for single crystal URu_2Si_2 [16]

Below T_{HO} the optical conductivities show a gap like structure, which may be due to a partial removal of the Fermi surface by the Hidden Order. At 2 K the peak is at about 65 cm^{-1} and it shifts down to about 46 cm^{-1} at 14 K . Converted to absolute temperature 65 cm^{-1} and 46 cm^{-1} correspond to 94 K and 66 K respectively. [16]

More recent optical measurements were carried out by Levallois *et al.*. The polarization of the electric field was along either the a-axis or the c-axis. The real parts of optical conductivity at four different temperature are shown in Fig. 1.14 [17]. The upper image is for the a-axis and the lower image is for the c-axis respectively.

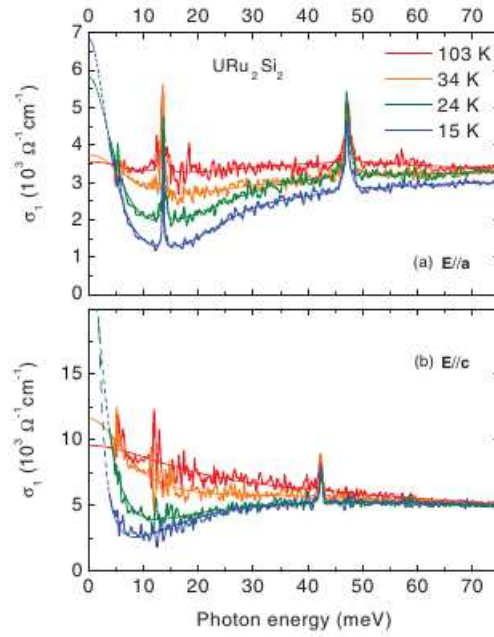


Figure 1.14: Real part of optical conductivity for single crystal URu₂Si₂
 Upper Image: Along a-axis
 Lower Image: Along c-axis [17]

As expected from DC resistivity measurements, since the c-axis is the easy axis, the optical conductivities along the c-axis are higher than those along the a-axis for a given temperature. Two sharp peaks due to lattice vibration appear at $109 \text{ cm}^{-1} \approx 157 \text{ K}$ and $380 \text{ cm}^{-1} \approx 548 \text{ K}$ along the a-axis while one sharp peak due to lattice vibration appears at $342 \text{ cm}^{-1} \approx 493 \text{ K}$ along the c-axis. Below T_{co} as the temperature decreases, a notable dip develops along both the a-axis at $120 \text{ cm}^{-1} \approx 173 \text{ K}$ and the c-axis at $90 \text{ cm}^{-1} \approx 130 \text{ K}$ corresponding to a reduction in the spectral weight in this region of the spectrum. The FWHM of the Drude peak becomes narrower as the temperature decreases. Its width is the scattering rate Γ at zero frequency and the loss of spectral weight results from the decrease in Γ . The spectral weight can be calculated from the following relations,

$$\frac{\omega_p^2}{8} = \int_0^\infty \sigma_1(\omega) d\omega = \frac{\pi N e^2}{2m^*}, \quad (1.3)$$

where ω_p is the plasma frequency, $\sigma_1(\omega)$ is the real part of optical conductivity, the integral is the spectral weight, N is the density of charge carriers, e is the electron charge and m^* is the effective mass of the electron [18, p. 66]. From T_{co} to T_{HO} the electron effective masses increase forming a heavy fermion liquid, which is due to the hybridization between the itinerant electrons

and the localized electrons. The N increases from T_{co} to T_{HO} from the Hall coefficient measurement performed by Dawson *et al.* [3]. The loss of spectral weight in this temperature range corresponds to the changes of the m^* and the N . Below T_{HO} the sudden reduction of effective mass is shown by the specific heat capacity measured by Maple *et al.*. Their fittings gave the values of Sommerfeld coefficient γ $112 \text{ mJ}/(K^2 \cdot \text{mol})$ above T_{HO} and $65.5 \text{ mJ}/(K^2 \cdot \text{mol})$ below T_{HO} respectively. The ratio of the two shows about 40% reduction in effective mass since the Sommerfeld coefficient is proportional to effective mass. [19] But the loss of spectral weight continues below T_{HO} , from Eq. 1.3 the N has to decrease substantially. The loss of N corresponds to the Hall coefficient measurement. It showed that the Hall coefficient jumped by a factor more than four around T_{HO} . [3]

Chapter 2

Defects in Crystals

Crystals are like people, it is the defects in them which tend to make them interesting!

— Colin Humphreys [20]

Perfect crystals do not exist in nature. Real crystals always have some kinds of defects. These defects affect their physical properties, e.g. stiffness, colour, electrical conductivity, magnetic hysteresis, dielectric strength, etc.. Sometimes the defects are desired. For example, in electronics the silicon used requires a small concentration of chemical impurities such as phosphorus and arsenic [21, p. 95-96] [22, p. 91]. Steel needs to be carbonised properly for different strengths. As another example, a Type-II superconductor needs some lattice distortions so that vortices can be pinned by these defects and the transport current can flow around the vortices without resistance [23, p. 42].

The defects are sorted by dimension as follows,

- (i) Point defects
- (ii) Line defects
- (iii) Surface defects
- (iv) Volume defects

[21, p. 96]

2.1 Point Defects

Point defects occur at lattice points and are due to imperfect packing of atoms during crystallization or to vibrations of atoms at high temperatures [21, p. 96]. The number of defects at equilibrium

concentration at a certain temperature is given by Eq. 2.1,

$$n_{PD} = N \exp \left(-\frac{E}{kT} \right), \quad (2.1)$$

where n_{PD} is the number of point defects, N is the number of lattice points, E is the free energy needed to form a point defect, k is the Boltzmann constant and T is the absolute temperature [21, p. 96] [22, p. 92]. The typical value of $\frac{n_{PD}}{N}$ is 10^{-5} . $\frac{n_{PD}}{N}$ can be reduced by slowly cooling the sample. [21, p. 96]

The kinds of point defects are as follows,

- (i) Vacancies
- (ii) Interstitial Defects
- (iii) Frenkel Defect
- (iv) Schottky Defect
- (v) Impurity
- (vi) Phonon

2.1.1 Vacancies

A lattice point is normally occupied by an atom. But in the case it is missing, a vacancy defect forms as shown in Fig. 2.1 [22, p. 92].

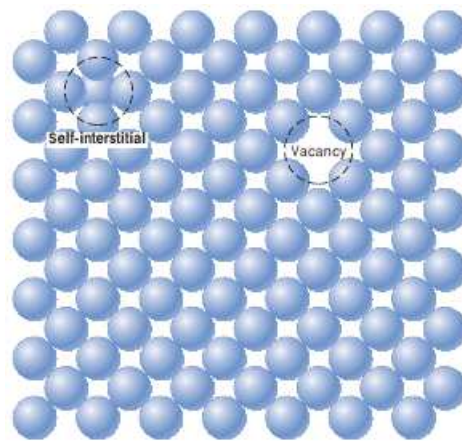


Figure 2.1: Vacancy and Interstitial Defect [22, p. 92]

The vacancies increase the entropy of the crystal. At a temperature of $20^{\circ}\text{C} - 25^{\circ}\text{C}$ copper has

10^{-13} vacancies [21, p. 97]. Just below the melting point most metals have 10^{-4} vacancies calculated by Eq. 2.1 [22, p. 93]. As the temperature increases, the probability for individual atoms escaping from their equilibrium positions increases and so do the number of vacancies as indicated by Eq. 2.1. The vacancies can be formed in a di-vacancy or a tri-vacancy [21, p. 97].

2.1.2 Interstitial Defects

Interstitial defects happen when the volume fraction of the crystal structure is low so there are some voids among regular lattice points. Then some extra atoms can insert into these interstitial spaces, which can cause large structural distortions if the size of these atoms is comparable to that of the surrounding atoms. An example of an interstitial defect is also shown in Fig. 2.1. The interstitial defects can also be formed in di-interstitial or tri-interstitial configurations. The probability for forming an interstitial defect is lower than that for a vacancy since it needs higher free energy. [21, p. 97] [22, p. 93]

2.1.3 Frenkel Defect

A Frenkel defect occurs when an atom immigrates from its normal position to an interstitial site and hence the original point becomes a vacancy. This is illustrated in Fig. 2.2 [21, p. 97].

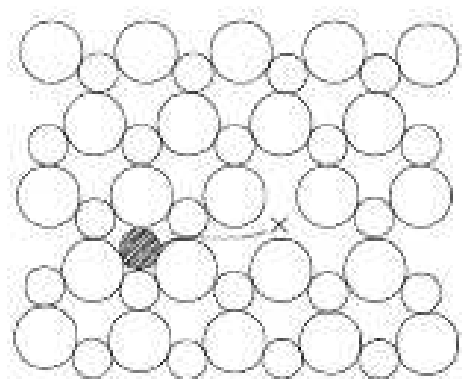


Figure 2.2: Frenkel Defect [21, p. 97]

Frenkel defects happen more commonly in ionic crystals because the smaller cations can easily fit into the interstitial spaces.

2.1.4 Schottky Defect

Schottky defects occur when a pair consisting of a cation and an anion is missing from their normal positions so that the crystal is still charge neutral [21, p. 98]. An example is shown in Fig. 2.3 [21, p. 97].

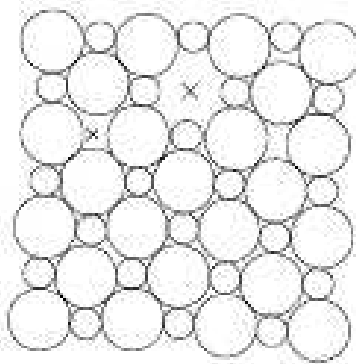


Figure 2.3: Schottky Defect [21, p. 97]

Frenkel defects need higher energy to form than Schottky defects.

2.1.5 Impurity

Real crystals always contain impurities. It is very difficult to purify metals in excess of 99.9999%. With this percentage 10^{22} to 10^{23} foreign atoms dissolve in one cubic meter of host material [22, p. 93]. There are two kinds of impurity defects, substitutional and interstitial. For substitutional impurities the foreign atoms substitute the host atoms. For interstitial impurities the foreign atoms occupy the interstitial spaces. These are shown in Fig. 2.4 [22, p. 94].

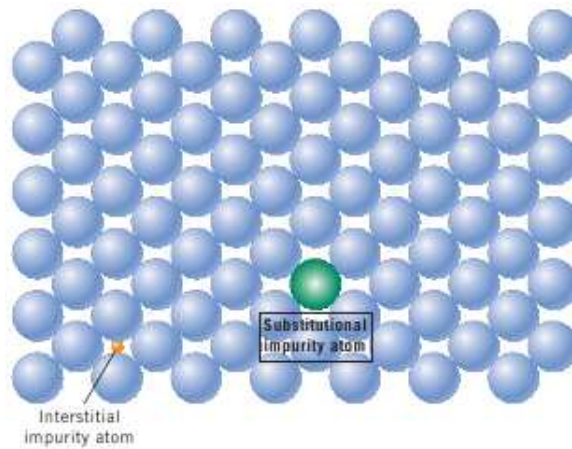


Figure 2.4: Substitutional Impurity and Interstitial Impurity [22, p. 94]

The Hume-Rothery rules state that four factors affect the degree to which the foreign atoms dissolve into the host material as follows,

(i) Atomic size factor

The foreign atoms can dissolve into the host material without substantial structural distortion if the difference of atomic radii between the foreign atoms and the host atoms is less than about $\pm 15\%$.

(ii) Crystal structure

If the foreign atoms and the host atoms have similar crystal structure, it will be easy for the foreign atoms to dissolve into the host material.

(iii) Electronegativity

The more electropositive elements and the more electronegative elements are likely to form an intermetallic compound other than a substitutional impurity.

(iv) Valences

A metal is more likely to dissolve into another metal with higher valency than a metal with lower valency. [22, p. 95]

2.1.6 Phonon

The importance of lattice vibrations will increase as the temperature increases. The lattice vibration will deform the structure symmetry [21, p. 98].

2.1.7 Methods to create point defects

There are several processes by way of which point defects are created. They include,

- (i) Thermal vibrations
- (ii) Quenching the samples rapidly from high to low temperature.
- (iii) Mechanically deforming the crystal lattice.
- (iv) Bombarding the host material by foreign atoms. [21, p. 98]

2.2 Line defects

Line defects are also called dislocations. Line defects are a one dimensional defect around which some of the atoms are misaligned. There are two basic types of dislocations: the edge dislocation and the screw dislocation.

2.2.1 Burgers Vector

The Burgers vector is used to describe the magnitude and direction of the dislocation. There are two steps to find the Burgers vector in a distorted crystal structure. Firstly one needs to draw an arbitrary contour in an ideal lattice, which has a length of multiple lattice constants. Secondly one tries to use a contour of the same length to enclose the dislocation in the distorted lattice. It turns out that an extra vector will be needed to enclose the dislocation completely. Or vice versa if a contour enclosing the dislocation completely in the distorted lattice is to be fitted into an ideal lattice, an extra vector appears. This vector is the Burgers vector denoted by \mathbf{b} . Burgers vectors for edge and screw dislocations are shown in Fig. 2.5 [24].

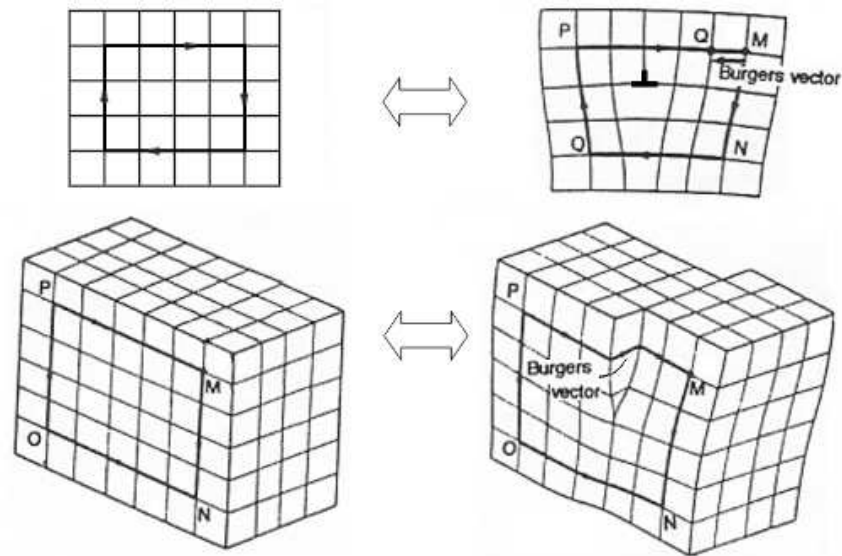


Figure 2.5: Burgers vector
 Upper Image: Edge Dislocation
 Lower Image: Screw Dislocation [24]

2.2.2 Edge Dislocation

An edge dislocation occurs when an extra atomic plane inserts into the regular lattice as shown in Fig. 2.6 [22, p. 99].

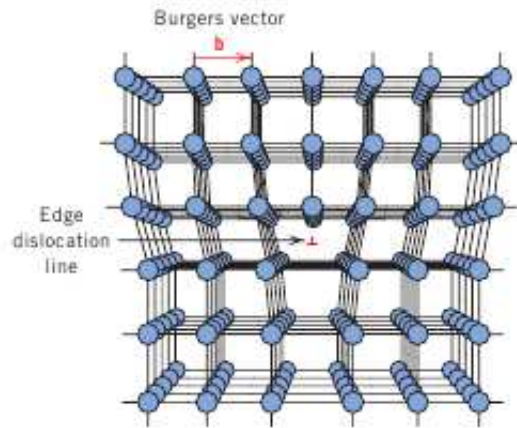


Figure 2.6: Edge Dislocation [22, p. 99]

The edge dislocation centers on a line which is along the end of the extra atomic plane. This line is called a dislocation line. The dislocation line is perpendicular to Burgers vector. The atoms above the dislocation line are squeezed together and those below the dislocation line are spread apart. As the distance becomes further away from the dislocation line, the distortion is less severe. The

dislocation is denoted by \perp if the extra atomic plane is above the dislocation line. It is denoted by \top if the plane is below the dislocation line. [22, p. 99] [21, p. 98]

2.2.3 Screw Dislocation

A screw dislocation can be thought to be formed by a shear stress as shown in Fig. 2.7a [22, p. 100].

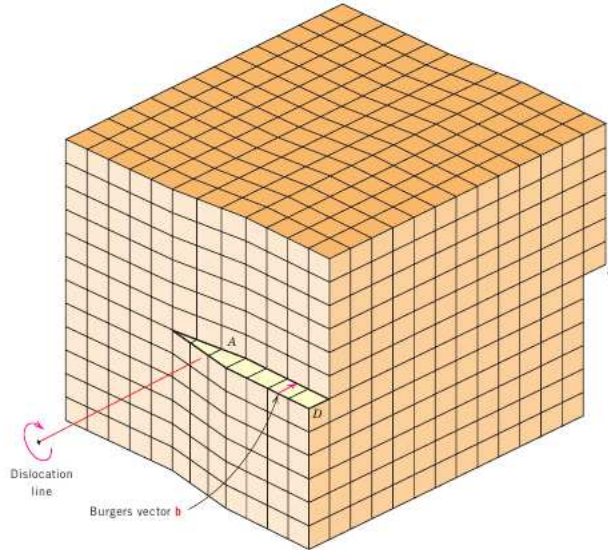


Figure 2.7a: Screw Dislocation [22, p. 100]

The upper atomic plane shifts relatively to the lower plane. In Fig. 2.7b [22, p. 100] line AB is the screw dislocation line. The screw dislocation line is parallel to the Burgers vector.

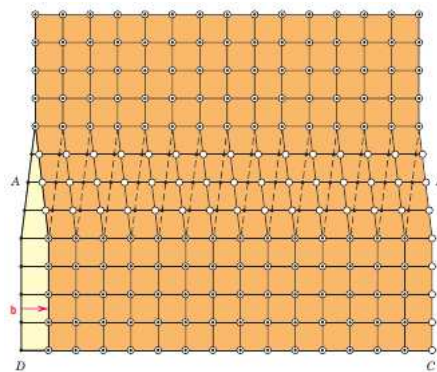


Figure 2.7b: Screw Dislocation Line [22, p. 100]

The open circles denote the upper plane and the solid circles denote the lower.

Dislocations have the following three geometrical characteristics,

- (i) Natural dislocations are usually mixed dislocations, which are combinations of edge and screw

dislocations. In this case Burgers vectors are neither perpendicular nor parallel to the dislocation lines but the Burgers vector will be the same at any point of the same dislocation. [22, p. 100]

(ii) The vectorial sum of the Burgers vectors at a meeting point of different dislocations must be zero. This point is called a node. [21, p. 101]

(iii) A dislocation line must end at a node or the sample surface. It cannot end inside the sample. Alternatively the dislocation line can end itself in a loop. [21, p. 101]

The total length of all dislocation lines divided by the sample volume gives the dislocation density. For semiconductor crystals it may have a value of $10^4 - 10^5 \text{ cm}^{-2}$. For annealed metals it may have a value of $10^6 - 10^8 \text{ cm}^{-2}$. As an approximation for elastic strain the distortional energy E per unit length associated with the dislocations can be calculated by,

$$E = \frac{\mu \mathbf{b}^2}{2}, \quad (2.2)$$

where μ is the shear modulus and \mathbf{b} is the Burgers vector. [21, p. 101]

Impurity atoms tend to concentrate inside the dislocations. The dislocation lines of a titanium alloy are shown in a transmission electron micrograph in Fig. 2.8 [22, p. 102].

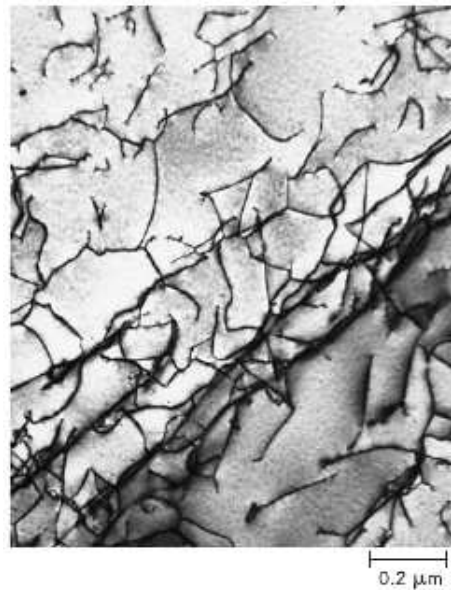


Figure 2.8: The dark lines are dislocations [22, p. 102]

2.3 Surface defects

Surface defects are two-dimensional defects. Surface defects are divided into external and internal surface defects. Internal surface defects are further subdivided into grain boundaries, twin boundaries and stacking faults.

2.3.1 External Surface Defects

External surface defects are due to the fact that surface atoms of samples are not bonded on one side so they have higher energy than that possessed by the interior atoms. A sketch of this defect is shown in Fig. 2.9 [21, p. 101].

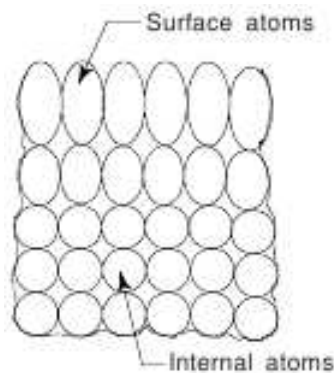


Figure 2.9: External Surface Defects [21, p. 101]

A liquid drop tends to minimize such surface energy by forming in a sphere, which reduces the total surface area. But this is impossible for a rigid crystal. [22, p.103]

2.3.2 Grain Boundaries

When two grains of different orientations are neighbouring, there is a distorted transition zone between them, which is not aligned with either of the two grains. This zone is called the grain boundary. The atoms in the grain boundaries have higher energy than that possessed by the atoms in the grains. Grain boundary defects can occur during nucleation or crystallization and their thickness may be from 1 nm to 5 nm . The grain boundary defects can be divided into low angle grain boundaries and high angle grain boundaries. For low angle grain boundaries the angle between

two neighbouring grains is less than 10° . For high angle grain boundaries it is more than or equal to 10° . [21, p. 101-102] These two cases are shown in Fig. 2.10. [22, p. 103]

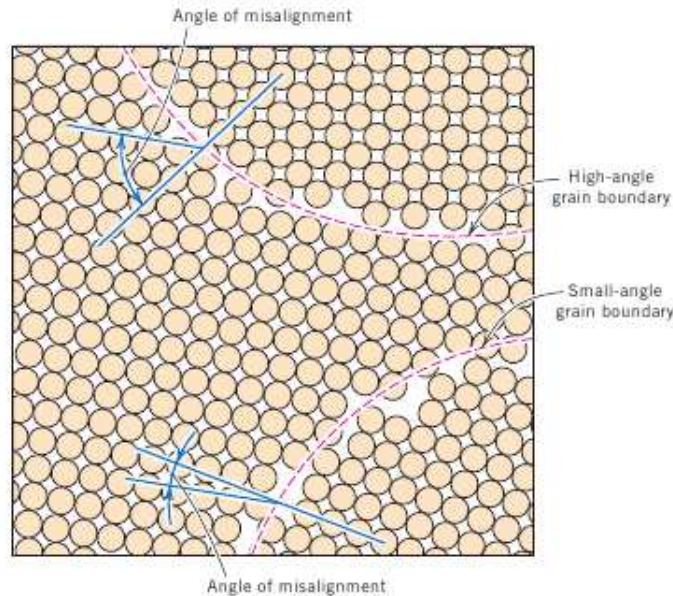


Figure 2.10: Low angle grain boundary and high angle grain boundary [22, p. 103]

Grain boundary defects can also be divided into tilt boundaries and twist boundaries. For tilt boundaries the angle of misorientation is perpendicular to the boundary, which can be thought of as an array of edge dislocations [21, p. 102]. For twist boundaries the angle of misorientation is parallel to the boundary, which can be thought of as an array of screw dislocations [22, p. 104]. These two cases are shown in Fig. 2.11 [25].

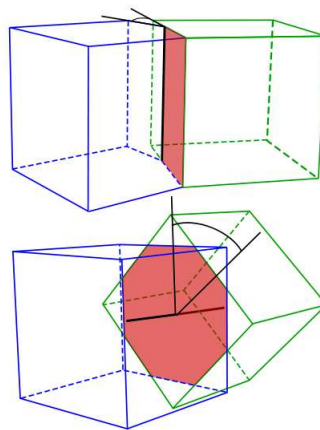


Figure 2.11: Upper Image: Tilt Boundary
Lower Image: Twist Boundary [25]

If the misorientation angle θ of the tilt boundary is small enough, since $\tan \theta \approx \theta$, θ can be calculated by,

$$\theta \approx \frac{\mathbf{b}}{D}, \quad (2.3)$$

where \mathbf{b} is the Burgers vector and D is the average vertical distance between two edge dislocations. This is illustrated in Fig. 2.12 [21, p. 102].

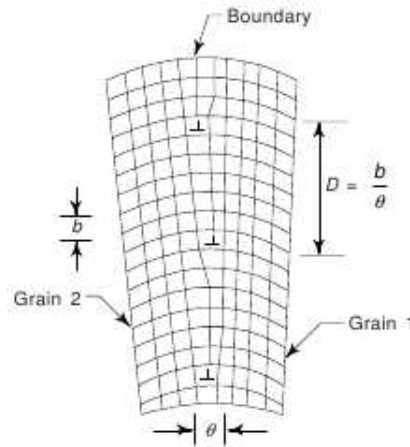


Figure 2.12: Tilt boundary of low misorientation angle [21, p. 102]

If two neighbouring grains have different crystal structures or compositions, the grain boundary is called an interphase boundary. Because the atoms in grain boundaries have higher energy, these boundaries are more chemically reactive and more likely to host impurity atoms. [21, p. 101] [22, p. 103-104] Fig. 2.13 shows grain boundaries of an acid-etched polycrystalline metal [25].

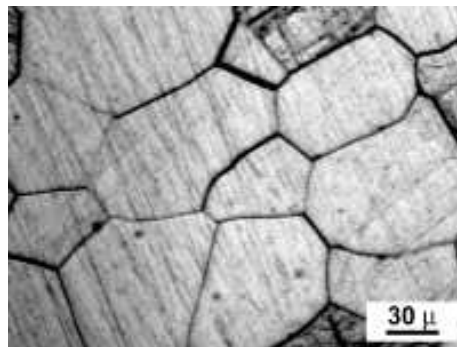


Figure 2.13: Grain Boundaries [25]

2.3.3 Twin Boundaries

Crystal structures on the two sides of the twin boundary have a mirror symmetry as shown in Fig. 2.14 [21, p. 103].

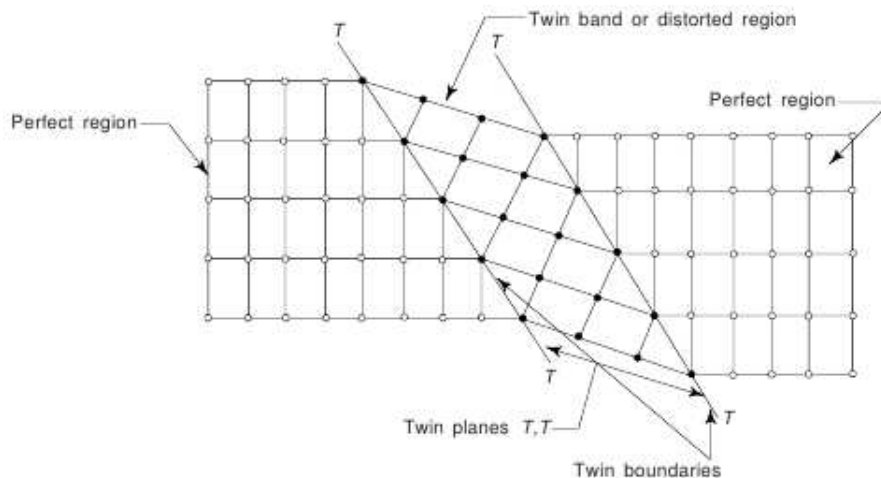


Figure 2.14: Twin Boundary [21, p. 103]

There are two types of twin boundaries according to how they form. Mechanical twins are due to atomic displacements made by mechanical shear forces. Annealing twins are due to the displacements made by annealing after plastic deformation. Mechanical twins typically appear in Body Centered Cubic (BCC) and Hexagonal Close Packed (HCP) metals. Annealing twins typically appear in Face Centered Cubic (FCC) metals. [22, p. 106] [21, p. 103]

2.3.4 Stacking Faults

Stacking faults happen when the regular stacking sequence of atomic planes is interrupted. There are two types of stacking faults, intrinsic stacking faults and extrinsic stacking faults. If an atomic plane is missing from the regular sequence, it is an intrinsic stacking fault. If an extra atomic plane appears in the regular sequence, it is an extrinsic stacking fault. We can take the FCC lattice as an example. The regular sequence of atomic planes for an FCC lattice is ABCABCABC..., as shown in Fig. 2.15. [26]

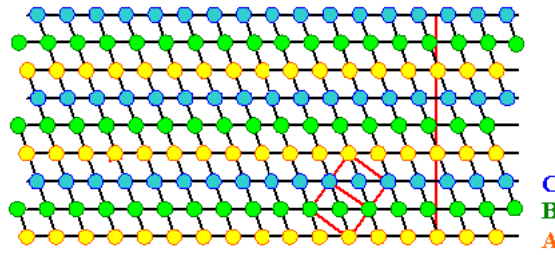


Figure 2.15: Regular Stacking Sequence for FCC [26]

The stacking sequence is along the $[111]$ direction. The cross-sectional view is along the $[110]$ direction. When an intrinsic stacking fault happens, for example, part of a C atomic plane is missing, the stacking sequence becomes $ABCABABC\cdots$ as shown in Fig. 2.16. [26]

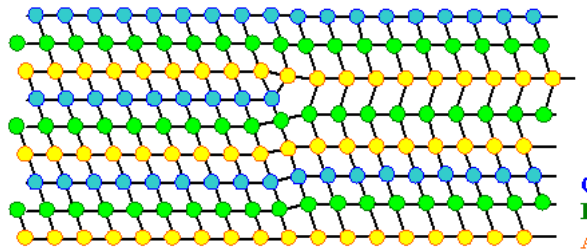


Figure 2.16: Intrinsic Stacking Fault for FCC [26]

When an extrinsic stacking fault happens, for example, part of an A atomic plane tucks between the B plane and the C plane, the stacking sequence becomes $ABCABACABC\cdots$ as shown in Fig. 2.17. [26]

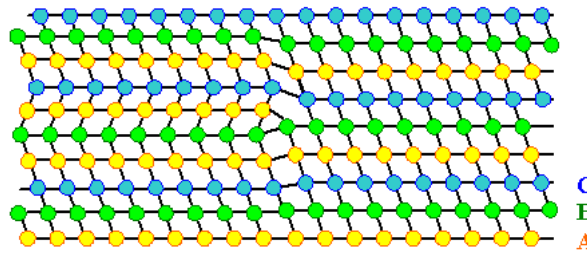


Figure 2.17: Extrinsic Stacking Fault for FCC [26]

Since $ABABAB\cdots$ is HCP structure, FCC with stacking fault is a mixture of FCC and HCP. There is a certain stacking fault energy in the defects. [26]

2.4 Volume Defects

Volume defects include cracks, large vacancies, foreign particle inclusions and non-crystalline regions with dimensions over 0.20 nm. Volume defects usually occur during processing and fabrication. [21, p. 104] [22, p. 106]

2.5 Czochralski Process

The samples used for the measurements were grown by the Czochralski Process. As an example, the three steps of growing single crystal silicon is shown in Fig. 2.18. [27]

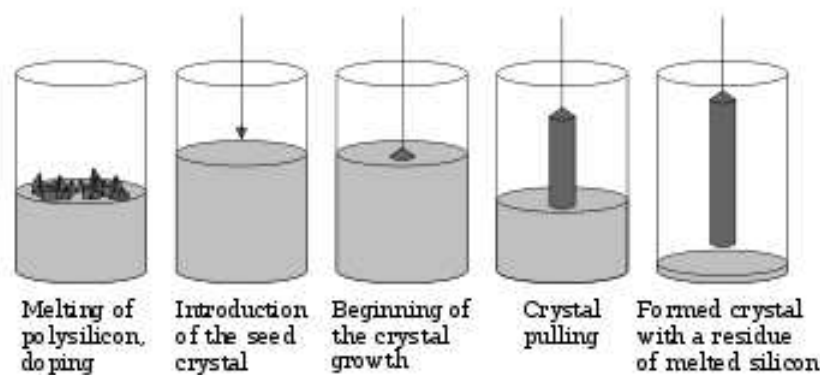


Figure 2.18: Three steps of the Czochralski Process [27]

The three steps are carried out in a vacuum or an atmosphere of inert gas.

Step 1: Melting the elements in a crucible.

Step 2: A precisely oriented small seed crystal is mounted on the end of a rotating rod. The seed is lowered just a little below the surface of molten elements.

Step 3: The rod and the crucible rotate in opposite directions. The rotating rod is slowly raised up while a cylindrical boule grows below the seed, which has the same orientation of the seed. Three parameters need to be precisely controlled, the temperature gradients, the rate of pulling and the speeds of the two opposite rotations.

The main defects generated during the Czochralski Process are due to impurities dissolved into the molten elements from the crucible. [27]

Matsuda *et al.* claimed that the quality of URu_2Si_2 mainly depends on the purity of uranium, which usually has lower purity than those of Ru and Si. They found that for Czochralski grown crystals URu_2Si_2 on the surface of the ingot has better quality than crystals derived from near the core of the ingot. [2, 28]

Chapter 3

Annealing Samples

3.1 Annealing Mechanisms

Annealing is one method of several heat treatment processes. The purposes of annealing are,

- (i) relieve stresses,
- (ii) increase softness, ductility or toughness,
- (iii) produce a specific micro structure.

Annealing has three steps, which are,

- (i) raise the sample temperature to a certain level,
- (ii) keep the sample at this temperature for a certain period of time,
- (iii) slowly cool the sample down.

During step one and step three a temperature gradient exists between the interior and the exterior of the sample so the rate at which temperature is changed should not be too fast. A fast changing rate can induce high internal stress, which may warp or even crack the sample. For step two the annealing time needs to be long enough for an effective transformation. The temperature needs to be controlled accurately because it plays a key role in the annealing process, which will be discussed in the following sections. [22, p. 422] [21, p. 322]

3.1.1 Strain Energy

The crystal distortions store a certain amount of energy. The increased Gibbs free energy is,

$$\Delta G = \Delta H - T\Delta S. \quad (3.1)$$

ΔH is the increased enthalpy, namely the stored strain energy. ΔS is the increased entropy. It is assumed that the distortions happen at a constant temperature T . [29, p. 217] The stored strain energy will be released during annealing as shown in the isothermal anneal curve, Fig. 3.1 [29, p. 218].

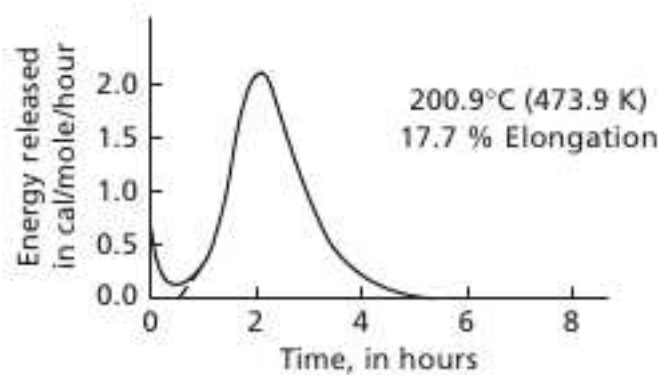


Figure 3.1: Isothermal anneal curve of highly purified copper [29, p. 218]

In this example, the temperature is kept at 473.9 K. Initially a small amount of energy is released during the time before the dashed curve. This first stage of annealing is called recovery. As the time increases, the released energy reaches a peak and then slows down. This second stage is called recrystallization. As the time increases further, a third stage occurs called grain growth. For the anisothermal annealing these three stages continue as a function of temperature. All three stages happen below the melting point. [29, p. 218-219]

3.1.2 Recovery

The recovery process usually happens below one-third of the melting temperature and involves edge dislocation slip, edge dislocation climb, screw dislocation cross slip, dislocation annihilation and polygonization.

The plane that contains both the Burgers vector and the dislocation line is defined as a slip plane. For edge dislocation the extra atomic rows can only slip in a certain slip plane. This restriction is because its Burgers vector is perpendicular to the dislocation line. The slip is shown in Fig. 3.2 [30, p. 110].

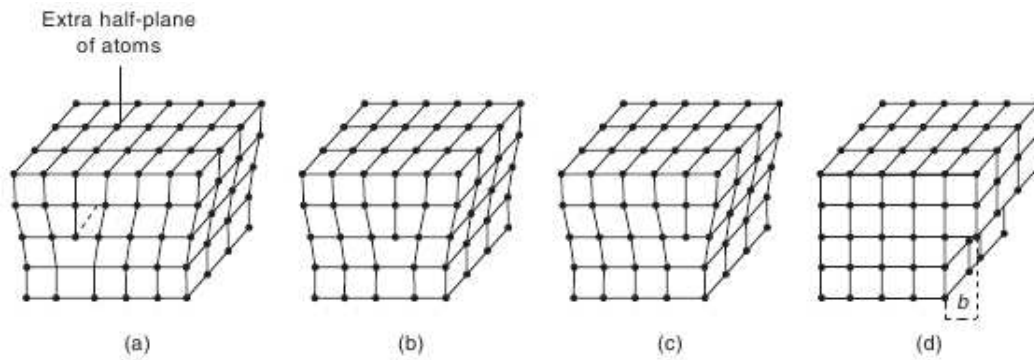


Figure 3.2: Edge Dislocation Slip [30, p. 110]

The edge dislocation slip can happen at a relatively low temperature. To move in a direction perpendicular to the slip plane the edge dislocation needs vacancy defects to assist. This movement is called dislocation climb. Positive climb is illustrated in Fig. 3.3 [29, p. 103].

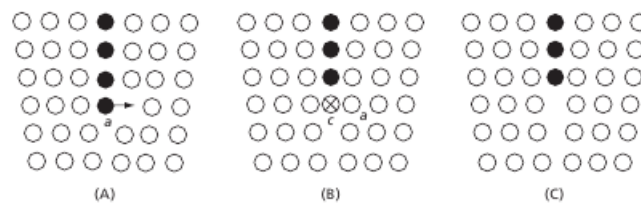


Figure 3.3: Positive Dislocation Climb [29, p. 103]

The atom *a* at the bottom of the extra plane moves into a neighbouring vacancy. Atom *c* is behind *a*. If atoms of the entire bottom row move into vacancies, the extra plane become shorter. The negative climb is shown in Fig. 3.4 [29, p. 104].

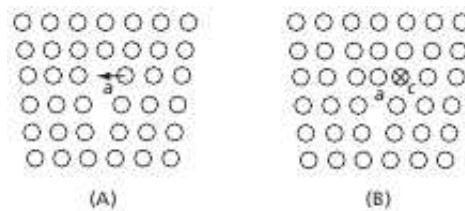


Figure 3.4: Negative Dislocation Climb [29, p. 104]

Individual atom *a* moves to a neighbouring vacancy just below the bottom of the extra plane. Atom *c* was originally behind *a*. If this individual process makes an entire row just below the original extra plane, the extra plane become longer. To complete dislocation climb it needs a certain number

of highly mobile vacancies. Such vacancies increase in number as temperature rises so it can only happen at a relatively high temperature.

For screw dislocation because its Burgers vector and the dislocation line are parallel, it can slip in any plane which passes the dislocation line. This is illustrated in Fig. 3.5 [30, p. 111].

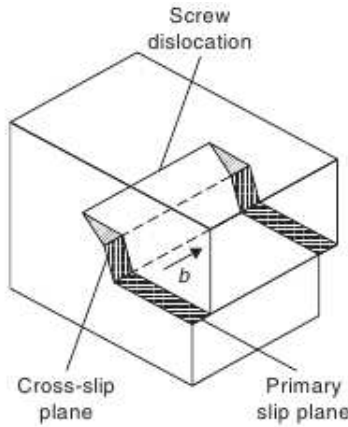


Figure 3.5: Screw Dislocation Cross Slip [30, p. 111]

The original screw dislocation moves into a slip plane through a step, which is higher than the original slip plane. This is called cross slip.

If two edge dislocations have the same sign and lie in the same slip plane, they will repel each other. If they have opposite sign, they will attract each other and annihilate eventually as shown in Fig. 3.6 [22, p. 202].

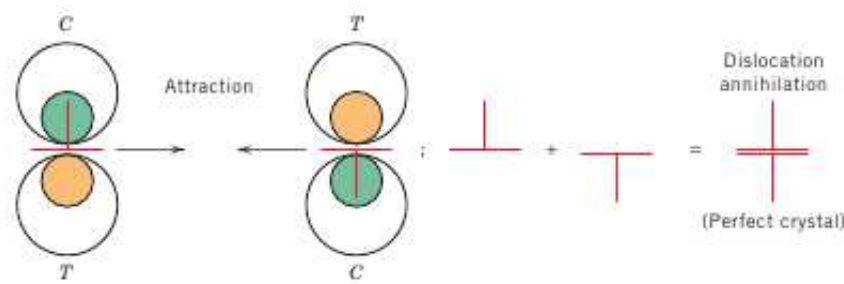


Figure 3.6: Edge Dislocation Annihilation [22, p. 202]

A right hand screw dislocation can also annihilate with a left hand screw dislocation.

A plastically bent crystal will have a certain number of positive edge dislocations towards the curvature. This is shown in Image A of Fig. 3.7 [29, p. 225]. After annealing these randomly distributed edge dislocations will align between any two subgrains, forming low angle grain boundaries.

The strain fields of aligned edge dislocations can be partially canceled. This is shown in Image B of Fig. 3.7 [29, p. 225]. This process is called polygonization.

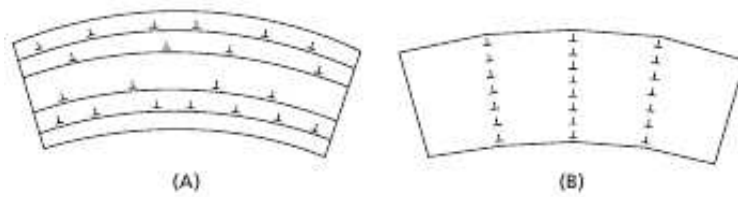


Figure 3.7: Edge Dislocation Polygonization [29, p. 225]

3.1.3 Recrystallization

If the annealing temperature is higher or the annealing time is longer at high enough temperature, recrystallization will happen after the recovery. During recrystallization some small crystals nucleate most likely at the distorted regions. The orientations of these nucleations are different from the surrounding areas. The nucleations may continue to grow and consume the surrounding subgrains if they have the advantage in sizes. The growth will continue until new strain free grains form, which will have high angle boundaries with the surrounding grains. The rate of recrystallization depends on three important factors, (i) the annealing temperature, (ii) the level of deformation during cold works and (iii) the purity of samples. [30, p. 352]

A plot of percent recrystallization versus log time at different annealing temperature is shown in Fig. 3.8 [29, p. 230].

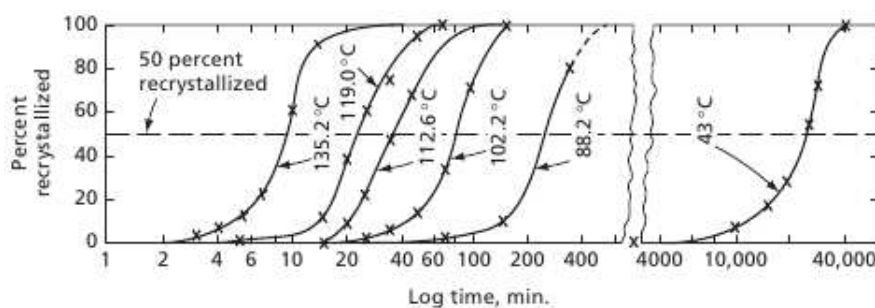


Figure 3.8: Isothermal recrystallization curve for pure copper [29, p. 230]

So for a certain percentage of recrystallization the annealing time decreases rapidly with increasing temperature. The relation between annealing time and temperature for a certain percentage of

recrystallization is given by,

$$\frac{1}{\tau} = A \exp\left(-\frac{Q_A}{RT}\right), \quad (3.2)$$

where τ is the annealing time, A is a constant, Q_A is the activation energy for the recrystallization, R is the gas constant and T is the annealing temperature. The recrystallization temperature is defined as the temperature at which full recrystallization is completed during one hour. [29, p. 231-232]

The plots of annealing time to complete recrystallization versus temperature of two zirconium crystals are shown in Fig. 3.9. The plots are for full recrystallization. One crystal had 13% deformation during the cold works (A metal is plastically deformed below its melting temperature.) and the other had 51%. [29, p. 233]

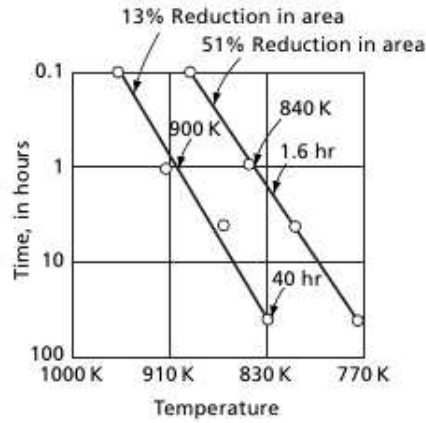


Figure 3.9: Time-Temperature recrystallization curve for zirconium (iodide) [29, p. 233]

So for the same annealing time the zirconium of higher deformation needs lower annealing temperature to fully recrystallize. And for the same annealing temperature the one of higher deformation needs much less annealing time to complete. The two plots also have different slope and from Eq. 3.2 this means the one of higher deformation needs lower activation energy to complete.

The grain sizes at the end of full crystallization depend on the deformation level during the cold works other than the annealing temperature. This is evident in Fig. 3.10 [29, p. 237].

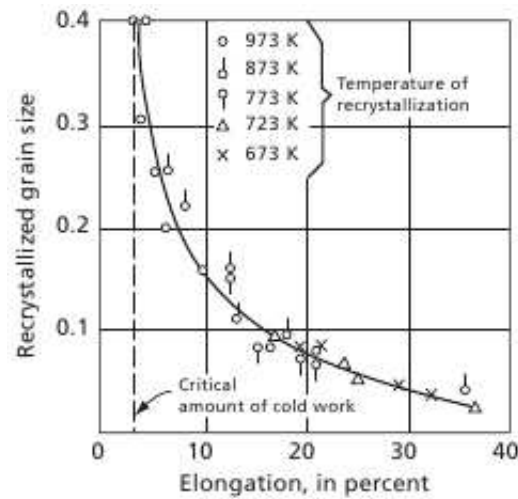


Figure 3.10: Fully Recrystallized Grain Size versus Percent Elongation in α -Brass [29, p. 237]

For five different annealing temperatures and any given percent elongation the grain sizes are almost the same. The plots also show that with higher elongated percentage the final grain sizes are smaller. Another important feature shown is that below a minimum amount of elongation the recrystallization cannot happen. This minimum value of deformation during cold works is called critical strain and it is about 3% in Fig. 3.10. The critical strain depends on what kind of deformation exists. If a certain kind of deformation is below its critical strain, the recrystallization cannot happen at any annealing temperature. [29, p. 237-239]

The recrystallization temperature can be increased by several hundred degrees even though only 0.01% foreign atoms are present in the sample. Table 3.1 [29, p. 240] shows how different kinds of foreign atoms increase the recrystallization temperature of pure copper by an impurity level of 0.01 atomic percent.

Impurity Atoms	Increase in the recrystallization temperature (K)
Ni	0
Co	15
Fe	15
Ag	80
Sn	180
Te	240

Table 3.1: Effects of atomic 0.01% impurity on the recrystallization temperature of pure copper [29, p. 240]

Foreign atoms reduce the mobility of grain boundaries, which retards the recrystallization.

3.1.4 Grain Growth

The new strain free grains can grow further after the full recrystallization. Atomic diffusion during grain growth across a grain boundary is shown in Fig. 3.11 [22, p. 224].

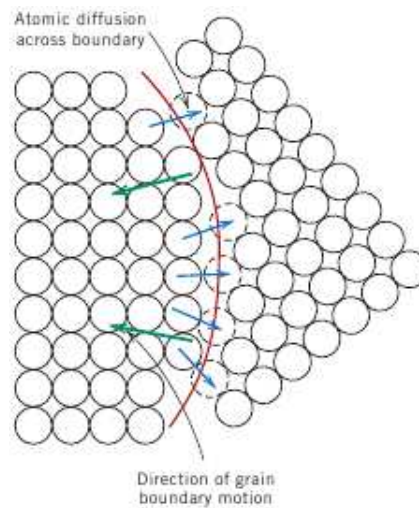


Figure 3.11: Atomic diffusion during grain growth [22, p. 224]

Atoms diffuse from the convex side to the concave side and in the opposite direction simultaneously. Fig. 3.11 shows the net diffusion is from the concave side to the convex side and the grain boundary migrates towards the concave side. The 3-D geometrical changes during grain growth are shown in Fig. 3.12 [29, p. 244].

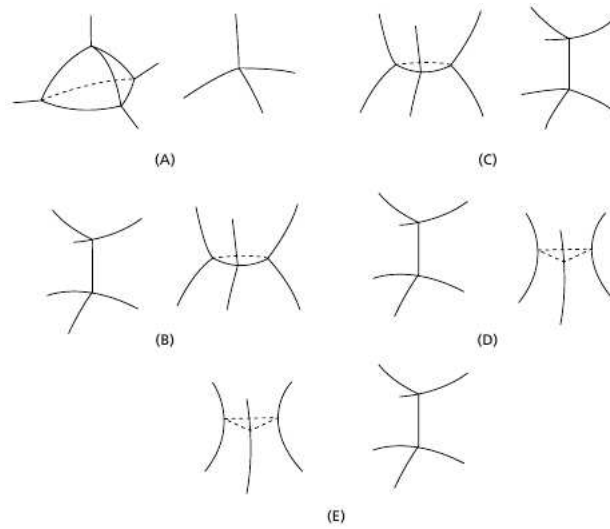


Figure 3.12: Five basic geometrical changes during grain growth [29, p. 244]

Fig. 3.12 [29, p. 244] image A shows a tetrahedral grain being consumed by the neighbouring grains. Image B shows the meeting of two grains forming a high angle boundary. Image C shows the separation of two grains which have a high angle boundary initially. Image D shows the meeting of two grains forming a low angle boundary, which could make a geometrical coalescence happen, so two grains become a larger grain. Image E shows one grain separating into two grains.

An empirical equation for isothermal grain growth is given by,

$$D - D_0 = kt^n, \quad (3.3)$$

where D is the growing grain size, D_0 is the initial grain size and t is the annealing time. k is a time independent constant but may depend on the level of previous deformation. n is also a time independent constant but generally increases with increasing annealing temperature. [29, p. 249] [22, p. 224] The log of growing grain diameter versus log of annealing time for brass at different annealing temperature is shown in Fig. 3.13 [22, p. 225].

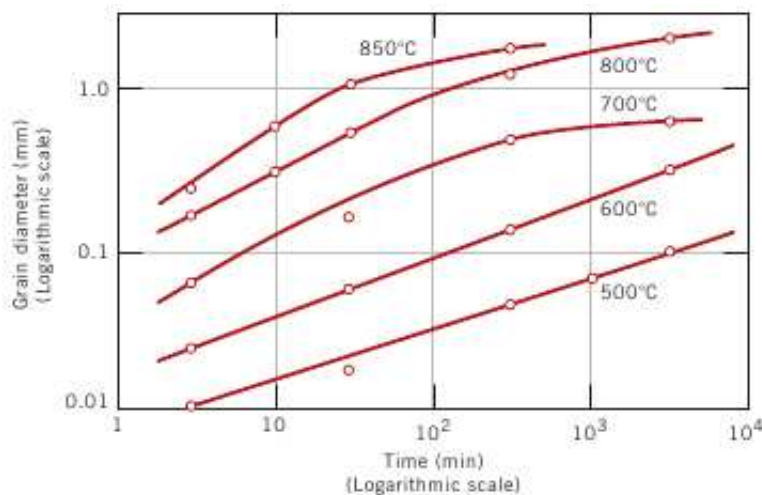


Figure 3.13: Growing grain diameters versus annealing time for brass [22, p. 225]

Impurity defects can inhibit grain growth. The effect of foreign inclusions retarding grain growth in aluminum is shown in Fig. 3.14 [29, p. 251].

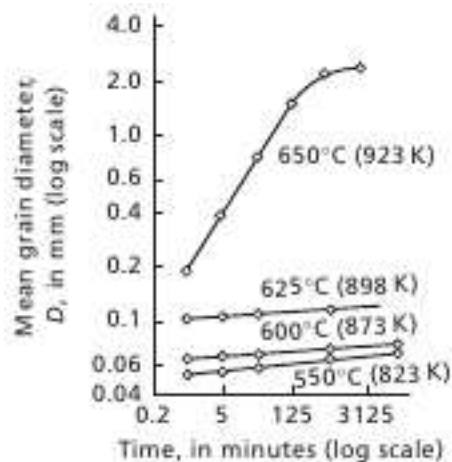


Figure 3.14: Retardation on grain growth in aluminum by second-phase inclusions [29, p. 251]

The aluminium has 1.1% manganese impurity, which forms second-phase inclusions MnAl_6 . The second-phase inclusions retard the grain growth up to 898 K. At 923 K MnAl_6 dissolves in the crystal, which has much less retardation on the grain growth. And at this relatively high temperature the exponent n in Eq. 3.3 is 0.42 close to the theoretical value 0.5 predicted by a mathematical model in reference [29, p. 247]. In another case the foreign inclusions may coalesce into fewer larger clusters at high temperature, which can also weaken the retardation of grain growth. For individual foreign atoms provided that the impurity percentage is not too high, high enough annealing tem-

perature will also weaken the retarding effects and the exponent n approaches the theoretical value 0.5. It is supposed that thermal vibration at high enough temperature breaks up the environments of foreign atoms.

Some other point defects have similar retarding effects such as holes or pores. The retarding effect of pores on grain growth is shown in Fig. 3.15 [29, p. 252]. The crystal is Remalloy (12% Co, 17% Mo and 71% Fe). A number of pores can be seen lying on the grain boundaries. In particular, several pores retard the boundary motion of the uppermost large grain towards the concave side. [29, p. 249-253]

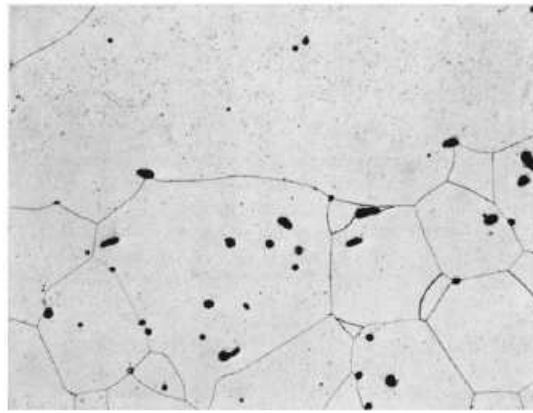


Figure 3.15: Retardation on grain growth by pores [29, p. 252]

When the grain size grows to a level comparable to the dimensions of samples, another important retardation on the growth appears. This is called thermal grooving and is shown in Fig. 3.16 [29, p. 254].

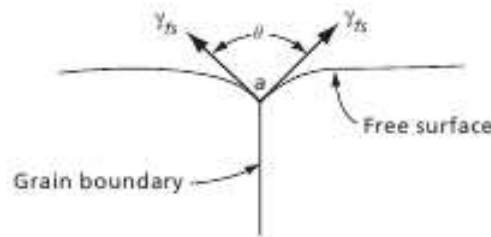


Figure 3.16: Thermal Grooving [29, p. 254]

The grain boundary attaches to the left surface and to the right. A certain amount of energy is required for the grain boundary to escape from the thermal grooving. This is the reason why the rate

of grain growth decreases after 625-minute annealing at 923 K in Fig. 3.14 [29, p. 251]. [29, p. 253-254]

With these inhibitions presented, if the annealing temperature is raised further above that at which the initial grain growth happens, secondary recrystallization will happen. Interestingly the grain growth due to secondary recrystallization is not affected by the retarding factors during the grain growth due to primary recrystallization. [29, p. 256]

3.1.5 Various Annealing Processes

There are five types of annealing processes, (i) Process Annealing or Partial Annealing, (ii) Stress Relief Annealing, (iii) Diffusion Annealing, (iv) Full Annealing and (v) Spheroidising Annealing. Full annealing and spheroidising annealing deal with carburised steel. The other three annealing processes are briefly described as follows,

(i) Process Annealing or Partial Annealing

Process annealing is used to remove the distortions induced by the cold works. It is also used in fabricating metals to avoid cracks. The controlled temperature allows recovery and recrystallization to happen but not grain growth to have a fine grain micro structure. To prevent oxidization the temperature cannot be too high or it must be processed in a non-oxidizing atmosphere.

(ii) Stress Relief Annealing

Internal residual stresses may remain in crystals due to, (1) plastic deformation processes, (2) nonuniformly cooling down crystals from hot works or (3) phase transformations during cooling down. These stresses may lead to distortions or warpages. To relieve the stresses the crystals are soaked at an elevated temperature provided that this temperature will not affect any result from other processes. Following the soak, the crystals are cooled down to room temperature in a prepared atmosphere. [22, p. 422-423] [21, p. 322-324]

(iii) Diffusion Annealing

When alloyed crystals grow, the chemical compositions may non-uniformly distribute, particularly liquation inhomogeneities (Non-equilibrium solidification from liquid phase to solid phase [31, p. 114-115]. Liquation regions have high hardness. As the annealing temperature or time increases,

the overall hardness decreases and the crystal dendrites are smeared. [32, p. 159]

3.2 Review of Annealing Effects on URu_2Si_2

Since the defects in crystals do have a significant effect on their properties, removing the defects by annealing may change these properties to a considerable level.

Menovsky *et al.* measured the resistivity of URu_2Si_2 for annealed single crystal and unannealed single crystal. They also cited the measurements of annealed polycrystal from other groups. The results are shown in Table 3.2. [33]

Table 3.2: Annealing Effects on Resistivity of URu₂Si₂ [33]

Sample	Distance from seed (mm)	Orientation (parallel to axis)	ρ_{300K} $\mu\Omega \cdot cm$	$\rho_{4.2K}$ $\mu\Omega \cdot cm$	$\rho_{300K}/\rho_{4.2K}$
Single Crystal Annealed (900 °C / 7 days)	25	a	356	27.3	14.05
	30	c	161	24	6.7
	55	c	166	-	-
	55	a	300.4	15.35	19.57
	70	a	376.2	24.13	15.59
	73	c	158	18.4	8.6
	105	c	179.7	-	-
	110	a	327.5	18.13	18.06
Single Crystal Unannealed (other batch)		a	330	32	10.31
		c	170	32	5.31
Polycrystal Annealed (1000 °C / 100 Hours)			~ 430	~ 50	8.6
Polycrystal Annealed (900 °C / 7 days)			~ 2460	~ 120	20

It seems the resistivities for annealed single crystals at different distances from the seed vary considerably. They claim three factors may cause such large variation, the compositional gradients along the crystal growing direction as a result of the Czochralski method, crystalline defects, and nonuniformly distributed impurities. They also claim that ρ_{300K} has no significant change by annealing and $\rho_{300K}/\rho_{4.2K}$ increases mainly due to the decreasing of $\rho_{4.2K}$. The resistivities of polycrystals are larger than those of single crystals by a factor of 1.5 to nearly 10. They propose that polycrystals may have significantly more microcracks and impurities.

B. Fåk *et al.* grew two single crystals also by the Czochralski method. They kept one as grown and annealed the other wrapped in a tantalum foil under vacuum (5×10^{-7} Torr) at 950°C for eight days. [34] There are some significant differences between the two in several kinds of measurements. The heat capacity measurements are shown in Fig. 3.17 [34].

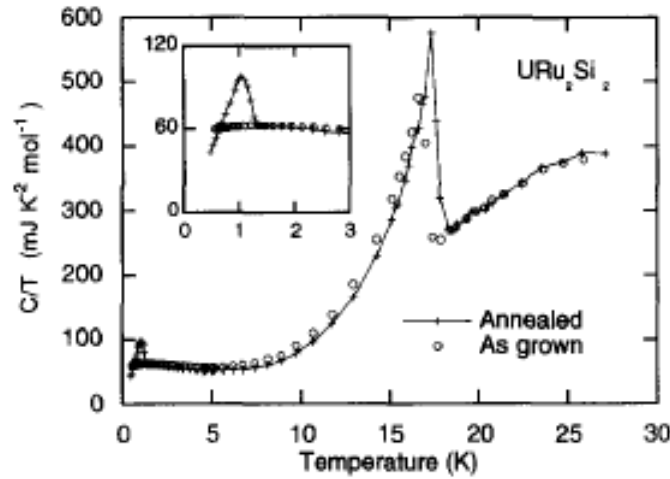


Figure 3.17: Specific Heat Capacities of the annealed URu_2Si_2 and the as-grown URu_2Si_2 [34]

The hidden order temperature, T_{HO} , of the as-grown sample is 17.1 K and T_{HO} for the annealed sample is 17.6 K . One big difference is that the annealed sample shows the superconducting transition at 1.2 K but the as-grown sample doesn't show the SC transition down to 0.3 K .

The resistivity measurements along the a-axis are shown in Fig. 3.18 [34].

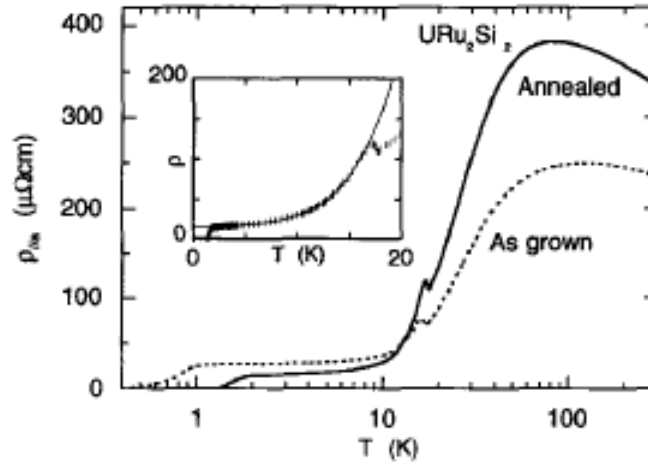


Figure 3.18: Resistivities of the annealed URu_2Si_2 and the as-grown URu_2Si_2 [34]

The resistivity measurements of both show a SC transition but T_c for the annealed sample is 1.6 K and T_c for the as-grown sample is 0.75 K. Their fittings show that the residual resistivity ρ_0 for the annealed sample is $14.9 \mu\Omega \cdot \text{cm}$ and ρ_0 of the as-grown sample is $27.0 \mu\Omega \cdot \text{cm}$. The higher ρ_0 of the as-grown sample is claimed to be caused by its larger amount of crystal defects. A surprising difference is that the annealed sample has a maximum resistivity of $380 \mu\Omega \cdot \text{cm}$ at its coherence temperature, T_{coh} , but the as-grown sample has a smaller maximum of $250 \mu\Omega \cdot \text{cm}$ at its T_{coh} . And below some temperature around 10 K the resistivity of the annealed sample appears to be smaller than that of the as-grown sample.

The DC magnetic susceptibility measurements are shown in Fig. 3.19 [34].

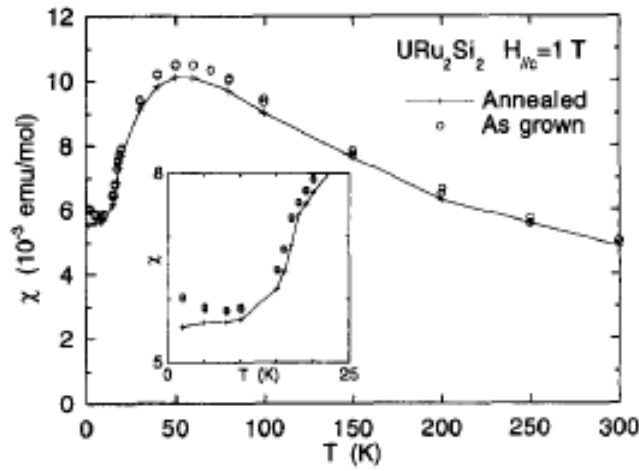


Figure 3.19: DC magnetic susceptibility of the annealed URu_2Si_2 and the as-grown URu_2Si_2 [34]

The 1 T field direction is along the c-axis. There are no significant differences from 2 K to 300 K.

However the as-grown sample has a small upturn at lower temperature. This upturn is claimed to be caused by the crystal defects because heavy fermions are sensitive to dislocations and stacking faults, which affect $5f$ electrons at uranium sites.

The elastic neutron scattering measurements are shown in Fig. 3.20 [34].

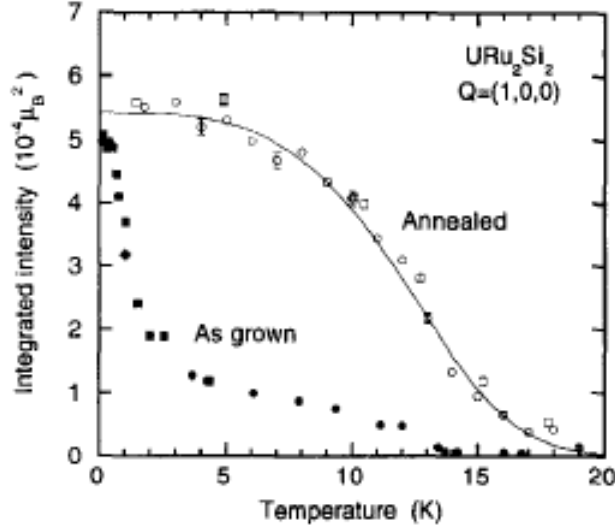


Figure 3.20: Elastic Neutron Scattering of the annealed URu_2Si_2 and the as-grown URu_2Si_2 [34]

The Bragg reflection plane is (100) . The integrated intensity is the square of the magnetic moment. The magnetic moment of the annealed sample increases as the temperature decreases from 20 K and saturates at low temperature. The as-grown doesn't show a magnetic moment between 14 K and 20 K and its magnetic moment increases much more slowly as the temperature decreases from 14 K to 2 K . Between 5 K and 10 K the normalized magnetic moment of the as-grown sample is five times smaller than that of the annealed sample. The magnetic moment of the as-grown sample suddenly increases below 2 K and saturates close to that of the annealed sample at 0.5 K . The difference of T_{HO} determined by specific heat capacity and elastic neutron scattering is about 2 K for the annealed sample while it is about 3 K for the as-grown sample. [34]

Honma *et al.* also measured the resistivities of an as-grown single crystal of URu_2Si_2 and an annealed crystal. The crystals were grown by the Czochralski method too. The samples were wrapped in tantalum and zirconium foils and were annealed under vacuum of $1 \times 10^{-7}\text{ Torr}$ at 1000°C for one week. The resistivities were measured along the a -axis from 0.5 K to 300 K . [35] The measurements below 6 K are shown in Fig. 3.21 [35].

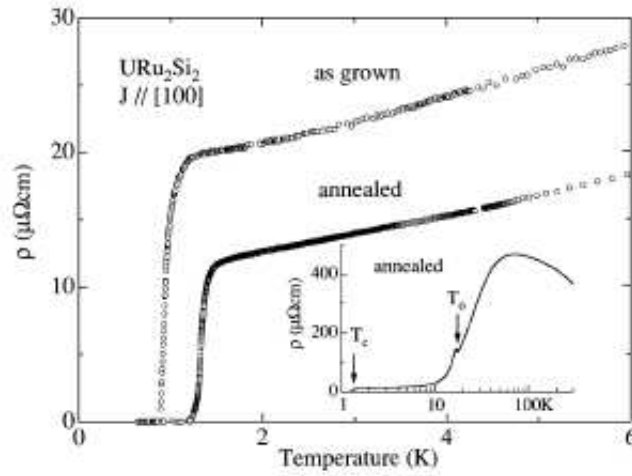


Figure 3.21: Resistivities of the annealed URu_2Si_2 and the as-grown URu_2Si_2 from Honma et al. [35]

The SC transition width of the as-grown sample is between 0.82 K and 1.2 K while it is between 1.2 K and 1.5 K for the annealed sample. The residual resistivity ratio (RRR defined as the resistivity at room temperature ρ_{RT} divided by the residual resistivity ρ_0) for the as-grown sample is 19 while it is 40 for the annealed sample. [35]

Chapter 4

^3He Refrigerator

The cryostat used for all temperature dependent measurements is a ^3He Refrigerator, which is a multistage cooling system [36]. One temperature sensor at the sample stage is used for $T > 6\text{ K}$ and the other one at the bolometer stage is used for $T < 6\text{ K}$. Below 2 K the temperature at the sample stage is somehow higher than at the bolometer stage. The outer view of the cryostat is shown in Fig. 4.1a [37]. The inner view of the cryostat is shown in Fig. 4.1b [37].



Figure 4.1a: Cryostat Outer View [37]

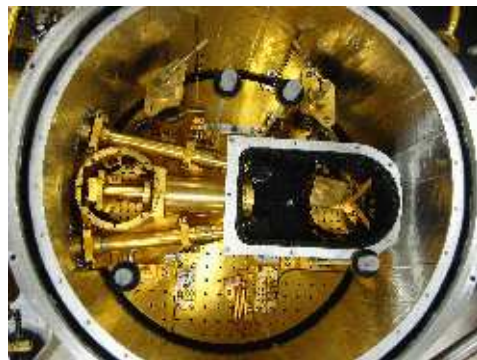


Figure 4.1b: Cryostat Inner View [37]

The explanatory drawings of inner view of ^3He refrigerator are shown in Fig. 4.2a [38, p. 26].

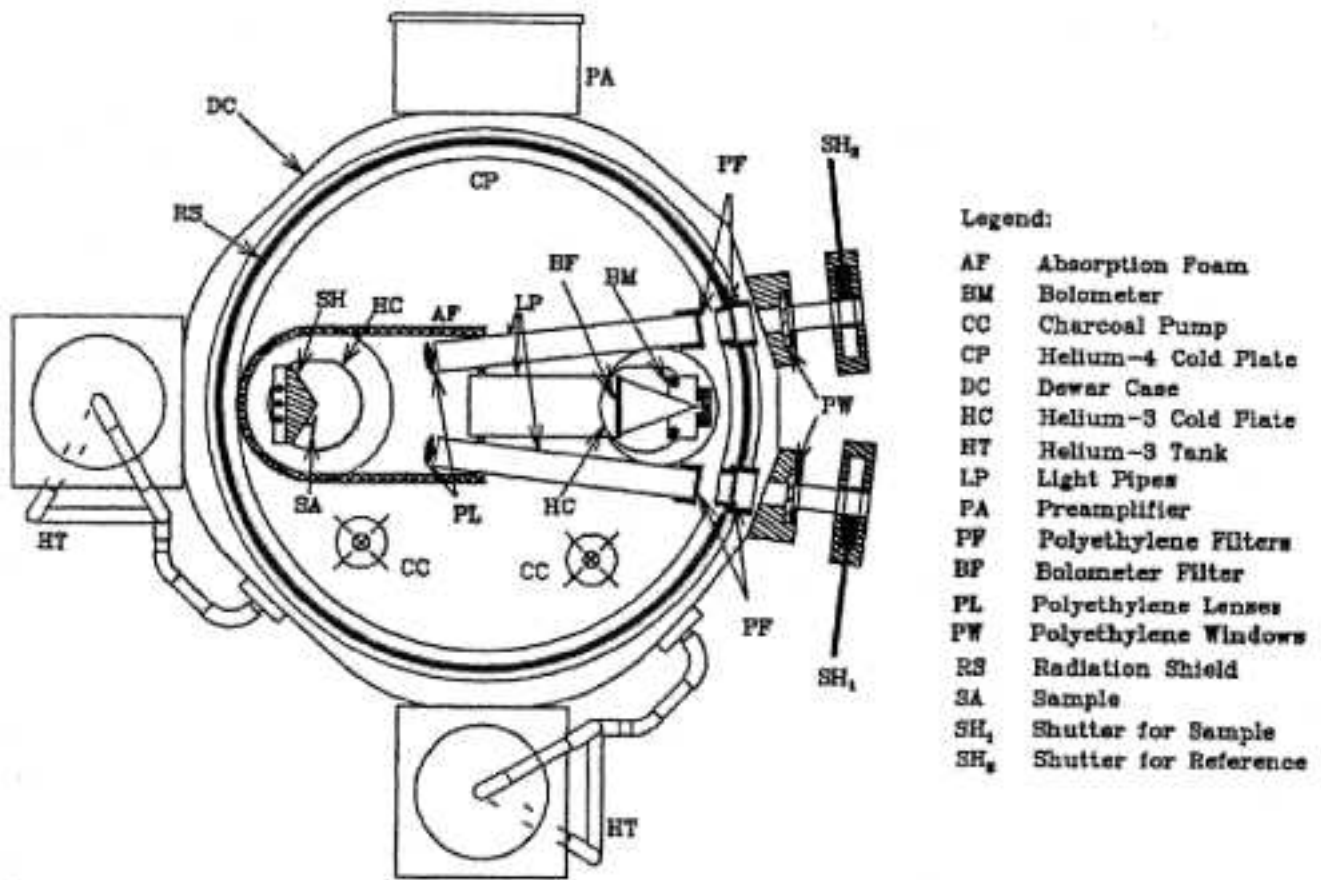
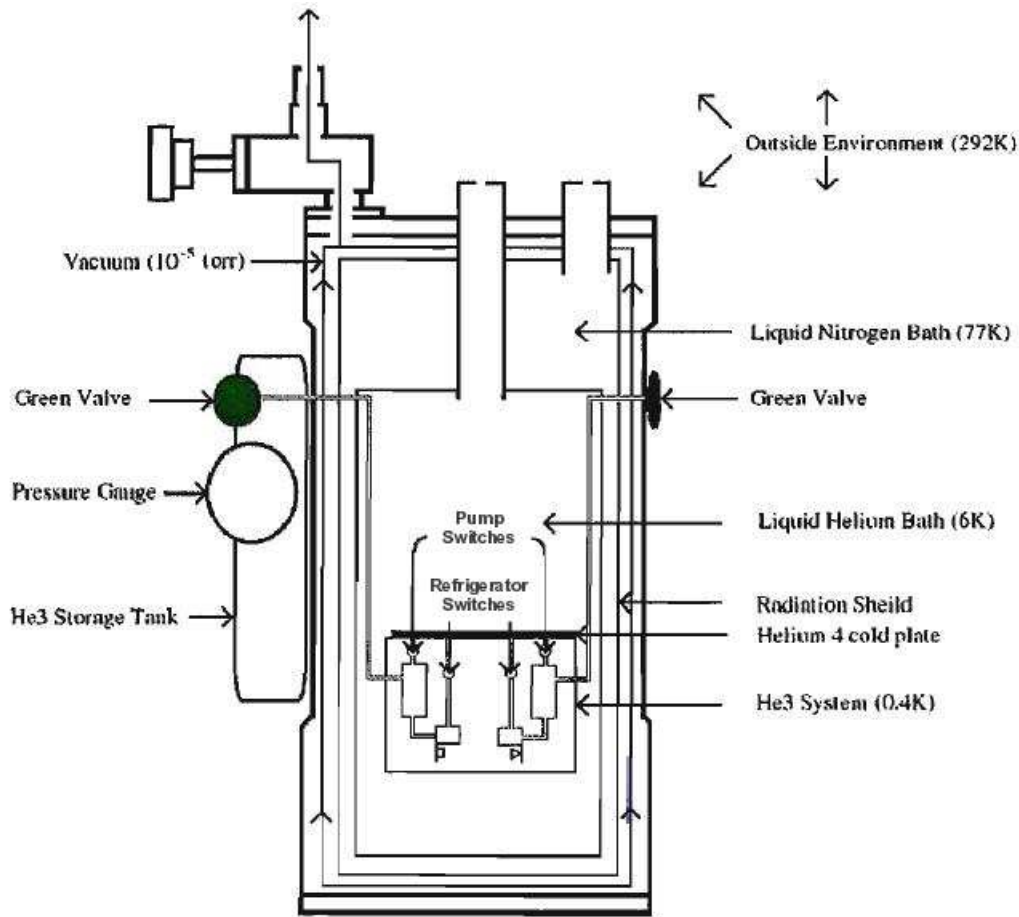


Figure 4.2a: Bolometer Stage and Sample Stage of ^3He Refrigerator [38, p. 26]

The side view of of ^3He refrigerator are shown in Fig. 4.2b [39, p. 26].

Figure 4.2b: Side View of ^3He Refrigerator [39, p. 34]

The procedure used to cool the cryostat to temperature below 1 K is the following,

Stage 1:

By using a rough pump the pressure in the cryostat is reduced from ambient pressure to 10^{-3} Torr. The pressure is then further reduced to 10^{-5} Torr or less using a turbomolecular pump.

Stage 2:

Before initiating the cooling process, the four heat switches labeled in Fig. 4.2b [39, p. 26] are closed, namely sample stage pump switch, sample stage refrigerator switch, bolometer stage pump switch and bolometer stage refrigerator switch. This ensures that the sample stage, the bolometer stage, the sample stage charcoal and the bolometer stage charcoal are in equilibrium with the temperature of the Helium vessel. Furthermore the green valves connecting the two ^3He storage cylinders with the ^3He bath inside the cryostat need to be open so the ^3He can be driven from the cylinders onto the cold charcoal during the cooling process described next. The green valves are

labeled in Fig. 4.2b.

Both the nitrogen vessel and the helium vessel are filled with liquid nitrogen so the temperature of the system decreases from the ambient temperature to the boiling point of nitrogen 77 K .

Stage 3:

After about two hours, when the system reaches temperature equilibrium at 77 K , the liquid nitrogen in the helium vessel is extruded into a storage container by pressurizing with nitrogen gas. Then the system is flushed by using nitrogen gas firstly and ^4He gas secondly to remove any liquid nitrogen residue at the bottom of the helium vessel. This procedure is to prevent any liquid nitrogen residue from solidifying when we transfer ^4He . The melting point of nitrogen is 63.15 K under ambient pressure [40, p. 51]. The boiling point of ^4He is 4.2 K under ambient pressure [41].

Stage 4:

Liquid ^4He is transferred from a storage container to the emptied helium vessel through a U-shape transfer tube.

Stage 5:

When the temperature of the system is cooled down to 4.2 K , a rough pump is used to pump on the liquid ^4He so the temperature can go down further. Above the λ point $\approx 2.17\text{ K}$ under saturated pressure ^4He is a normal fluid [42, p. 115] and the evaporative cooling is explained by the Clausius-Clapeyron equation [43],

$$\ln P = -\frac{\Delta H_{\text{vap}}}{RT} + \text{const.} \quad [43]. \quad (4.1)$$

It relates the pressure and temperature of the co-existing phases of liquid and gas. P is the pressure. ΔH_{vap} is the enthalpy change per mole on vapourization. R is the Universal Gas Constant. T is the temperature. The constant is the intercept of plotting $\ln P$ vs $\frac{1}{T}$. As the pressure goes down, the temperature decreases. The pumping continues until the temperature reaches approximately 2 K which is below the boiling point of ^3He (3.2 K under ambient pressure [41]).

Meanwhile the bolometer stage charcoal pump and/or the sample stage charcoal pump need to be isolated from the ^4He bath. The charcoal is then heated so that the ^3He stored during the previous cooling process is released and condenses into the ^3He bath. Before heating the charcoal the

green valves discussed above need to be closed so the released ^3He will not flow back to its storage cylinders. The charcoal temperature is indicated by a resistor mounted on its storage vessel. The heating of charcoal continues until its temperature rises to 30 K and the resistor decreases to 2.5 $k\Omega$.

Stage 6:

Pumping on the ^4He bath and heating of the charcoal pumps are stopped. The bolometer stage refrigerator and/or the sample stage refrigerator switches are opened to isolate the ^3He bath from the ^4He bath. The bolometer stage pump and/or the sample stage pump switches are connected to the ^4He bath so that the charcoal becomes colder. ^3He vapour will be adsorbed onto the cold charcoal from the ^3He bath resulting in a lowering of the pressure of the vapour above the ^3He bath. This process of pumping on the ^3He bath makes the temperature decrease approximately to 0.3 K , which again is explained by the Clausius-Clapeyron equation [43] above the superfluid transition temperature of ^3He which is about 2 mK [42, p. 124–p. 125].

Stage 7:

The temperature can be maintained at about 0.3 K until all ^3He is adsorbed by the cold charcoal. After that the temperature will increase drastically and the green valves leading to the ^3He storage cylinder need to be opened before the temperature rises so that as the charcoal gets warmer, the released ^3He can flow back to the ^3He storage cylinder. The bolometer stage refrigerator and/or the sample stage refrigerator heat switches then need to be closed so that the bolometer stage and/or the sample stage contacts the ^4He bath and all stages reach thermal equilibrium with the ^4He cold plate. When the pressure inside the ^4He vessel goes back to ambient pressure, the valve used to close it off from the rough pump must be opened so that the ^4He bath can boil off safely. This prevents the pressure in the enclosed vessel to accumulate to a dangerous level. If there is still some ^4He in the ^4He vessel, a 100 Ω resistor can be used to gently apply heat to the cold plate of the vessel to evaporate the ^4He so that the temperature does not stay at the ^4He boiling point too long. It may take two days for the temperature to raise back to room temperature, ensuring good thermal equilibrium.

Chapter 5

Resistivity Measurement

5.1 Van der Pauw Method

The Van der Pauw Method is a technique used to measure the resistivity of a sample of arbitrary shape [44–46], provided that the following conditions are satisfied,

- (1) The contacts are on the perimeter of the sample.
- (2) The contacts are sufficiently small.
- (3) The sample is homogeneous in thickness.
- (4) The surface of the sample is singly connected without isolated holes.

5.1.1 Four Contacts in One Dimension

Consider four contacts M, N, O and P are in a line on a real axis x at the edge of an Upper Half Complex Plane Z as shown in Fig. 5.1. The sample is in the Upper Half Plane (UHP). And $x_N - x_M = a$, $x_O - x_N = b$ and $x_P - x_O = c$.

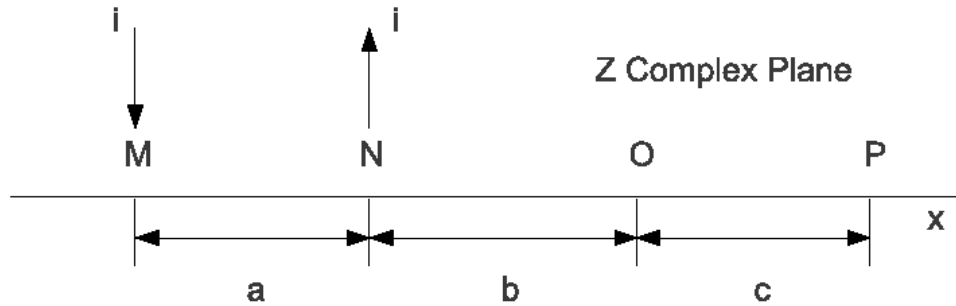


Figure 5.1: Upper Half Complex Plane

Let a current i enter into M and exit out of N. Firstly we consider the entering current density J_{ent} .

at a point z , which has a distance r_M from $M(x_M, 0)$,

$$\vec{r}_M = \vec{z} - \vec{M} \quad [47, \text{p. 168–p. 170}], \quad (5.1)$$

$$\vec{J}_{ent.} = \frac{i}{\vec{A}} = \frac{i}{\pi \vec{r}_M d} \quad [45] \quad [47, \text{p. 168–p. 170}], \quad (5.2)$$

assuming i flows radially. \vec{A} is the cross section of current i . d is the sample thickness. Secondly we consider the exiting current density J_{exit} at the point z , which has distance r_N from $N(x_N, 0)$,

$$\vec{r}_N = \vec{z} - \vec{N} \quad [47, \text{p. 168–p. 170}], \quad (5.3)$$

$$\vec{J}_{exit} = \frac{i}{\vec{A}} = \frac{i}{\pi \vec{r}_N d} \quad [45] \quad [47, \text{p. 168–p. 170}]. \quad (5.4)$$

Then the vector sum of the two current densities at the point z is,

$$\vec{J}_{sum} = \vec{J}_{ent.} - \vec{J}_{exit} = \frac{i}{\pi \vec{r}_M d} - \frac{i}{\pi \vec{r}_N d} \quad [45] \quad [47, \text{p. 168–p. 170}]. \quad (5.5)$$

The generalized Ohm's law is,

$$\vec{J} = \sigma \vec{E}, \quad (5.6a)$$

where σ is the electrical conductivity, which is the reciprocal of electric resistivity ρ . \vec{E} is the applied electric field. The negative gradient operator $-\vec{\nabla}$ of potential U gives \vec{E} ,

$$\vec{E} = -\vec{\nabla} U, \quad (5.6b)$$

so we have,

$$\vec{J}_{sum} \rho = -\vec{\nabla} U. \quad (5.7)$$

To calculate the potential difference between O and P ($U_P - U_O$), we need to take the line integral of the vector sum \vec{J}_{sum} and for simplicity we choose the shortest line between O and P, namely from

x_O to x_P along the x axis,

$$\begin{aligned}
 U_P - U_O &= -\rho \int_{x_O}^{x_P} \left(\frac{i}{\pi \vec{r}_M d} - \frac{i}{\pi \vec{r}_N d} \right) dx \\
 &= -\rho \int_{x_O}^{x_P} \left[\frac{i}{\pi(\vec{x} - \vec{M})d} - \frac{i}{\pi(\vec{x} - \vec{N})d} \right] dx \\
 &= \frac{i\rho}{d\pi} \ln \left\{ \frac{(x_P - x_N)(x_O - x_M)}{(x_P - x_M)(x_O - x_N)} \right\} \\
 &= \frac{i\rho}{d\pi} \ln \left\{ \frac{(b+c)(a+b)}{(a+b+c)b} \right\} \quad [45] \quad [47, \text{p. 171}].
 \end{aligned} \tag{5.8}$$

a is the distance between M and N. b is the distance between N and O. c is the distance between O and P. So the resistance $R_{MN,OP}$ is given by,

$$R_{MN,OP} = \frac{U_P - U_O}{i} = \frac{\rho}{d\pi} \ln \left\{ \frac{(b+c)(a+b)}{(a+b+c)b} \right\} \quad [45] \quad [47, \text{p. 171}]. \tag{5.9}$$

Rearranging Equation 5.9 we get,

$$\exp\left(-\frac{d\pi}{\rho} R_{MN,OP}\right) = \frac{(a+b+c)b}{(b+c)(a+b)} \quad [45] \quad [47, \text{p. 172}]. \tag{5.10}$$

Next let the current i enter into N and exit out of O. Similarly we consider the entering current density, the exit current density and the vector sum \vec{J}_{sum} of the two current densities at a point z . Then by taking the line integral of the vector sum along the shortest distance from x_P to x_M along the x axis we have the potential difference between P and M,

$$\begin{aligned}
 U_M - U_P &= -\rho \int_{x_P}^{x_M} \left(\frac{i}{\pi \vec{r}_N d} - \frac{i}{\pi \vec{r}_O d} \right) dx \\
 &= -\rho \int_{x_P}^{x_M} \left[\frac{i}{\pi(\vec{x} - \vec{N})d} - \frac{i}{\pi(\vec{x} - \vec{O})d} \right] dx \\
 &= \frac{i\rho}{d\pi} \ln \left\{ \frac{(x_M - x_O)(x_P - x_N)}{(x_M - x_N)(x_P - x_O)} \right\} \\
 &= \frac{i\rho}{d\pi} \ln \left\{ \frac{(b+c)(-(a+b))}{c(-a)} \right\} \quad [45] \quad [47, \text{p. 172}],
 \end{aligned} \tag{5.11}$$

so the resistance $R_{NO,PM}$ is given by,

$$R_{NO,PM} = \frac{U_M - U_P}{i} = \frac{\rho}{d\pi} \ln \left\{ \frac{(b+c)(a+b)}{ca} \right\} \quad [45] \quad [47, \text{p. 172}]. \quad (5.12)$$

Rearranging Equation 5.12 we get,

$$\exp \left(-\frac{d\pi}{\rho} R_{NO,PM} \right) = \frac{ca}{(b+c)(a+b)} \quad [45] \quad [47, \text{p. 172}]. \quad (5.13)$$

Summing both sides of Eq. 5.10 and Eq. 5.13, we get,

$$\begin{aligned} \exp \left(-\frac{d\pi}{\rho} R_{MN,OP} \right) + \exp \left(-\frac{d\pi}{\rho} R_{NO,PM} \right) &= \frac{(a+b+c)b}{(b+c)(a+b)} + \frac{ca}{(b+c)(a+b)} \\ &= \frac{(a+b+c)b + ca}{(b+c)(a+b)} \\ &= 1 \quad [45] \quad [47, \text{p. 172}]. \end{aligned} \quad (5.14)$$

This is the Van der Pauw theorem in one dimension.

5.1.2 Four Contacts in Two Dimensions

To extend the Van der Pauw theorem to the edge along an arbitrary shape in two dimensions as shown in Fig. 5.2, we invoke the method of Conformal Mapping.

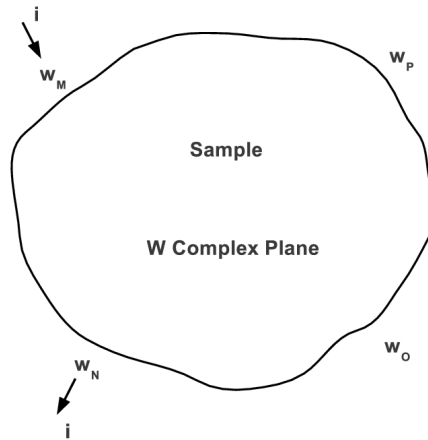


Figure 5.2: W Complex Plane

The general idea is to find a pair of transform functions relating the points M, N, O and P in the Z complex plane to the one-by-one corresponding points w_M , w_N , w_O and w_P in another complex plane W [45] [47, p. 172–p. 173]. We will have a pair of transform functions,

$$w = f(z), \quad (5.15a)$$

$$z = g(w). \quad (5.15b)$$

In the Z plane we have the potential difference between O and P,

$$U_P - U_O = \frac{i\rho}{d\pi} \ln \left\{ \frac{(x_P - x_N)(x_O - x_M)}{(x_P - x_M)(x_O - x_N)} \right\}. \quad (5.16)$$

Then we transform M, N, O and P to w_M , w_N , w_O and w_P by $z = g(w)$. The result is,

$$U_{w_P} - U_{w_O} = \frac{i\rho}{d\pi} \ln \left\{ \frac{[g(w_P) - g(w_N)][g(w_O) - g(w_M)]}{[g(w_P) - g(w_M)][g(w_O) - g(w_N)]} \right\}. \quad (5.17)$$

The resistance $R_{w_M w_N, w_O w_P}$ in the W plane is thus,

$$\begin{aligned} R_{w_M w_N, w_O w_P} &= \frac{U_{w_P} - U_{w_O}}{i} \\ &= \frac{\rho}{d\pi} \ln \left\{ \frac{[g(w_P) - g(w_N)][g(w_O) - g(w_M)]}{[g(w_P) - g(w_M)][g(w_O) - g(w_N)]} \right\}. \end{aligned} \quad (5.18)$$

For mapping from the W plane to the Z plane by using $w = f(z)$ we will have $w_M = f(x_M)$, $w_N = f(x_N)$, $w_O = f(x_O)$, and $w_P = f(x_P)$ and also $z = g(w) = g(f(z))$ so,

$$\begin{aligned} R_{w_M w_N, w_O w_P} &= \frac{\rho}{d\pi} \ln \left\{ \frac{[g(f(x_P)) - g(f(x_N))][g(f(x_O)) - g(f(x_M))]}{[g(f(x_P)) - g(f(x_M))][g(f(x_O)) - g(f(x_N))]} \right\} \\ &= \frac{\rho}{d\pi} \ln \left\{ \frac{(x_P - x_N)(x_O - x_M)}{(x_P - x_M)(x_O - x_N)} \right\} \\ &= \frac{\rho}{d\pi} \ln \left\{ \frac{(b+c)(a+b)}{(a+b+c)b} \right\} \quad [45] [47, p. 173], \end{aligned} \quad (5.19)$$

for which the resistance value is invariant under the transformation. Similarly we can find the value

of the resistance $R_{w_N w_O, w_P w_M}$ which is also invariant under the transformation. Hence the Van der Pauw theorem is valid in two dimensions.

Mahan used a Conformal Mapping method called Schwarz-Christoffel transformation in his book to extend the Van der Pauw theorem to the vortices of a polygon in two dimensions [47, p. 173]. The generalized transform function $w = f(z)$ for Schwarz-Christoffel transformation is,

$$w = w_0 + A \int_{-\infty}^{+\infty} \frac{1}{\prod_j (z - z_j)^{\frac{\phi_j}{\pi}}} dz \quad [47, \text{p. 158}]. \quad (5.20)$$

The subscript j is the number of pairs of points in the two complex planes. The angle ϕ_j is between two boundaries at the vortex j in a counterclockwise direction. The constants w_0 and A are determined by the values of the points in a pair [47, p. 158].

5.1.3 f factor in Van der Pauw theorem

Following from Van der Pauw's second paper regarding his theorem [45], we next derive Eq. (4) of this second paper, which is used in our resistivity measurement.

Let

$$R_{MN,OP} d\pi = \alpha, \quad (5.21a)$$

and

$$R_{NO,PM} d\pi = \beta, \quad (5.21b)$$

[45] and substitute into Eq. 5.22

$$\exp\left(-\frac{d\pi}{\rho} R_{MN,OP}\right) + \exp\left(-\frac{d\pi}{\rho} R_{NO,PM}\right) = 1 \quad [45], \quad (5.22)$$

so we have

$$\exp\left(-\frac{\alpha}{\rho}\right) + \exp\left(-\frac{\beta}{\rho}\right) = 1 \quad [45]. \quad (5.23)$$

Let

$$\alpha = \frac{1}{2}[(\alpha + \beta) + (\alpha - \beta)], \quad (5.24a)$$

$$\beta = \frac{1}{2}[(\alpha + \beta) - (\alpha - \beta)], \quad (5.24b)$$

[45] and substitute Eq. 5.24a and Eq. 5.24b into Eq. 5.23 so we have

$$\exp\left(-\frac{(\alpha + \beta) + (\alpha - \beta)}{2\rho}\right) + \exp\left(-\frac{(\alpha + \beta) - (\alpha - \beta)}{2\rho}\right) = 1 \quad [45], \quad (5.25)$$

and factor out $\exp(-\frac{\alpha+\beta}{2\rho})$ and we have

$$\exp\left(-\frac{\alpha + \beta}{2\rho}\right) \left[\exp\left(-\frac{\alpha - \beta}{2\rho}\right) + \exp\left(\frac{\alpha - \beta}{2\rho}\right) \right] = 1 \quad [45], \quad (5.26)$$

and divide both sides by 2 so we have

$$\exp\left(-\frac{\alpha + \beta}{2\rho}\right) \left[\frac{\exp\left(-\frac{\alpha - \beta}{2\rho}\right) + \exp\left(\frac{\alpha - \beta}{2\rho}\right)}{2} \right] = \frac{1}{2}, \quad (5.27a)$$

$$\exp\left(-\frac{\alpha + \beta}{2\rho}\right) \cosh\left(\frac{\alpha - \beta}{2\rho}\right) = \frac{1}{2}, \quad (5.27b)$$

$$\exp\left(-\frac{\alpha + \beta}{2\rho}\right) \cosh\left[\frac{(\alpha - \beta)(\alpha + \beta)}{2\rho(\alpha + \beta)}\right] = \frac{1}{2}, \quad (5.27c)$$

$$\exp\left[-\frac{\alpha + \beta}{2\rho}\right] \cosh\left[\frac{\beta(\frac{\alpha}{\beta} - 1)(\alpha + \beta)}{2\rho\beta(\frac{\alpha}{\beta} + 1)}\right] = \frac{1}{2}, \quad (5.27d)$$

[45] and let

$$\frac{\alpha + \beta}{2\rho} = \frac{\ln 2}{f} \quad [45]. \quad (5.28)$$

Making this substitution in Eq. 5.27d we have,

$$\exp\left(-\frac{\ln 2}{f}\right) \cosh\left[\frac{\left(\frac{\alpha}{\beta} - 1\right)}{\left(\frac{\alpha}{\beta} + 1\right)} \times \frac{\ln 2}{f}\right] = \frac{1}{2} \quad [45], \quad (5.29)$$

substituting Eq. 5.21a and Eq. 5.21b into Eq. 5.29 so we have,

$$\exp\left(-\frac{\ln 2}{f}\right) \cosh\left[\frac{\left(\frac{R_{MN,OP}}{R_{NO,PM}} - 1\right)}{\left(\frac{R_{MN,OP}}{R_{NO,PM}} + 1\right)} \times \frac{\ln 2}{f}\right] = \frac{1}{2} \quad [45], \quad (5.30)$$

and rearranging,

$$\cosh\left[\frac{\left(\frac{R_{MN,OP}}{R_{NO,PM}} - 1\right)}{\left(\frac{R_{MN,OP}}{R_{NO,PM}} + 1\right)} \times \frac{\ln 2}{f}\right] = \frac{1}{2} \exp\left(\frac{\ln 2}{f}\right) \quad [45]. \quad (5.31)$$

Eq. 5.31 gives the relation between $\frac{R_{MN,OP}}{R_{NO,PM}}$ and the f factor [45]. Rearranging Eq. 5.28 we have,

$$\rho = \left(\frac{\alpha + \beta}{2 \ln 2}\right) \times f \quad [45], \quad (5.32)$$

substituting Eq. 5.21a and 5.21b into Eq. 5.32 so we have,

$$\rho = \frac{\pi d}{\ln 2} \frac{(R_{MN,OP} + R_{NO,PM})}{2} f \quad [45], \quad (5.33)$$

which is Eq. (4) in Van der Pauw's second paper [45]. Eq. 5.31 has no analytic solution. Van der Pauw gave a graphic solution in his paper, which is reproduced in Fig. 5.3 [45],

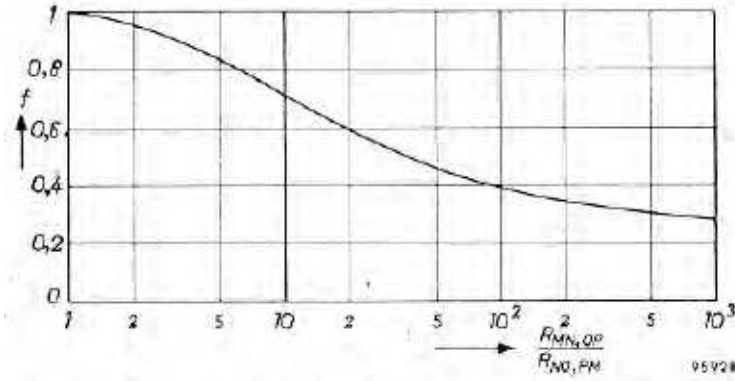


Figure 5.3: f factor as a function of $R_{MN,OP}/R_{NO,PM}$ [45]

In our measurement we use an algorithm written in Pascal to give a numerical solution for the

f factor. Rearranging Eq. 5.31 we obtain,

$$\exp\left(\frac{-2\ln 2}{f(1 + \frac{1}{R_{MN,OP}/R_{NO,PM}})}\right) + \exp\left(\frac{-2\ln 2}{f(1 + \frac{R_{MN,OP}}{R_{NO,PM}})}\right) = 1. \quad (5.34)$$

The initial minimum and maximum values of f are set as 0 and 1 respectively. The trial f value is set as $\frac{f_{min}+f_{max}}{2}$ so the initial f value is 0.5. If 0.5 makes the left side of Eq. 5.34 smaller than 1, then f_{min} is set as 0.5 and f_{max} is still 1. The new f value 0.75 is substituted into Eq. 5.34 and the output from the left side will be compared with 1 again. On the other hand if 0.5 makes the left side of Eq. 5.34 larger than 1, then f_{max} will be set as 0.5 and f_{min} remains 0. The new f value 0.25 is substituted into Eq. 5.34 and the output from the left side will be compared with 1 again. If the new trial f value makes the output smaller than 1, the next f_{min} is set as this f value and f_{max} remains unchanged. If the new trial f value makes the output larger than 1, the next f_{max} is set as this f value and the next f_{min} remains unaltered. The loop for the comparison will continue until the absolute value of the difference between the output and 1 is less than 10^{-6} or the number of iterations reaches 100.

5.2 Experimental Methods

The set up for mounting the sample is shown in Fig. 5.4.

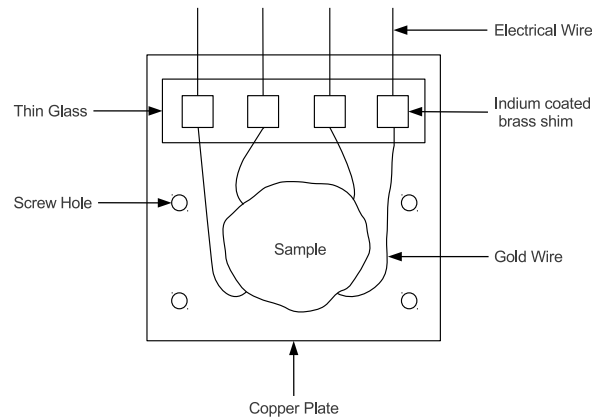
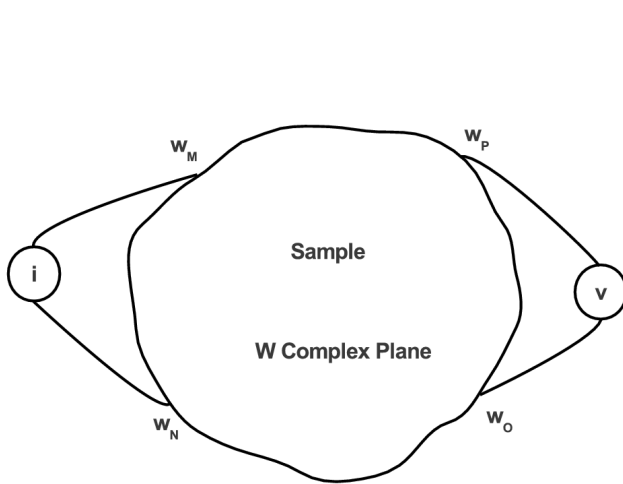
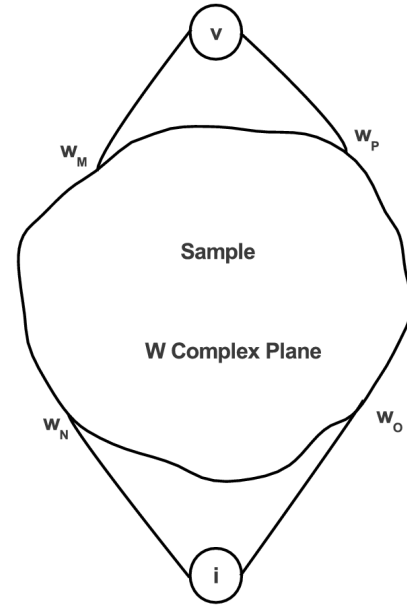


Figure 5.4: Set Up of Sample

It is essential to mount samples using a good thermal bonding which has high thermal conductivity so the samples can be effectively cooled down especially at low temperature. A sample is mounted on the copper plate by double-sided tape, VGE-7031 or five-minute epoxy, which also acts as an insulator between the sample and the copper plate. The thermal conductivity for VGE-7031 is $0.034 \text{ W}/(m \cdot K)$ at 1 K and $0.062 \text{ W}/(m \cdot K)$ at 4.2 K respectively [48]. The thermal conductivities for the double-sided tape and the five-minute epoxy used for the measurements are not available.

Four indium coated brass shims are epoxied to a thin piece of glass and the glass is epoxied to the copper plate. The glass needs to be thin enough to conduct heat from the indium contacts to the copper plate effectively. Four gold wires are attached to the four contacts near the circumference of the sample by silver paint under a microscope. A great effort is required to make good contacts. The other ends of the gold wires are soldered to the four indium contacts respectively. The indium contacts are connected to four pins respectively, which will be inserted into a mating connector inside the cryostat. Since below 2 K the temperature at the bolometer stage can go down lower than it can at the sample stage, the copper plate is screwed onto the cold plate of the bolometer stage. Four brass screws are used to mount the copper plate to the ^3He stage, by which the thermal conductivity between the copper plate and the cold plate can be improved. The illustrations of the measurements of $R_{MN,OP}$ and $R_{NO,PM}$ are shown in Fig. 5.5a and Fig. 5.5b respectively,

Figure 5.5a: $R_{MN,OP}$ Figure 5.5b: $R_{NO,PM}$

For fig. 5.5a firstly the applied current flows from the contact W_M to W_N and the corresponding potential difference between the contact W_O and W_P is measured so $R_{MN,OP}$ can be calculated once. Then the applied current flows from the contact W_N to W_M and again the potential difference between the other two contacts is measured so $R_{MN,OP}$ can be calculated a second time. An average value of the two calculations is used for $R_{MN,OP}$. For fig. 5.5b by using a programmable switching instrument the applied current can flow between the contact W_N and W_O and the corresponding potential difference between the contact W_P and W_M is measured. $R_{NO,PM}$ is calculated by the same method. Then $R_{MN,OP}$ and $R_{NO,PM}$ are used by the algorithm discussed in Section 5.1.3 to numerically calculate the f factor of Eq. 5.34 and thereafter the resistivity ρ by Eq. 5.33. The temperature is read by a temperature sensor at the sample stage above 6 K and by the other temperature sensor at the bolometer stage below 6 K. The communications between the instruments and the computer are through General Purpose Interface Buses (GPIB), which are designed by National Instruments [49]. The data points are recorded by using MPMS MultiVu Software, which is designed by Quantum Design [50].

For annealing, some samples were wrapped in tantalum foil and then put in a quartz tube. The inner wall of the quartz tube was covered by zirconium foil. The quartz tube was vacuumed to 4.4×10^{-7} Torr. The samples were annealed at 1000 °C for about three weeks. The warming rate and the cooling rate were not set up. [34,35]

The sample designated as Sample1 is unannealed and was measured once before cleaving to Sample1-1 and Sample1-2. It was attached to the copper plate by double-sided tape for the measurement.

Sample1-1 was measured three times after annealing. For the first measurement it was mounted on the copper plate by double-sided tape and measured about seven weeks after the annealing. For the second measurement it was attached by VGE-7031 and measured about fourteen weeks after the annealing. For the third measurement it was mounted on the copper plate by five-minute epoxy and measured about twenty six weeks after the annealing.

Sample1-2 was unannealed and attached to the copper plate by five-minute epoxy for the measurement.

Sample2 was also unannealed and mounted on the copper plate by double-sided tape.

Sample3-1 and Sample3-2 were split from one unannealed sample. Sample3-1 was measured twice after the annealing. For the first measurement it was attached to the copper plate by double-sided tape and measured about six weeks after the annealing. For the second measurement it was mounted on the copper plate by five-minute epoxy and measured about thirty two weeks after the annealing.

Sample3-2 was also measured twice. For the first measurement it was unannealed and attached to the copper plate by double-sided tape. For the second measurement it was mounted on the copper plate by five-minute epoxy and measured about forty three weeks after the annealing.

Annealed Sample3-2 (left) and unannealed Sample1-2 mounted by five-minute epoxy (right) are shown in Fig. 5.6.

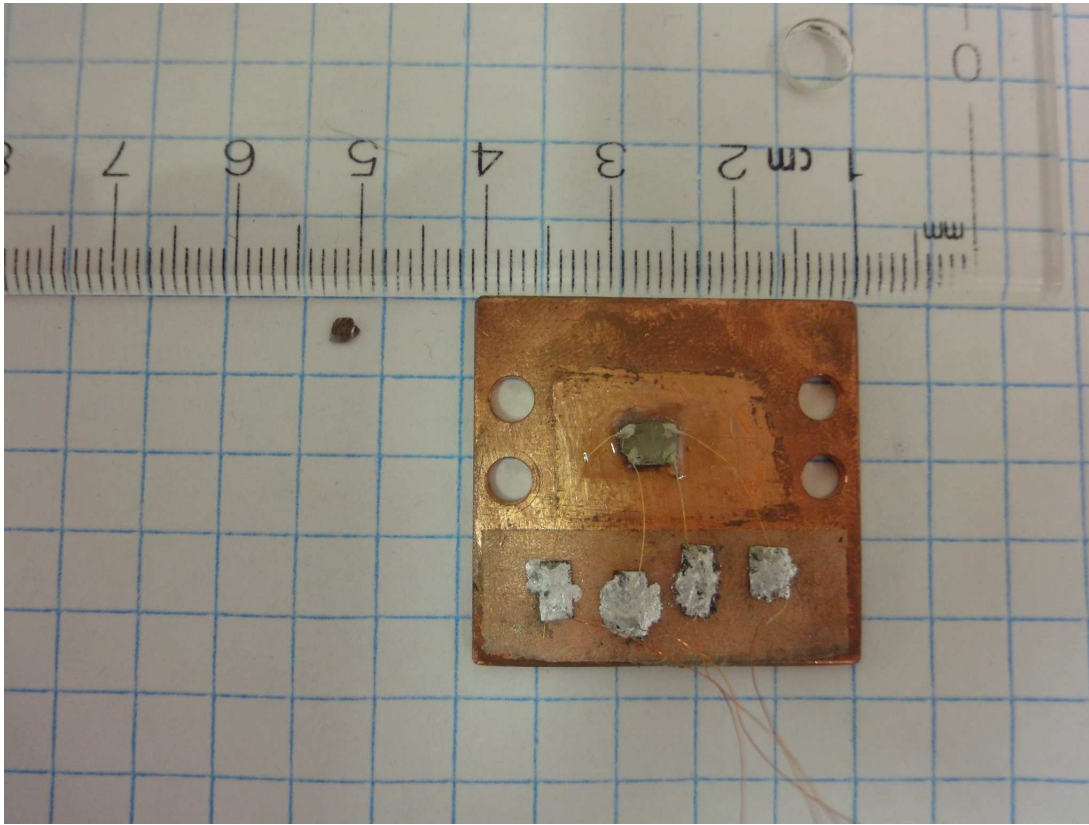


Figure 5.6: Annealed Sample3-2 (left) and unannealed Sample1-2 mounted by five-minute epoxy (right)

Sample1-1, Sample2 and Sample3-1 melted unexpectedly during the second round of annealing. Samples 1 and 2 were provided by Prof. Razavi, and were used in the study reported in reference [3]. Sample 3 was provided by Prof. Luke at McMaster. All three samples were grown by the Czochralski

Process. Samples 1 and 2 were single crystal and were spark cut perpendicular to the c -axis, which was verified by X-ray measurements. [3] For Sample1, Sample1-1, Sample1-2 and Sample2 the four contacts were on the cross section, which is supposed to be the ab plane.

5.3 Experimental Results

The samples were measured from about 0.5 K to room temperature. For nine of the ten measurements R_1 and R_2 (In the algorithm for calculating the resistivity $R_{MN,OP}$ and $R_{NO,PM}$ are written as R_1 and R_2 respectively.) appear to be along the a -axis. For annealed Sample1-1 mounted by five-minute epoxy one of the two resistances is along the a -axis while the other looks as if it is along the c -axis. This is likely because the four contacts were not at the same level. All experimental data below the Hidden Order temperature were fitted by,

$$\rho(T) = \rho_0 + BT^C + D \exp(-\Delta/T), \quad (5.35)$$

where ρ_0 is the residual resistivity at absolute zero, B , C and D are constants and Δ is the energy gap. [2] The values of these parameters are summarized in Table 5.1a and Table 5.1b.

All of the measurements for Sample1, Sample1-1 and Sample1-2 are plotted in Fig. 5.7a.

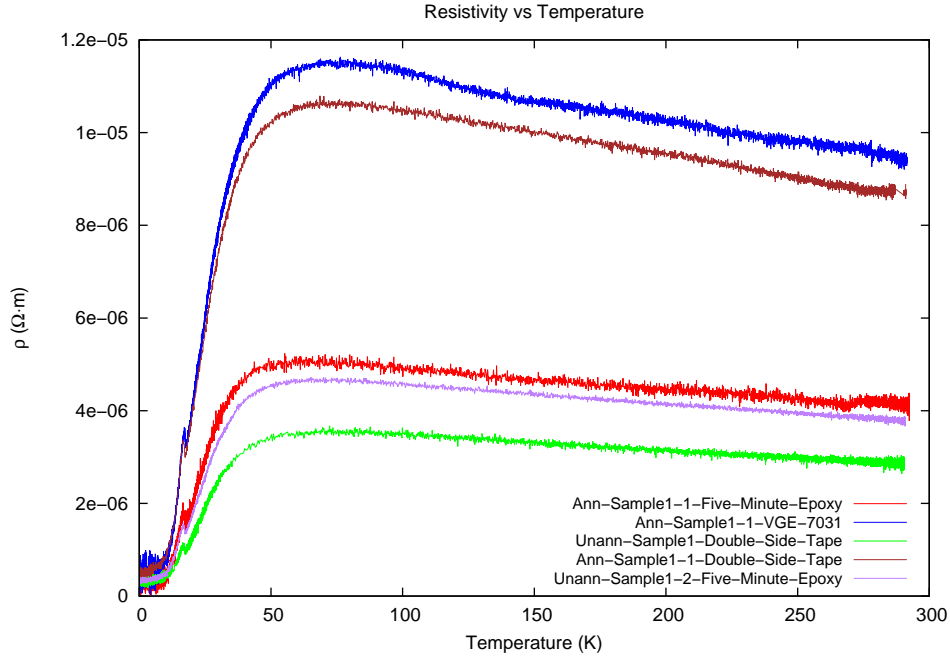


Figure 5.7a: Resistivity vs Temperature for Sample1, Sample1-1 and Sample1-2

For all of the measurements the resistivity slowly goes up as the temperature decreases from room temperature to the coherence temperature T_{co} . Then the resistivity drops drastically below T_{co} . At T_{HO} a λ shaped cusp appears. Below about 5 K the resistivity decreases slowly with decreasing temperature and no clear superconducting transition shows down to about 0.5 K. The resistivity after annealing appears to be increased. Fåk *et al.* had a similar surprising result [34]. T_{co} was about 75 K for annealed Sample1-1 mounted by double-sided tape or VGE-7031. T_{co} was about 50 K for unannealed Sample1 mounted by double-sided tape, annealed Sample1-1 attached by five-minute epoxy and unannealed Sample1-2 mounted by five-minute epoxy. For annealed Sample1-1 attached by five-minute epoxy R_1 appears to be along the a-axis while R_2 appears to be along the c-axis. At room temperature R_1 is about five times that of R_2 . At T_{co} R_1 is about seven times that of R_2 . Otherwise we expect that its resistivity would have approached those for it mounted by double-sided tape and by VGE-7031. The plots below 22.5 K are shown in Fig. 5.7b.

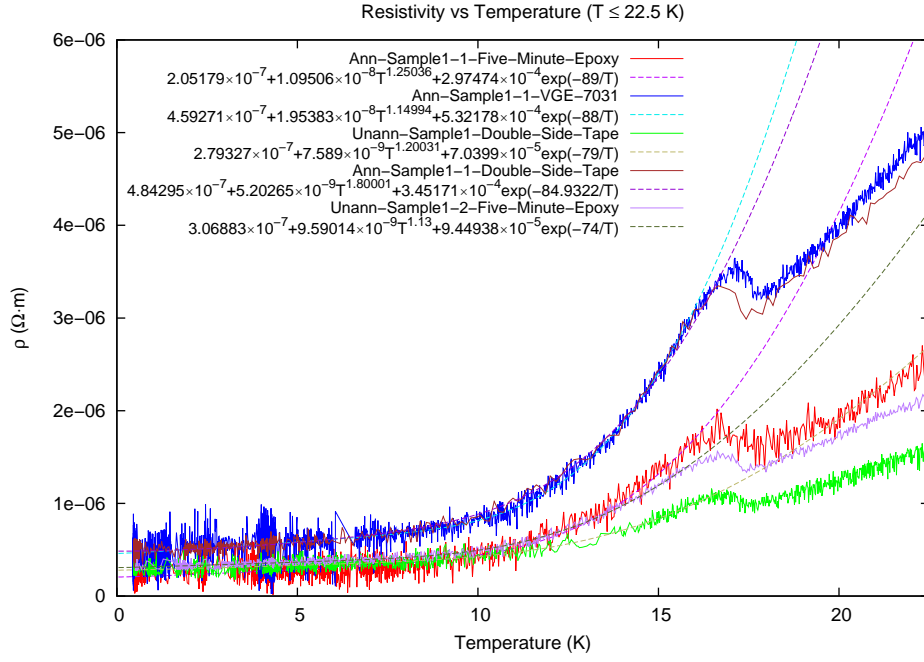


Figure 5.7b: Resistivity vs Temperature $T \leq 22.5K$ for Sample1, Sample1-1 and Sample1-2

The dashed lines are the fitting curves. Fig. 5.7c shows that annealed Sample1-1 mounted using five-minute epoxy had evidence of a SC transition below $0.6 K$.

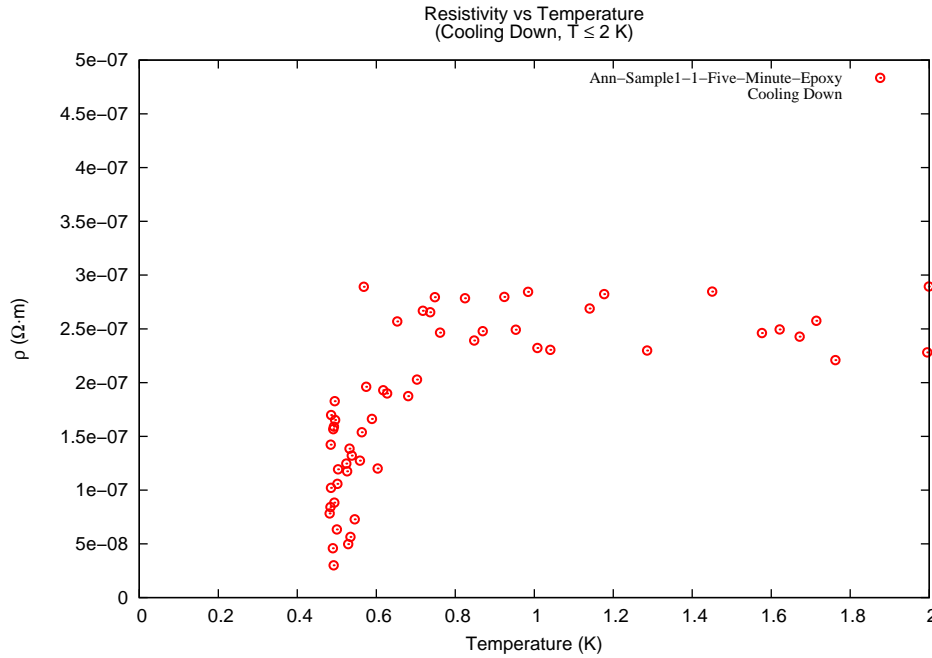


Figure 5.7c: Resistivity vs Temperature $T \leq 2K$ during cooling down for annealed Sample1-1 mounted using five-minute epoxy

The superconducting transition was observed when the applied current was switched from $3 mA$

to 1 *mA* followed by 0.5 *mA* but smaller current increased the noise level. Annealed Sample1-1 is approximately a rectangle. From Eq. 5.36a,

$$P = I^2 R, \quad (5.36a)$$

where P is the dissipated power, I is the applied current and R is the resistance and Eq. 5.36b,

$$R = \rho \frac{l}{S}, \quad (5.36b)$$

where ρ is the resistivity, l is the length of sample and S is the cross-section area, the dissipated power of annealed Sample1-1 mounted using five-minute epoxy was about 4.58×10^{-11} *Watt* at about 0.5 *K*. (The dimensions of annealed Sample1-1 were 5 *mm* \times 3.5 *mm* \times 0.87 *mm* at room temperature. The average resistivity was about $1.12 \times 10^{-7} \Omega \cdot m$ at about 0.5 *K*. The applied current was 0.5 *mA*.) However the resistance of the interface between the contact and the sample surface can be from several ohms to above ten ohms at room temperature. This likely generates much more heat than the sample itself does even at low temperature (Increasing the dissipated power by a few orders).

The resistivity did not go down to zero because the R_1 and R_2 were unwisely forced to be absolute values. Otherwise in the superconducting state the measured resistivity oscillates around zero according to Eq. 5.33.

The plot for unannealed Sample2 is shown in Fig. 5.8a.

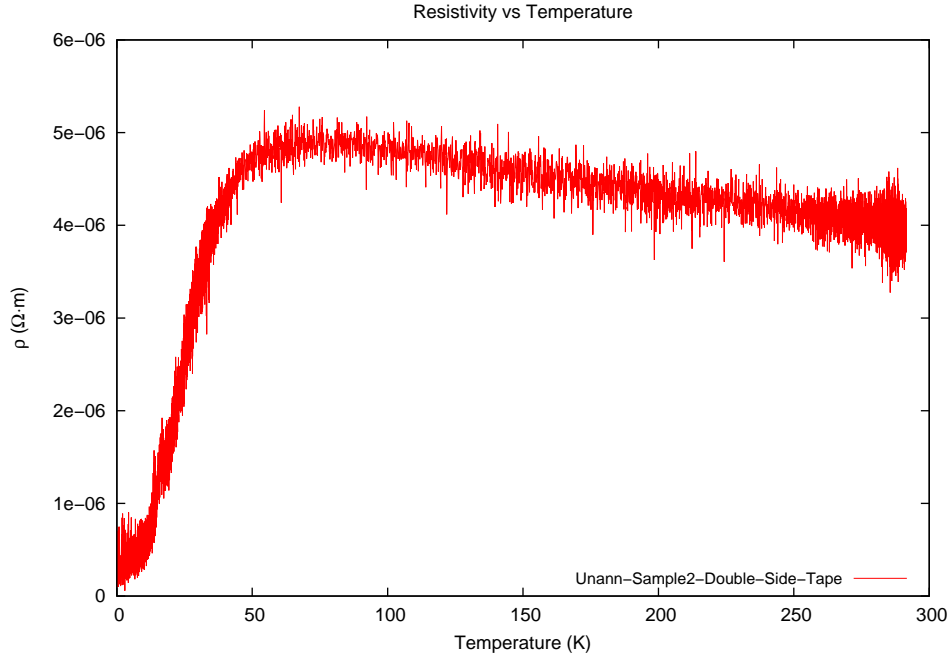
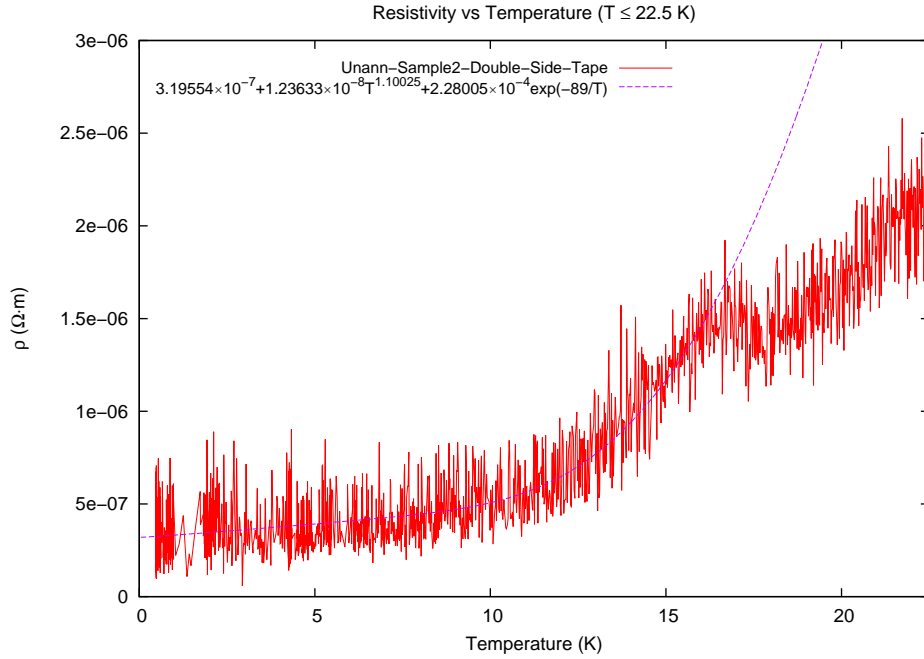


Figure 5.8a: Resistivity vs Temperature for Sample2

T_{co} is about 62.5 K. No SC transition shows down to about 0.5 K. The plot below 22.5 K is shown in Fig. 5.8b.

Figure 5.8b: Resistivity vs Temperature $T \leq 22.5K$ for Sample2

The dashed line is the fitting curve. The data have relatively larger noise for Sample2. The noise level along the resistance R_1 is much larger than it is along R_2 . In an excellent paper Vandamme

explained all kinds of noise sources in electronic measurements [51]. Two factors may cause the large noise along R_1 in Sample2. One factor is that the defects along R_1 are more prevalent than along R_2 . Vandamme showed that annealing reduced the noise. The other factor is that the contact resistances along R_1 are much greater than those along R_2 .

All measurements for Sample3-1 and Sample3-2 are shown in Fig. 5.9a.

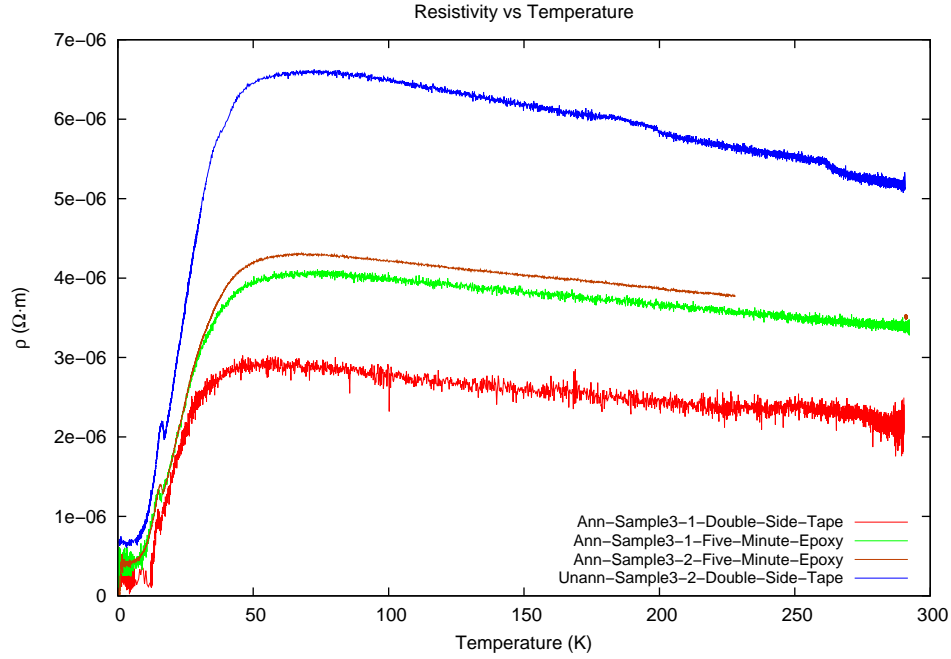


Figure 5.9a: Resistivity vs Temperature for Sample3-1 and Sample3-2

For these samples, the resistivity after annealing appears to be decreased. This may be because the crystal defects in Sample3-1 and Sample3-2 are at a much higher concentration level than those for Sample1-1, which can be seen from their RRR. The annealing appears to be not quite as effective for Sample3-1 and Sample3-2 as it was for Sample1-1 because RRR for Sample3-1 and Sample3-2 has almost no enhancement after annealing while RRR for Sample1-1 has a notable enhancement after annealing. T_{co} is about 50 K for annealed Sample3-1 attached by double-sided tape. T_{co} was about 62.5 K for unannealed Sample3-2 attached by double-sided tape, annealed Sample3-1 mounted using five-minute epoxy and annealed Sample3-2 attached by five-minute epoxy. Annealed Sample3-2 mounted with five-minute epoxy exhibits a SC transition as shown in Fig. 5.9c. The starting point and ending point of the SC transition width are at about 1.36 K and 0.85 K respectively. For this measurement when the temperature rose to 228.08 K, one contact split off from the sample. The

data at room temperature were measured before cooling down. The plots below 22.5 K are shown in Fig. 5.9b.

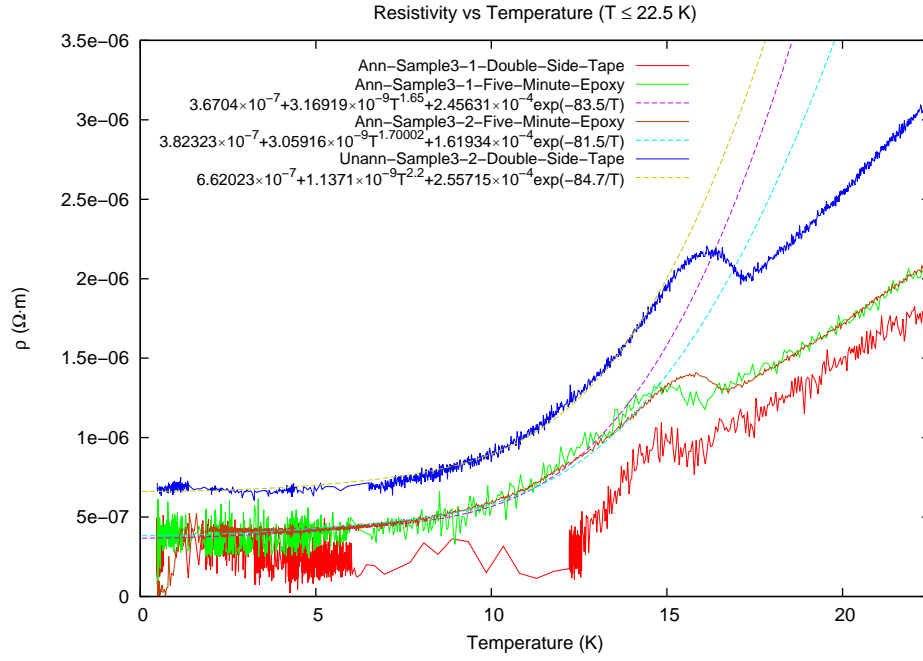


Figure 5.9b: Resistivity vs Temperature $T \leq 22.5K$ for Sample3-1 and Sample3-2

The dashed lines are the fitting curves. For annealed Sample3-1 attached with double-sided tape the refrigerator switch at the sample stage was accidentally not tightened. When the temperature rose above 6 K , the temperature sensor was switched from the one at the bolometer stage to the one at the sample stage and it was measured as about 12 K . The misalignment of data for this part makes it invalid for fitting. The plot for annealed Sample3-2 attached with five-minute epoxy below 22.5 K is shown in Fig. 5.9c.

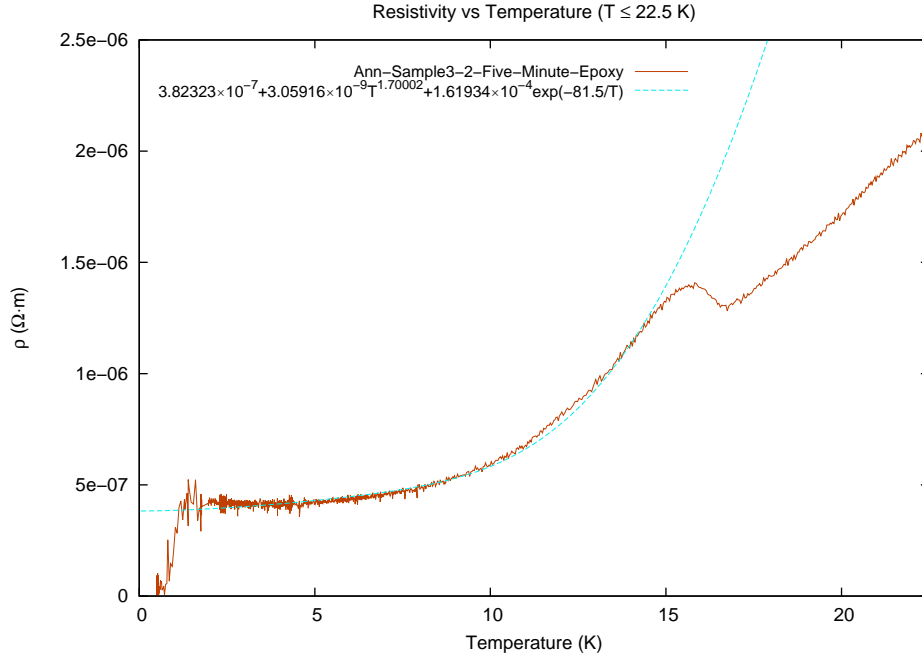


Figure 5.9c: Resistivity vs Temperature $T \leq 22.5 K$ for annealed Sample3-2

The dashed line is the fitting curve. Though RRR does not increase much after annealing for Sample3-2, the annealing may effectively remove the defects which can destroy heavy fermion superconductivity. The mounting medium, five-minute epoxy, has better thermal conductivity. The size of Sample3-2 is also much smaller than that of other samples so the interface between the contact and the sample surface needs to be small in order that four contacts can be placed on the sample. These factors effectively reduce the heat generated due to the applied current during the measurements. The Residual Resistivity Ratio (RRR) defined by Matsuda *et al.* is the resistivity at 300 K divided by that at 2 K [2]. For all of our measurements the resistivity below 5 K in the normal state decreases slowly with decreasing temperature so the RRR is the average resistivity at about room temperature divided by that at about the lowest temperature in the normal state around 0.5 K. For annealed Sample3-2 it is divided by the average resistivity at about 2 K since the data have some noise near the onset of the SC transition. The plots of the exponent C in Eq. 5.35 versus RRR compared with those obtained by Matsuda *et al.* are shown in Fig. 5.10.

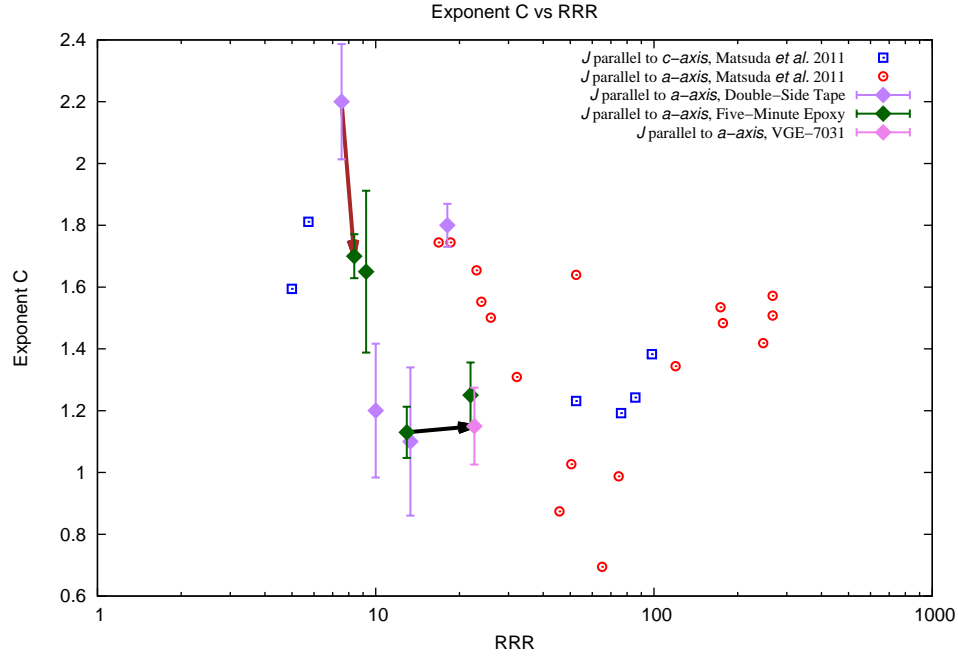


Figure 5.10: Exponent C vs RRR

Our data along with those of Matsuda *et al.* seem to show that for the lowest values of RRR C approaches 2, which shows Fermi liquid behaviour. For intermediate RRR C approaches 1. For high RRR the measurements done by Matsuda *et al.* show that C values approach 1.5. [2] The brown arrow shows the effect of annealing on Sample3-2. The black arrow shows the effect of annealing on Sample1.

The Hidden Order temperature is defined by the local minimum temperature at HO. The plots of T_{HO} vs RRR compared with those obtained by Matsuda *et al.* are shown in Fig. 5.11.

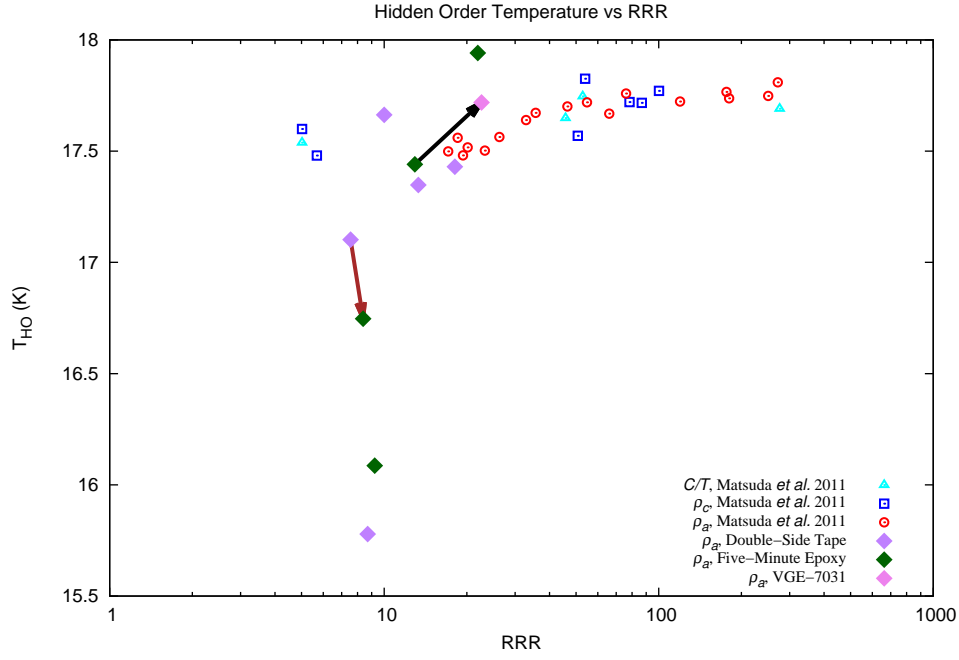


Figure 5.11: Hidden Order Temperature vs RRR

For low RRR like our samples T_{HO} has a notable drop as RRR decreases. For high RRR the measurements carried out by Matsuda *et al.* show that T_{HO} saturates to some higher temperature as RRR increases. The brown arrow shows the effect on T_{HO} of annealing on Sample3-2. The black arrow shows the effect on T_{HO} of annealing on Sample1.

The temperature transition width at HO ΔT_{HO} is defined as the temperature at the local minimum subtracted by that at the local maximum. The plots of ΔT_{HO} vs RRR compared with those obtained by Matsuda *et al.* are shown in Fig. 5.12.

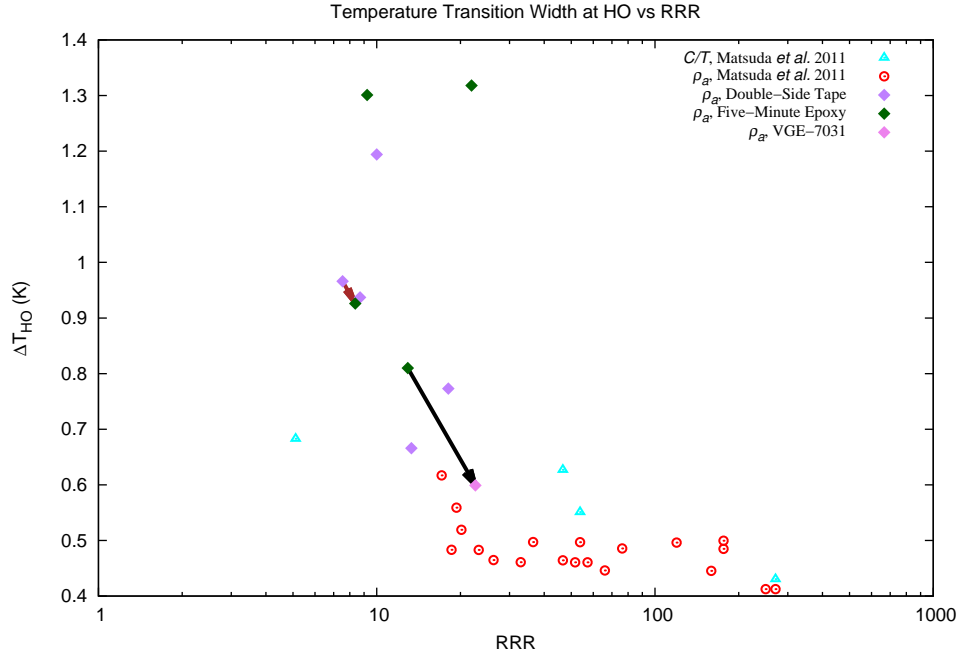


Figure 5.12: Temperature Transition Width at HO vs RRR

For low RRR like our samples ΔT_{HO} has a notable rise as RRR decreases. For high RRR the measurements carried out by Matsuda *et al.* show that ΔT_{HO} saturates to some lower value as RRR increases. The brown arrow shows the effect of annealing on ΔT_{HO} for Sample3-2. The black arrow shows the effect of annealing on ΔT_{HO} for Sample1.

The values of RRR, fitting parameters, local maximum and local minimum at HO and ΔT_{HO} are summarized in Table 5.1a and Table 5.1b.

Table 5.1a: RRR, fitting parameters, local maximum and local minimum at HO and ΔT_{HO}

<i>J</i> parallel to a-axis, Resistivity Fitting to $\rho(T) = \rho_0 + BT^C + D \exp(-\Delta/T)$					
URu ₂ Si ₂	Ann-Sample1-1-Five-Minute-Epoxy ^a	Ann-Sample1-1-VGE-7031	Unann-Sample1-Double-Side-Tape	Ann-Sample1-1-Double-Side-Tape	Unann-Sample1-2-Five-Minute-Epoxy
RRR ^b	21.92	22.62	10	18.09	12.928
ρ_0 ($\Omega \cdot m$)	$(2.05 \pm 0.06) \times 10^{-7}$	$(4.59 \pm 0.10) \times 10^{-7}$	$(2.79 \pm 0.07) \times 10^{-7}$	$(4.84 \pm 0.02) \times 10^{-7}$	$(3.07 \pm 0.03) \times 10^{-7}$
B ($\Omega \cdot m \cdot K^{-C}$)	$(1.1 \pm 0.3) \times 10^{-8}$	$(2.0 \pm 0.5) \times 10^{-8}$	$(8 \pm 4) \times 10^{-9}$	$(5.2 \pm 0.7) \times 10^{-9}$	$(10 \pm 2) \times 10^{-9}$
C	1.3 ± 0.1	1.1 ± 0.1	1.2 ± 0.2	1.80 ± 0.07	1.13 ± 0.08
D ($\Omega \cdot m$)	$(3.0 \pm 0.7) \times 10^{-4}$	$(5.3 \pm 0.8) \times 10^{-4}$	$(7 \pm 2) \times 10^{-5}$	$(3.5 \pm 0.5) \times 10^{-4}$	$(9.4 \pm 0.8) \times 10^{-5}$
Δ (K)	89 ± 4	88 ± 3	79 ± 5	85 ± 3	74 ± 1
Local Maximum at HO	T=16.623 K , $\rho = 2.019445 \times 10^{-6} \Omega \cdot m$	T=17.12 K , $\rho = 3.647411 \times 10^{-6} \Omega \cdot m$	T=16.469 K , $\rho = 1.15906 \times 10^{-6} \Omega \cdot m$	T=16.657 K , $\rho = 3.348107 \times 10^{-6} \Omega \cdot m$	T=16.631 K , $\rho = 1.561795 \times 10^{-6} \Omega \cdot m$
Local Minimum at HO	T=17.941 K , $\rho = 1.369568 \times 10^{-6} \Omega \cdot m$	T=17.719 K , $\rho = 3.191629 \times 10^{-6} \Omega \cdot m$	T=17.663 K , $\rho = 8.948714 \times 10^{-7} \Omega \cdot m$	T=17.43 K , $\rho = 2.987854 \times 10^{-6} \Omega \cdot m$	T=17.441 K , $\rho = 1.335378 \times 10^{-6} \Omega \cdot m$
Hidden Order Transition Width (ΔT_{HO})	1.318 K	0.599 K	1.194 K	0.773 K	0.81 K

^a $R_1 \parallel$ a-axis & $R_2 \parallel$ c-axis.^b Explained in Sec. 5.3

Table 5.1b: RRR, fitting parameters, local maximum and local minimum at HO and ΔT_{HO}
CONT.

<i>J</i> parallel to a-axis, Resistivity Fitting to $\rho(T) = \rho_0 + BT^C + D \exp(-\Delta/T)$					
URu ₂ Si ₂	Unann-Sample2- Double-Side-Tape	Ann-Sample3-1- Double-Side-Tape	Ann-Sample3-1-Five- Minute-Epoxy	Ann-Sample3-2-Five- Minute-Epoxy	Unann-Sample3-2- Double-Side-Tape
RRR	13.32	8.71	9.24	8.376	7.54
$\rho_0 (\Omega \cdot m)$	$(3.20 \pm 0.09) \times 10^{-7}$	N/A	$(3.67 \pm 0.04) \times 10^{-7}$	$(3.82 \pm 0.02) \times 10^{-7}$	$(6.62 \pm 0.02) \times 10^{-7}$
$B (\Omega \cdot m \cdot K^{-C})$	$(1.2 \pm 0.6) \times 10^{-8}$	N/A	$(3 \pm 2) \times 10^{-9}$	$(3.1 \pm 0.5) \times 10^{-9}$	$(1.1 \pm 0.4) \times 10^{-9}$
C	1.1 ± 0.2	N/A	1.6 ± 0.3	1.70 ± 0.07	2.2 ± 0.2
$D (\Omega \cdot m)$	$(2.3 \pm 0.8) \times 10^{-4}$	N/A	$(2 \pm 2) \times 10^{-4}$	$(1.6 \pm 0.1) \times 10^{-4}$	$(2.6 \pm 0.4) \times 10^{-4}$
$\Delta (K)$	89 ± 7	N/A	84 ± 10	82 ± 1	85 ± 3
Local Maximum at HO	T=16.682 K, $\rho =$ $1.923534 \times 10^{-6} \Omega \cdot m$	T=14.842 K, $\rho =$ $1.094138 \times 10^{-6} \Omega \cdot m$	T=14.785 K, $\rho =$ $1.341572 \times 10^{-6} \Omega \cdot m$	T=15.821 K, $\rho =$ $1.408347 \times 10^{-6} \Omega \cdot m$	T=16.136 K, $\rho =$ $2.202796 \times 10^{-6} \Omega \cdot m$
Local Minimum at HO	T=17.348 K, $\rho =$ $1.052761 \times 10^{-6} \Omega \cdot m$	T=15.779 K, $\rho =$ $7.681365 \times 10^{-7} \Omega \cdot m$	T=16.086 K, $\rho =$ $1.177532 \times 10^{-6} \Omega \cdot m$	T=16.747 K, $\rho =$ $1.281394 \times 10^{-6} \Omega \cdot m$	T=17.102 K, $\rho =$ $1.963180 \times 10^{-6} \Omega \cdot m$
Hidden Order Transition Width (ΔT_{HO})	0.666 K	0.937 K	1.301 K	0.926 K	0.966 K

5.4 Some Other Models of Resistivity

For conduction electron-phonon interaction the resistivity is given by the Bloch-Grüneisen formula.

Its high temperature solution is,

$$\rho = \frac{A}{4} \left(\frac{T}{\theta_D} \right) \text{ for } T \geq \theta_D, \quad (5.37a)$$

and its low temperature solution is,

$$\rho = 124.4A \left(\frac{T}{\theta_D} \right)^5 \text{ for } T \ll \theta_D, \quad (5.37b)$$

where A is a constant and θ_D is Debye temperature. [52, p. 58-59]

For conduction electron-magnetic ion interaction in dilute solid solution the resistivity is given by the Kondo effect,

$$\rho = c\rho_0 - c\rho_1 \ln T, \quad (5.38)$$

where c is the concentration of magnetic ions, ρ_0 is the residual resistivity, ρ_1 is a constant and T is temperature. [40, p. 639]

If different scatterings of conduction electron exist simultaneously, according to Matthiessen's Rule the resultant resistivity will be a simple summation of resistivities due to each scattering process. However this rule does not consider the interactions among different scattering mechanisms so some experimental observations deviate from this rule. [52, p. 43-44] [53, p. 9-10]

Chapter 6

DC Magnetization Measurement at SC Transition

6.1 Meissner Effect

Besides zero resistivity a superconductor exhibits another fundamental property, the Meissner effect. The Meissner effect distinguishes a superconductor from an ideal conductor. W. Meissner and R. Ochsenfeld discovered the Meissner effect in 1933 [23, p. 9]. The response to an applied magnetic field for a superconductor and an ideal conductor is shown in Fig. 6.1 [54, Sec. 2.3].

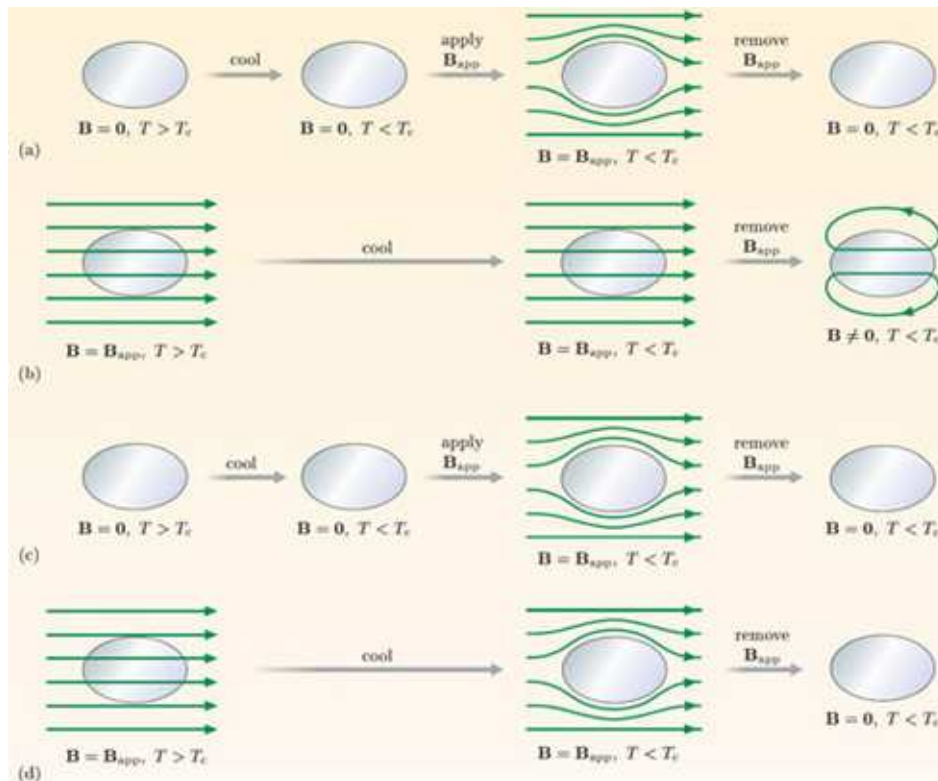


Figure 6.1: A comparison of response to applied magnetic field between ideal conductor and superconductor [54, Sec. 2.3]

In Fig. 6.1 (a) [54, Sec. 2.3] an ideal conductor is initially cooled under zero magnetic field until below the critical temperature, when its resistivity becomes zero. Then an applied magnetic field is turned on and the screening current produced on the surface repels the applied magnetic flux. So the magnetic flux cannot penetrate inside the ideal conductor. After the field is turned off, the magnetic flux is zero inside the ideal conductor. [54]

In Fig. 6.1 (b) [54, Sec. 2.3] the ideal conductor is cooled under an applied field from the normal state to a temperature below T_c . At temperatures both above and below T_c the magnetic flux can penetrate inside the ideal conductor. After the applied field is turned off below T_c , the magnetic flux remains inside the ideal conductor. [54]

In Fig. 6.1 (c) [54, Sec. 2.3] a superconductor is initially cooled under zero magnetic field until the temperature is below T_c . Then an applied field is turned on and the screening current produced on the surface repels the applied magnetic flux. The magnetic flux inside the superconductor is zero and it remains zero after the applied field is turned off.

In Fig. 6.1 (d) [54, Sec. 2.3] the superconductor is cooled under a non-zero magnetic field. In its normal state the magnetic flux can penetrate inside the superconductor but below T_c in its superconducting state the magnetic flux is repelled by the screening current on the superconductor surface. Below T_c after the applied field is turned off, no magnetic flux is inside the superconductor. The field inside the superconductor is zero below T_c no matter whether the applied field is zero or not.

Superconductivity implies perfect diamagnetism. The relative permeability μ_r is zero. The applied field H is related to the induced field B through,

$$\begin{aligned} B &= \mu_0(H + M) \\ &= \mu_0\left(1 + \frac{M}{H}\right)H \\ &= \mu_0(1 + \chi)H, \end{aligned} \tag{6.1}$$

where μ_0 is the permeability in free space, M is the volume magnetization and χ is the susceptibility.

The induced field B is zero so,

$$\mu_r = 1 + \chi = 0, \quad (6.2a)$$

and

$$\chi = -1. \quad (6.2b)$$

The susceptibility for perfect diamagnetism like superconductivity is -1.

In 1935 the brothers Fritz London and Heinz London derived a set of two equations, which give mathematical descriptions of the two fundamental properties of superconductivity. These are the first London equation and the second London equation [54, Sec. 3.3] [55, p. 5]. From a Drude-Lorentz model for electrons in a metal, Newton's second law is [55, p. 5],

$$m^* \left(\frac{dv}{dt} + \Gamma v \right) = eE, \quad (6.3)$$

where m^* is the effective mass of electron, v is the drift velocity, Γ is the scattering rate, e is the electron charge and E is the applied electric field. Since for either an ideal conductor or a superconductor the relaxation time τ goes to infinity, the scattering rate

$$\Gamma = \frac{1}{\tau} = 0. \quad (6.4)$$

The current density is given by,

$$J = nev, \quad (6.5)$$

where n is the conduction electron density. So we have

$$\frac{\partial J}{\partial t} = ne \frac{dv}{dt}. \quad (6.6)$$

Combining Eq. 6.3, Eq. 6.4 and Eq. 6.6 we have,

$$\frac{\partial J}{\partial t} = \frac{ne^2 E}{m^*}. \quad (6.7)$$

Eq. 6.7 is the first London equation. It states that a constant current can flow in either an ideal

conductor or a superconductor without applied electric field. The fourth equation of Maxwell's equations in matter is,

$$\nabla \times H = J_f + \frac{\partial(P + \epsilon_0 E)}{\partial t} = J_f + \frac{\partial D}{\partial t}, \quad (6.8)$$

where J_f is the free electron current density, P is the volume polarization, ϵ_0 is the permittivity in free space, E is the applied electric field and D is the electric flux density. Assuming the electric flux density is independent of time then we have,

$$\nabla \times H = J_f. \quad (6.9)$$

Taking the time derivative on both sides of Eq. 6.9 we have,

$$\nabla \times \frac{\partial H}{\partial t} = \frac{\partial J_f}{\partial t}. \quad (6.10)$$

Substituting Eq.6.10 into Eq. 6.7 we have,

$$\nabla \times \frac{\partial H}{\partial t} = \frac{ne^2 E}{m^*}. \quad (6.11)$$

Taking the curl of both sides of Eq. 6.11 we have,

$$\nabla \times \nabla \times \frac{\partial H}{\partial t} = \frac{ne^2}{m^*} \nabla \times E. \quad (6.12)$$

Substituting the third equation of Maxwell's equations in matter

$$\nabla \times E = -\mu_0 \frac{\partial H}{\partial t}, \quad (6.13)$$

into Eq. 6.12 we have,

$$\nabla \times \nabla \times \frac{\partial H}{\partial t} + \frac{ne^2 \mu_0}{m^*} \frac{\partial H}{\partial t} = 0. \quad (6.14)$$

By the vector identity,

$$\nabla \times \nabla \times H = \nabla(\nabla \cdot H) - \nabla^2 H, \quad (6.15)$$

and the second Maxwell's equation,

$$\nabla \cdot H = 0, \quad (6.16)$$

we have,

$$\nabla \times \nabla \times H = -\nabla^2 H. \quad (6.17)$$

Substituting Eq. 6.17 into Eq. 6.14 we obtain,

$$\frac{\partial(-\nabla^2 H)}{\partial t} + \frac{ne^2\mu_0}{m^*} \frac{\partial H}{\partial t} = 0. \quad (6.18)$$

Rearranging we find,

$$\nabla^2 \frac{\partial H}{\partial t} - \frac{ne^2\mu_0}{m^*} \frac{\partial H}{\partial t} = 0. \quad (6.19)$$

For an applied field H perpendicular to the surface of an ideal conductor, the only solution to Eq. 6.19 is $\partial H/\partial t = 0$ but this doesn't mean $H = 0$. For H parallel to the conductor's surface, e.g. in z direction as shown in Fig. 6.2 we have,

$$\frac{\partial^2}{\partial x^2} \left(\frac{\partial H}{\partial t} \right) - \frac{ne^2\mu_0}{m^*} \frac{\partial H}{\partial t} = 0. \quad (6.20)$$

Replacing $ne^2\mu_0/m^*$ by $1/\lambda^2$ we have,

$$\frac{\partial^2}{\partial x^2} \left(\frac{\partial H}{\partial t} \right) - \frac{1}{\lambda^2} \frac{\partial H}{\partial t} = 0. \quad (6.21)$$

Eq. 6.21 is a second order linear and homogeneous differential equation with respect to x and its characteristic equation is,

$$1 \cdot C^2 + 0 \cdot C - \frac{1}{\lambda^2} = 0, \quad (6.22)$$

which is a quadratic equation. The coefficients of Eq. 6.22 satisfy,

$$0^2 - 4 \cdot 1 \cdot \left(-\frac{1}{\lambda^2} \right) > 0, \quad (6.23)$$

and the two roots of Eq. 6.22 are $\pm \frac{1}{\lambda}$ so the general solution to Eq. 6.21 is,

$$\frac{\partial H}{\partial t} \hat{z} = A \exp\left(\frac{-|x|}{\lambda}\right) + B \exp\left(\frac{|x|}{\lambda}\right), \quad (6.24)$$

where A and B are constants. B has to be zero to have physical meaning. By applying a boundary condition at $x = 0$ we have,

$$\frac{\partial H_0}{\partial t} \hat{z} = A, \quad (6.25)$$

so that,

$$\frac{\partial H}{\partial t} \hat{z} = \frac{\partial H_0}{\partial t} \hat{z} \exp\left(\frac{-|x|}{\lambda}\right), \quad (6.26)$$

and $\partial H \hat{z} / \partial t$ decreases exponentially inside an ideal conductor. Again it doesn't mean $H \hat{z}$ has the same behaviour. To conform with the experimental observation for a superconductor, Eq. 6.19 has to be corrected to

$$\nabla^2 H - \frac{1}{\lambda_L^2} H = 0. \quad (6.27)$$

Thus for H perpendicular to a superconductor surface, H has to be zero inside the superconductor. For H parallel to a superconductor surface, we have a solution,

$$H \hat{z} = H_0 \hat{z} \exp\left(\frac{-|x|}{\lambda_L}\right), \quad (6.28)$$

so the applied field decreases exponentially inside a superconductor as shown in Fig. 6.2 [23, p. 31].

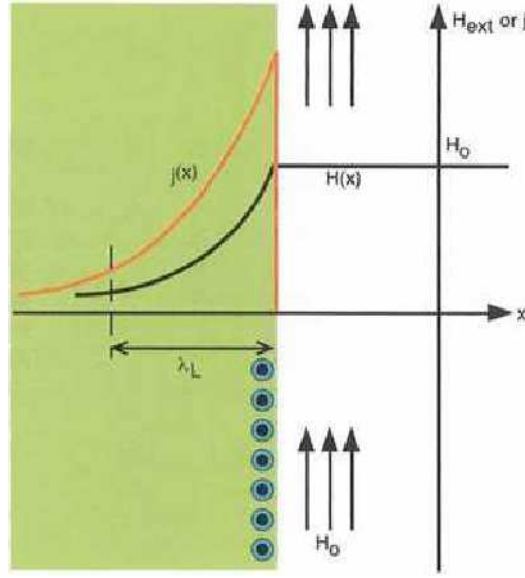


Figure 6.2: London penetration length in a superconductor [23, p. 31]

λ_L is the London penetration length, at which the applied field decreases to $\frac{1}{e}$ of the value at the boundary. λ_L is dependent on temperature.

6.2 Type-I superconductor and Type-II superconductor

The response to applied magnetic field for Type-I and Type-II superconductors has some differences. For a Type-I superconductor the applied magnetic field can be expelled up until a critical field H_c . At H_c it is in intermediate state, at which normal state and superconducting state coexist alternately inside the body. Above H_c it is in the normal state. [23, p. 37]

The response of a Type-II superconductor to the applied field has some differences. Below a lower critical field H_{c1} it is in the Meissner state. Between H_{c1} and an upper critical field H_{c2} it is in a vortex state. Above H_{c2} it is in the normal state. In the vortex state some magnetic flux penetrates inside the body with a super eddy current flowing around each of them. Each flux has a value of the flux quantum Φ_0 , where

$$\Phi_0 = \frac{hc}{2e} = 2.07 \times 10^{-7} \text{ Gauss/cm}^2. \quad [23, \text{ p. 44}] \quad [56, \text{ p. 12}] \quad (6.29)$$

These vortices form an equilateral-triangle array as shown in Fig. 6.3 [23, p. 39].

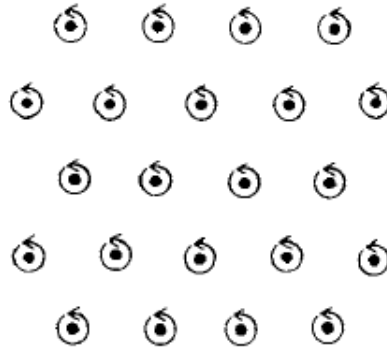


Figure 6.3: Equilateral-triangle array in the vortex state [23, p. 39]

As the applied field increases, the density of these vortices increases until the upper critical field is reached. Above H_{c2} the applied magnetic flux will penetrate the body completely so it is in the normal state. The relation between H_{c1} and H_{c2} is given by,

$$\frac{H_{c1}}{H_{c2}} = \frac{\ln \kappa}{2\kappa^2} \quad [56, \text{ p. 154}] \quad [57, \text{ p. 89}], \quad (6.30)$$

where κ is the Ginzburg-Landau parameter equal to $\lambda^*(T)/\xi^*(T)$, where $\lambda^*(T)$ is the effective London penetration length and $\xi^*(T)$ is the effective coherence length. The coherence length ξ is another characteristic length, within which the density of super electrons depends on the position from the surface into the body of a superconductor in a magnetic field. $\lambda^*(T)$ and $\xi^*(T)$ are temperature dependent while κ is approximately independent of temperature. For $\kappa < \frac{1}{\sqrt{2}}$ it is a Type-I superconductor and for $\kappa > \frac{1}{\sqrt{2}}$ it is a Type-II superconductor. [56, p. 161] H_{c1} , H_{c2} and κ given by Palstra *et al.* for URu_2Si_2 are $1.4mT$, $0.86T$ and 33 respectively at 0.657 K [8], which approximately satisfy Eq. 6.30.

Although the response to an applied field is different for Type-I and Type-II superconductors, the free energy released during the transition from the normal state to the Meissner state at zero field is $H_c^2/(8\pi)$ for both types if they have the same thermodynamic critical field H_c . For a Type-II superconductor the relation among H_{c1} , H_{c2} and H_c is given by,

$$H_{c1}H_{c2} = H_c^2 \ln \kappa \quad [56, \text{ p. 154}] \quad [58, \text{ p. 344}]. \quad (6.31)$$

Fig. 6.4 shows the magnetization for three superconductors, which have the same thermodynamic

critical field H_c [56, p. 161].

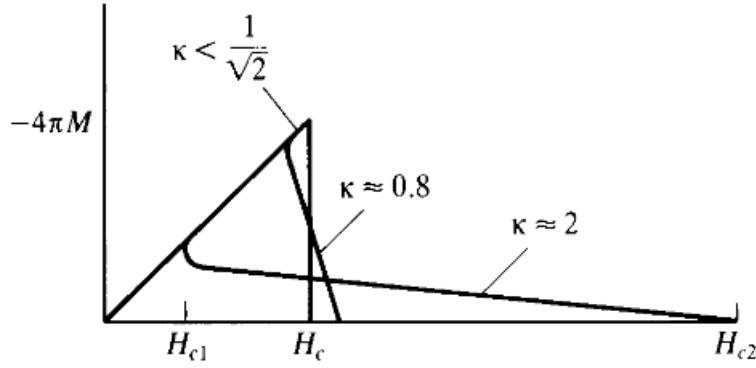


Figure 6.4: Magnetization curves for Type-I and Type-II superconductors [56, p. 161]

For $\kappa < \frac{1}{\sqrt{2}}$ it is a Type-I superconductor. The curves for $\kappa \approx 0.8$ and $\kappa \approx 2$ correspond to Type-II superconductors. The area under the magnetization curve is the same for all three superconductors, and is given by,

for a Type-I superconductor,

$$\int_0^{H_c} (-4\pi M) dH = \frac{H_c^2}{2}, \quad (6.32a)$$

and for a Type-II superconductor,

$$\int_0^{H_{c2}} (-4\pi M) dH = \frac{H_c^2}{2}. \quad (6.32b)$$

6.3 Josephson effect

For a superconductor sandwich, two superconductors separated by a thin insulator, the Cooper pairs can tunnel through the thin insulator. The theory is cited following the references [40, p. 289-p. 290] and [58, p. 460-p. 461].

The wave functions of the Cooper pairs for each superconductor are,

$$\psi_1 = n_{s1}^{\frac{1}{2}} e^{i\theta_1}, \quad (6.33a)$$

and

$$\psi_2 = n_{s2}^{\frac{1}{2}} e^{i\theta_2}. \quad (6.33b)$$

Applying the time dependent Schrödinger equation,

$$i\hbar \frac{\partial \psi}{\partial t} = \hat{H}\psi, \quad (6.34)$$

to the wavefunctions ψ_1 and ψ_2 we have,

$$i\hbar \frac{\partial \psi_1}{\partial t} = \hbar T \psi_2, \quad (6.35a)$$

and

$$i\hbar \frac{\partial \psi_2}{\partial t} = \hbar T \psi_1, \quad (6.35b)$$

where $\hbar T$ is the coupling operator due to the interaction among Cooper pairs through the sandwich.

Substituting Eq. 6.33a and Eq. 6.33b into Eq. 6.35a and Eq. 6.35b respectively we have,

$$i\hbar \left(\frac{1}{2} n_{s1}^{-\frac{1}{2}} \frac{\partial n_{s1}}{\partial t} e^{i\theta_1} + n_{s1}^{\frac{1}{2}} e^{i\theta_1} i \frac{\partial \theta_1}{\partial t} \right) = \hbar T n_{s2}^{\frac{1}{2}} e^{i\theta_2}, \quad (6.36a)$$

and

$$i\hbar \left(\frac{1}{2} n_{s2}^{-\frac{1}{2}} \frac{\partial n_{s2}}{\partial t} e^{i\theta_2} + n_{s2}^{\frac{1}{2}} e^{i\theta_2} i \frac{\partial \theta_2}{\partial t} \right) = \hbar T n_{s1}^{\frac{1}{2}} e^{i\theta_1}. \quad (6.36b)$$

The terms in the brackets on the left sides of Eq. 6.36a and 6.36b are from the product rule of differentiation. The complex conjugates of ψ_1 and ψ_2 are respectively,

$$\psi_1^* = n_{s1}^{\frac{1}{2}} e^{-i\theta_1}, \quad (6.37a)$$

$$\psi_2^* = n_{s2}^{\frac{1}{2}} e^{-i\theta_2}, \quad (6.37b)$$

and multiplying Eq. 6.36a by 6.37a and Eq. 6.36b by 6.37b, we have

$$i\hbar \left(\frac{1}{2} \frac{\partial n_{s1}}{\partial t} + n_{s1} i \frac{\partial \theta_1}{\partial t} \right) = \hbar T (n_{s1} n_{s2})^{\frac{1}{2}} e^{i(\theta_2 - \theta_1)}, \quad (6.38a)$$

$$i\hbar \left(\frac{1}{2} \frac{\partial n_{s2}}{\partial t} + n_{s2} i \frac{\partial \theta_2}{\partial t} \right) = \hbar T (n_{s1} n_{s2})^{\frac{1}{2}} e^{i(\theta_1 - \theta_2)}. \quad (6.38b)$$

Dividing both sides of Eq. 6.38a and 6.38b by $i\hbar$ and letting $\theta_2 - \theta_1 = \varphi$, we obtain

$$\frac{1}{2} \frac{\partial n_{s1}}{\partial t} + n_{s1} i \frac{\partial \theta_1}{\partial t} = -iT(n_{s1}n_{s2})^{\frac{1}{2}} e^{i\varphi}, \quad (6.39a)$$

$$\frac{1}{2} \frac{\partial n_{s2}}{\partial t} + n_{s2} i \frac{\partial \theta_2}{\partial t} = -iT(n_{s1}n_{s2})^{\frac{1}{2}} e^{-i\varphi}. \quad (6.39b)$$

The Euler formula gives,

$$e^{i\varphi} = \cos \varphi + i \sin \varphi, \quad (6.40a)$$

and

$$e^{-i\varphi} = \cos(-\varphi) + i \sin(-\varphi) = \cos \varphi - i \sin \varphi. \quad (6.40b)$$

Substituting Eq. 6.40a and 6.40b into Eq. 6.39a and Eq. 6.39b respectively gives,

$$\frac{1}{2} \frac{\partial n_{s1}}{\partial t} + n_{s1} i \frac{\partial \theta_1}{\partial t} = -iT(n_{s1}n_{s2})^{\frac{1}{2}} (\cos \varphi + i \sin \varphi), \quad (6.41a)$$

and

$$\frac{1}{2} \frac{\partial n_{s2}}{\partial t} + n_{s2} i \frac{\partial \theta_2}{\partial t} = -iT(n_{s1}n_{s2})^{\frac{1}{2}} (\cos \varphi - i \sin \varphi). \quad (6.41b)$$

Equating the real part and the imaginary part on both sides of Eq. 6.41a and Eq. 6.41b respectively gives,

$$\frac{1}{2} \frac{\partial n_{s1}}{\partial t} = T(n_{s1}n_{s2})^{\frac{1}{2}} \sin \varphi, \quad (6.42a)$$

$$n_{s1} \frac{\partial \theta_1}{\partial t} = -T(n_{s1}n_{s2})^{\frac{1}{2}} \cos \varphi, \quad (6.42b)$$

$$\frac{1}{2} \frac{\partial n_{s2}}{\partial t} = -T(n_{s1}n_{s2})^{\frac{1}{2}} \sin \varphi, \quad (6.42c)$$

$$n_{s2} \frac{\partial \theta_2}{\partial t} = -T(n_{s1}n_{s2})^{\frac{1}{2}} \cos \varphi. \quad (6.42d)$$

Subtracting Eq. 6.42c from Eq. 6.42a gives,

$$\frac{\partial(n_{s1} - n_{s2})}{\partial t} = 4T(n_{s1}n_{s2})^{\frac{1}{2}} \sin \varphi. \quad (6.43)$$

Multiplying both sides of Eq. 6.43 by the electron charge e and the length of the thin insulator l

gives,

$$el \frac{\partial(n_{s1} - n_{s2})}{\partial t} = J = 4elT(n_{s1}n_{s2})^{\frac{1}{2}} \sin \varphi = J_0 \sin \varphi, \quad (6.44)$$

where J is the super current density tunneling through the thin insulator as a function of the phase difference between the Cooper pairs on the two sides. This superconducting sandwich is called a Josephson junction. The DC Josephson effect is the basis for the AC Josephson effect and Macroscopic long-range quantum interference. [40, p. 290-p. 293]

6.4 Superconducting Quantum Interference Device

For a short Josephson junction in an applied field the relation between the tunnelling current density and the applied magnetic flux is,

$$J = J_0 \sin \varphi_0 \frac{\sin \left(\pi \frac{\Phi_{Junction}}{\Phi_0} \right)}{\pi \frac{\Phi_{Junction}}{\Phi_0}} [58, \text{p. 475}], \quad (6.45)$$

where J_0 is from Eq. 6.44. φ_0 is the phase difference of the Cooper pairs at some reference position on the junction. $\Phi_{Junction}$ is the applied flux through the effective area of the junction. Φ_0 is the flux quantum. Eq. 6.45 is called the Josephson junction diffraction equation, which is similar to the single-slit Fraunhofer diffraction equation in optics. [58, p. 475]

Consider a two-junction loop as shown in Fig. 6.5 [58, p. 479].

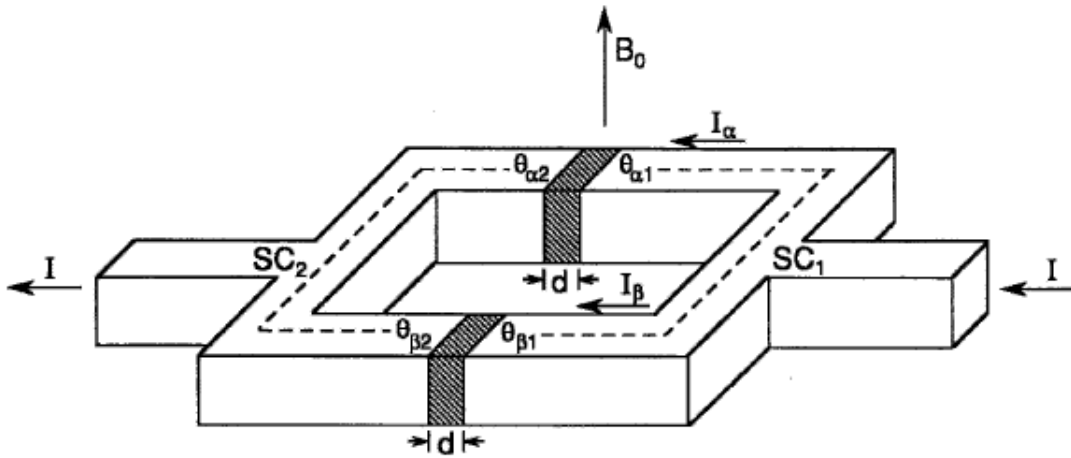


Figure 6.5: Two Josephson-junction loop in a applied field [58, p. 479]

If the two junctions are short enough and the current densities through them are equal, the total current density and the flux through the loop have the following relation,

$$J_{Total} = 2J_0 \left| \cos \left(\pi \frac{\Phi_{Loop}}{\Phi_0} \right) \right| \quad [58, \text{p. 479}]. \quad (6.46)$$

Eq. 6.46 is called the Josephson loop interference equation and is similar to Young's double-slit interference equation in optics. [58, p. 480]

If these two junctions have large enough area, since $\Phi_{app} = B_{app} \times area$, taking into account flux through both the loop and the junction areas and hence combining Eq. 6.45 and 6.46 we have,

$$J = 2J_0 \left| \cos \left(\pi \frac{\Phi_{Loop}}{\Phi_0} \right) \cdot \sin \varphi_0 \frac{\sin \left(\pi \frac{\Phi_{Junction}}{\Phi_0} \right)}{\pi \frac{\Phi_{Junction}}{\Phi_0}} \right|. \quad (6.47)$$

Eq. 6.47 is the Josephson loop diffraction equation, which is similar to the interference of Fraunhofer diffraction from two identical wide slits in optics. [58, p. 482]

A Superconducting Quantum Interference Device (SQUID) is shown in Fig. 6.6 [58, p. 485].

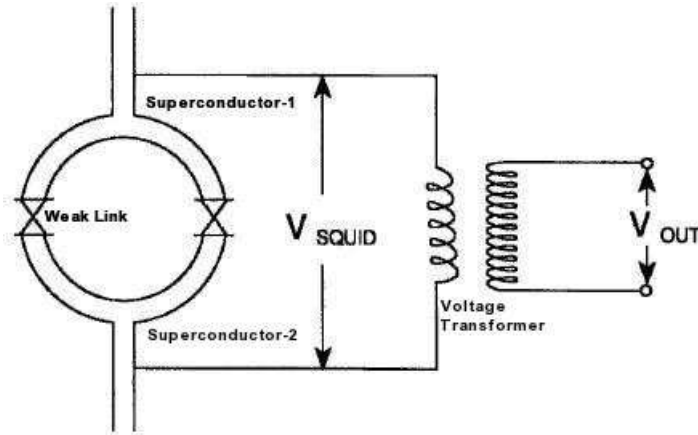


Figure 6.6: DC-SQUID [58, p. 485]

This is a DC-SQUID composed of a two Josephson-junction loop and a voltage transformer to output the signal. An AC-SQUID is composed of a single Josephson-junction loop coupled with an LC-tuned circuit. [58, p. 486]

6.5 Experimental Methods

The Quantum Design's Magnetic Property Measurement System (MPMS) was used for the low temperature magnetic measurements. The basic set up for detecting the magnetic response of samples is shown in Fig. 6.7 [59, p. 4-2].

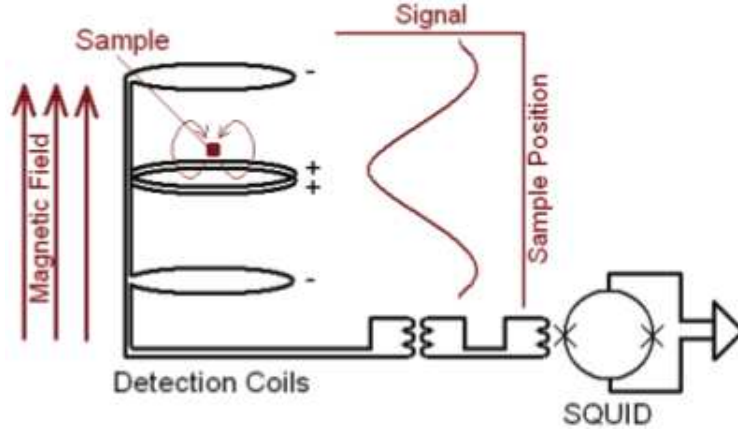


Figure 6.7: Basic set up for detecting signal [59, p. 4-2]

The detection coils are made of superconducting materials. The upper coil and the bottom coil are a single turn wound clockwise. The center coil has two turns wound counter-clockwise. This configuration is known as a second-order gradiometer, which can effectively reduce the noise. During the measurements a sample is oscillating through the superconducting detection coils. Hence the magnetic moments of the sample induce an electric current in the detection coils. Correspondingly the SQUID will output a voltage proportionally, which couples with the detection coils. The integration of output voltage with respect to the sample position is proportional to the magnetic moment. [60, p. 5-7, 10-11] Therefore the magnetization per unit mass can be calculated by,

$$M_{\text{mass}} = \frac{\mu}{m}, \quad (6.48)$$

where μ is the overall magnetic moment and m is the sample mass.

6.6 Experimental Results

The temperature-dependent and field-dependent DC magnetization measurements were made by Prof. Razavi at the Max Plank Institute for Solid State Research in Germany in the summer of 2011. The field direction was within the ab plane. The temperature dependent magnetization under 25 Oe and 50 Oe fields for the unannealed Sample1-2 is shown in Fig. 6.8.

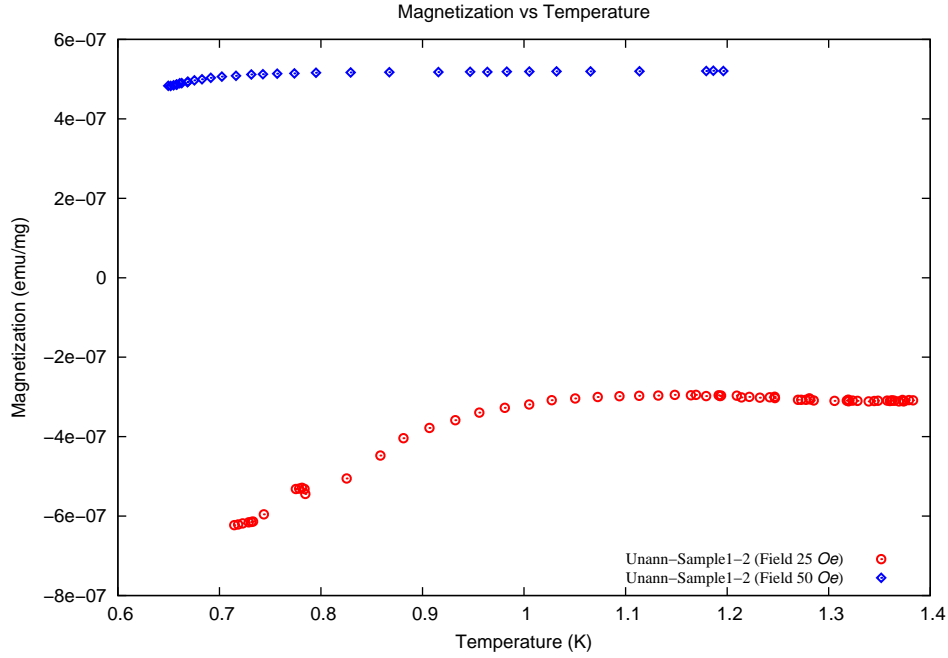


Figure 6.8: Temperature dependent DC magnetization under 25 Oe and 50 Oe field for unannealed Sample1-2

The temperature reached a lower limit of 0.7 K and only the onset of the superconducting transition was seen for both cases. For the same temperature range the magnetization for the 50 Oe field is positive while for the 25 Oe field it is negative, which is due to the diamagnetism of ^3He , in which the sample was immersed. For the 25 Oe field the onset of the SC transition is about 1 K while for the 50 Oe field it is suppressed down to about 0.8 K.

The temperature dependent magnetization under zero field for annealed Sample1-1 is shown in Fig. 6.9.

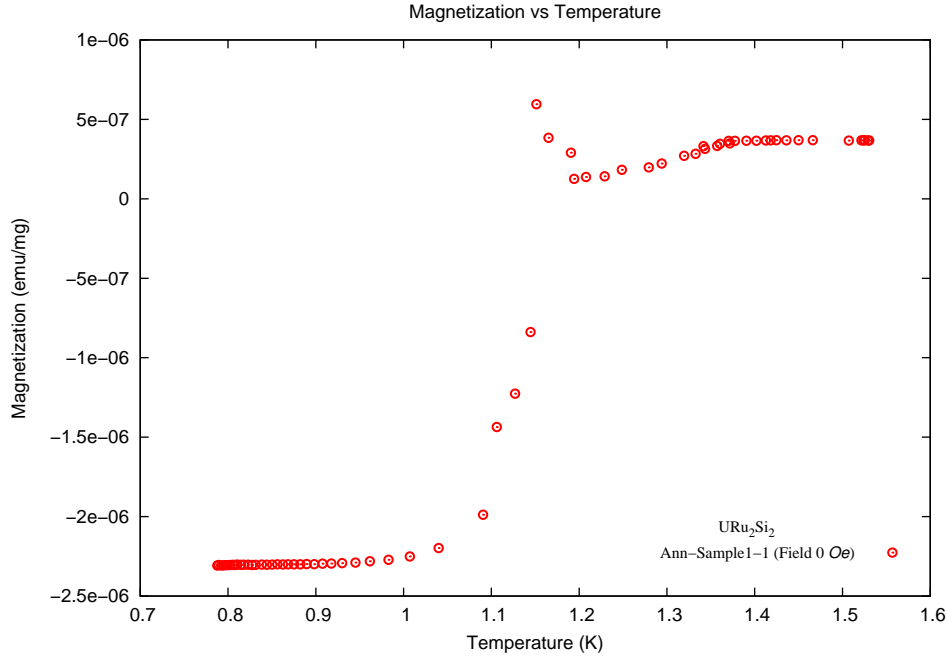


Figure 6.9: Temperature dependent DC magnetization under 0 Oe field for annealed Sample1-1

If T_c is defined as the temperature where $\frac{\partial M}{\partial T}$ is maximum, it is about 1.15 K. The onset of the SC transition is at about 1.4 K and the end of the SC transition is at about 0.9 K. Hence the transition width is about 0.5 K. The kink at about 1.35 K may be due to a double SC transition. Note that this feature is absent in Fig. 6.10 under the higher field of 25 Oe for the same sample. The sudden rise of the magnetization from about 1.2 K to about 1.15 K may be due to temperature oscillations during cooling rather than to a ferromagnetic impurity because this feature was also not observed in Fig. 6.10.

The temperature dependent DC magnetization under 25 Oe is shown in Fig. 6.10.

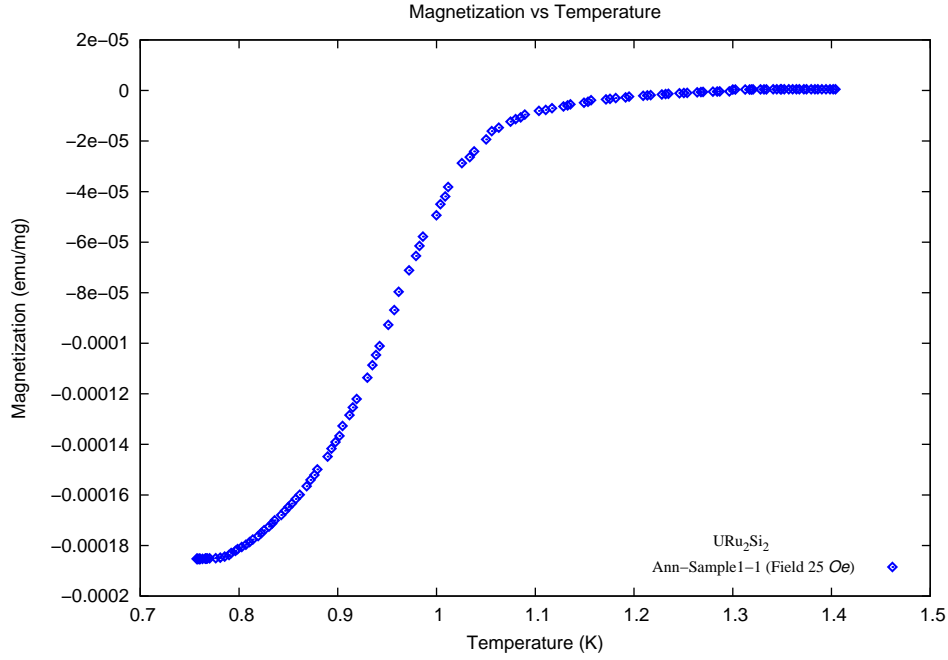


Figure 6.10: Temperature dependent DC magnetization under 25 Oe field

For the same definition T_c is about 0.95 K under the 25 Oe field. The onset of the SC transition is at about 1.3 K and the end of SC transition is at about 0.8 K. Hence the transition width is about 0.5 K the same as it was under zero field. However T_c , the onset of the SC transition and the end of the SC transition are suppressed down to lower temperature by 0.2 K, 0.1 K and 0.1 K respectively. The magnitude of the magnetization below the onset temperature of the SC transition is greater for the 25 Oe field than for zero field for the same temperature range, which may be because 25 Oe is below the lower critical field H_{c1} at any given temperature in this range and Eq. 6.2b applies.

The temperature dependent magnetizations of unannealed Sample1-2 and annealed Sample1-1 measured at 25 Oe are shown in Fig. 6.11.

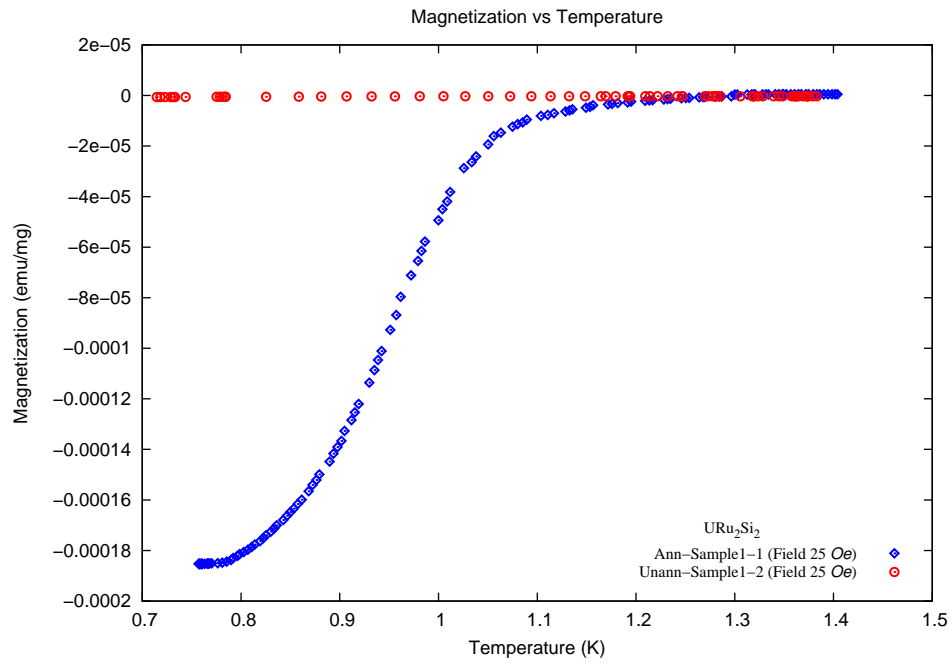


Figure 6.11: Temperature dependent DC magnetizations for unannealed Sample1-2 and annealed Sample1-1 under 25 Oe field

Obviously the annealing has induced superconductivity.

The field dependent DC magnetization at a temperature of 0.731 K up to 10^4 Oe for annealed Sample1-1 is shown in Fig. 6.12.

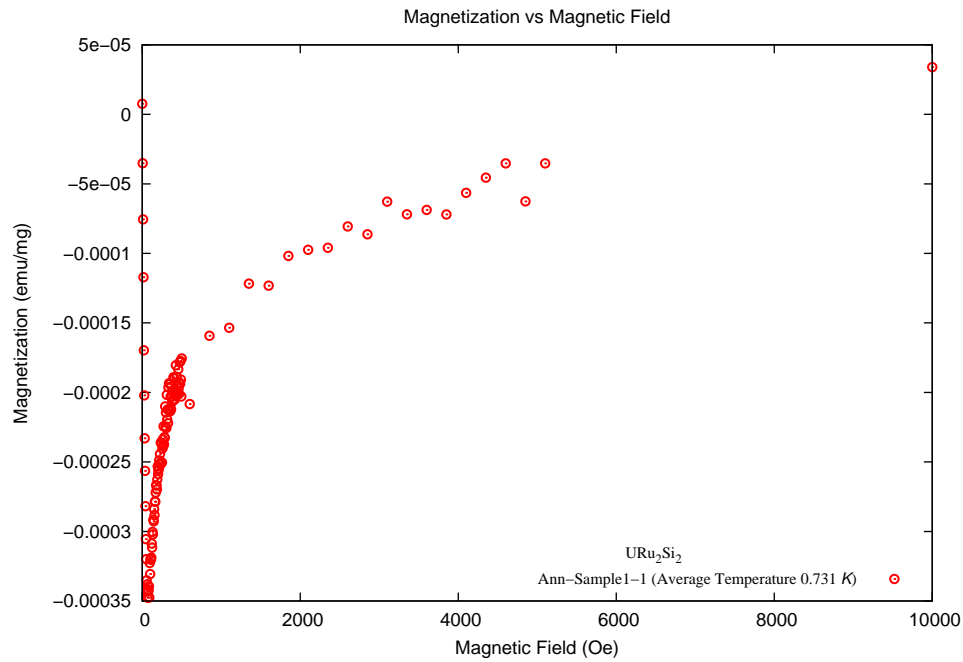


Figure 6.12: Field dependent DC magnetization up to 10^4 Oe field

This is a typical field dependent magnetization for a Type-II superconductor. Below the lower critical field H_{c1} perfect diamagnetism is exhibited in the Meissner state and its response to the applied field is given by Eq. 6.2b. Between H_{c1} and the upper critical field H_{c2} it is in the vortex state and its magnetization is still negative though the magnitude is reduced. Above H_{c2} it is in the normal state. The magnetization of the data point at 10^4 Oe is above zero. The low field region is shown in Fig. 6.13.

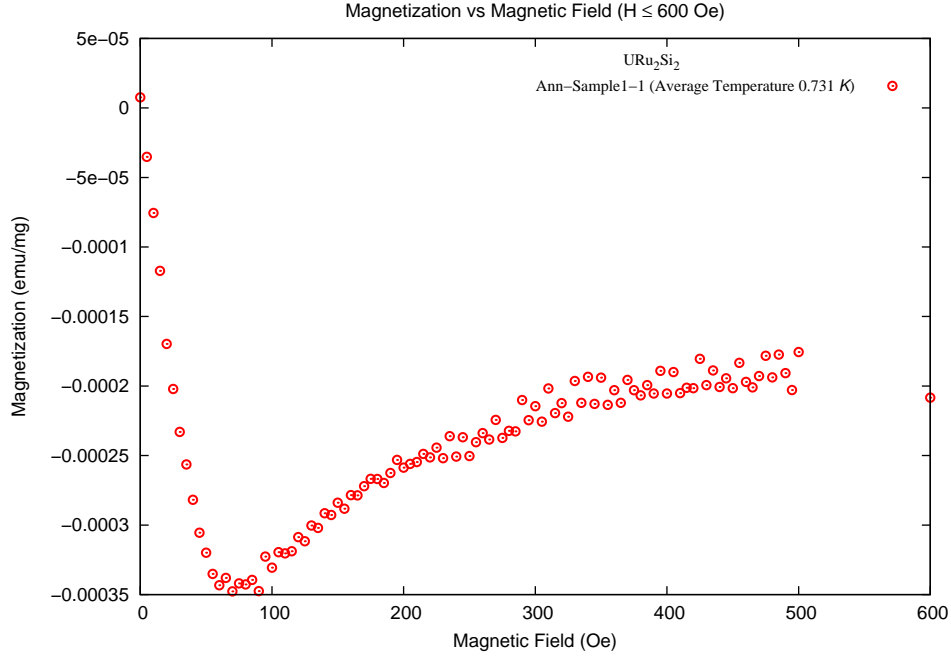


Figure 6.13: Field dependent DC magnetization up to 600 Oe field

The lower critical field H_{c1} is about 70 Oe at the temperature of 0.731 K without taking the demagnetization effect into account. The field at which the first magnetic flux penetrates from the edge of a sample, H_p , along the a-axis obtained by Okazaki *et al.* was about $0.6 \text{ mT} = 6 \text{ Oe}$ at 0.7 K, which had RRR over 700. Okazaki *et al.* determined H_{c1} along the a-axis as $1.15 \times H_p$. 1.15 is due to the demagnetization effect. [61] They calculated H_{c1} using the following formula for a platelet sample,

$$H_{c1} = \frac{H_p}{\tanh \sqrt{0.36b/a}} \quad [62]. \quad (6.49)$$

$\tanh \sqrt{0.36b/a}$ is the demagnetization factor, where a and b are the two dimensions of the surface which is parallel to the field direction. b is along the field direction and a is perpendicular to the field direction. Using the same formula the demagnetization factor of annealed Sample1-1 is

estimated to be 0.615 so the H_{c1} is $\frac{70 Oe}{0.615}$. Compared with the sample of Okazaki *et al.* the RRR of the annealed Sample1-1 is quite low. Crystal defects can pin the magnetic flux, which may retard the flux from penetrating into the sample, yielding a higher value of H_{c1} for the annealed Sample1-1. Note that in resistivity measurements for this sample the superconducting transition was only observed when it was mounted using five-minute epoxy (See Fig. 5.7c). This indicates that thermal bonding is extremely important. Also in order to obtain a measurable value of ρ , in the DC-resistivity measurements the applied current had to be relatively high, which increased the generated heat and therefore likely also suppressed the superconducting transition in those measurements.

Chapter 7

Conclusions

The resistivity of URu_2Si_2 was found to slowly increase from room temperature down to the coherence temperature T_{co} and then decrease drastically below T_{co} . A small λ shaped cusp appears at the Hidden Order temperature T_{HO} . These are in agreement with literature results.

The residual resistivity ratio RRR was found to increase after annealing. The resistivity was found to decrease only very slowly with decreasing temperature below 5 K and for all but two measurements didn't show the SC transition down to about 0.5 K. The one measurement showing most clearly the SC transition does not correspond to the sample with the highest RRR. For this measurement the sample was annealed and mounted using five-minute epoxy. Three factors were likely helpful in allowing the SC transition to be observed. For this sample though the annealing did not remove all kinds of defects effectively as demonstrated by the low RRR, it did likely remove certain defects which can destroy heavy fermion superconductivity. Second, the mounting medium, five-minute epoxy, has better thermal conductivity than double-sided tape does. Third, its small size and the small interface area between the contact and the sample surface effectively reduced the generated heat due to the applied current. For the same annealed samples the RRR for samples mounted with five-minute epoxy or VGE-7031 was higher than the RRR for samples mounted using double-sided tape likely due to the fact that a lower temperature and hence lower residual resistivity could be reached in the former cases.

The magnitude of the resistivity was found to be enhanced after annealing in some samples. The enhancement of resistivity after annealing was also found by Fåk *et al.* [34]. The resistivity was lowered after annealing for other samples likely because the annealing for these samples was not effective enough, which can be deduced by comparing the RRR for measurements of the annealed samples and the unannealed sample. In the former case RRR increases substantially after annealing while in the latter it is virtually unchanged.

A plot of the Exponent C of the temperature dependence of the resistivity below the Hidden Order transition vs RRR compared with those of Matsuda *et al.* showed that C for low RRR approaches 2, for medium RRR approaches 1 and for high RRR approaches 1.5.

Our data of the Hidden Order temperature T_{HO} vs RRR together with those of Matsuda *et al.* showed that T_{HO} for low RRR has a sharp dip at $RRR \approx 10$ and that T_{HO} for high RRR saturates to some higher temperature as RRR increases. We further found that as T_{HO} drops near $RRR \approx 10$, its transition width ΔT_{HO} increases significantly beyond the value found by Matsuda *et al.* at large RRR. [2]

The superconducting transition was easier to be observed using DC magnetization measurements. A higher field was found to suppress the SC transition to lower temperatures for both the unannealed sample and the annealed sample. The annealing was found to enhance the SC transition temperature when measurements were taken under the same field, namely 25 Oe. The magnetization of the annealed sample exhibits the typical field dependent magnetization for a Type-II superconductor. H_{c1} was found to be higher than literature values for samples with much higher RRR [61]. This may be due to the fact that crystal defects in our sample with a low value of RRR can pin the magnetic flux and hence retard the flux from penetrating.

A logical next step would be to measure the optical properties of URu₂Si₂ to temperatures below the T_c of the SC transition. As the electronic band structure evolves with temperature, the optical reflectivity of the sample, and in particular the optical response of the electrons, can reveal information about the scattering rate, the charge carrier concentration, the effective mass and the excitation gap in the Hidden Order phase and notably in the superconducting state, which has not yet been investigated. Additionally it will be of interest to examine the effect of the onset of superconductivity on the resonance frequencies of the lattice vibrations. Such information is certainly important to further the understanding of the temperature dependent evolution of the localized and itinerant electrons as well as their hybridization.

Bibliography

- [1] J. A. Mydosh and P. M. Oppeneer, “*Colloquium*: Hidden order, superconductivity, and magnetism: The unsolved case of URu₂Si₂,” *Reviews of Modern Physics*, vol. 83, pp. 1301–1322, 2011.
- [2] T. D. Matsuda, E. Hassinger, D. Aoki, V. Taufour, G. Knebel, N. Tateiwa, E. Yamamoto, Y. Haga, Y. Ōnuki, Z. Fisk, and J. Flouquet, “Details of Sample Dependence and Transport Properties of URu₂Si₂,” *arXiv.org*, vol. 1109.1953v1, pp. 1–10, 2011.
- [3] A. L. Dawson, W. R. Datars, J. D. Garrett, and F. S. Razavi, “Electric transport in URu₂Si₂,” *J. Phys: Condens. Matter*, vol. 1, pp. 6817–6828, 1989.
- [4] H. Harima, K. Miyake, and J. Flouquet, “Why the Hidden Order in URu₂Si₂ Is Still Hidden — One Simple Answer,” *Journal of the Physical Society of Japan*, vol. 79, pp. 033705–1–033705–4, 2010.
- [5] R. Okazaki, T. Shibauchi, H. J. Shi, Y. Haga, T. D. Matsuda, E. Yamamoto, Y. Onuki, H. Ikeda, and Y. Matsuda, “Rotational Symmetry Breaking in the Hidden-Order Phase of URu₂Si₂,” *Science*, vol. 331, pp. 439–442, 2011.
- [6] Polymer Synthesis & Physics Laboratory, “Crystallography.” <http://www.postech.ac.kr/chem/mree/study/crystallography.pdf>, 2011.
- [7] On the Cutting Edge - Professional Development for Geoscience Faculty, “Symmetry Elements.” <http://serc.carleton.edu/NAGTWorkshops/mineralogy/xtlsymmetry/elements.html>, 2011.

-
- [8] T. T. M. Palstra, A. A. Menovsky, J. van den Berg, A. J. Dirkmaat, P. H. Kes, G. J. Nieuwenhuys, and J. A. Mydosh, “Superconducting and Magnetic Transition in the Heavy-Fermion System URu₂Si₂,” *Phys. Rev. Lett.*, vol. 55, pp. 2727–2730, 1985.
- [9] P. G. Niklowitz, C. Peiderer, T. Keller, M. Vojta, Y.-K. Huang, and J. A. Mydosh, “Parasitic Small-Moment Antiferromagnetism and Nonlinear Coupling of Hidden Order and Antiferromagnetism in URu₂Si₂ Observed by Larmor Diffraction,” *Phys. Rev. Lett.*, vol. 104, pp. 106406–1–106406–4, 2010.
- [10] T. T. M. Palstra, A. A. Menovsky, and J. A. Mydosh, “Anisotropic electrical resistivity of the magnetic heavy-fermion superconductor URu₂Si₂,” *Phys. Rev. B*, vol. 33, pp. 6527–6530, 1986.
- [11] N. P. Butch, J. R. Jeffries, S. Chi, J. B. Leão, J. W. Lynn, and M. B. Maple, “Antiferromagnetic critical pressure in URu₂Si₂ under hydrostatic conditions,” *Phys. Rev. B*, vol. 82, pp. 060408–1–060408–4, 2010.
- [12] H. Amitsuka, K. Matsuda, I. Kawasaki, K. Tenya, M. Yokoyama, C. Sekine, N. Tateiwa, T. Kobayashi, S. Kawarazaki, and H. Yoshizawa, “Pressure-temperature phase diagram of the heavy-electron superconductor URu₂Si₂,” *Journal of Magnetism and Magnetic Materials*, vol. 310, pp. 214–220, 2007.
- [13] F. Bourdarot, E. Hassinger, S. Raymond, D. Aoki, V. Taufour, L.-P. Regnault, and J. Flouquet, “Precise Study of the Resonance at Q₀ = (1,0,0) in URu₂Si₂,” *Journal of the Physical Society of Japan*, vol. 79, pp. 064719–1–064719–8, 2010.
- [14] F. Bourdarot, E. Hassinger, S. Raymond, D. Aoki, V. Taufour, and J. Flouquet, “Temperature Dependence of Energy Gap in the Superconducting State in URu₂Si₂,” *Journal of the Physical Society of Japan*, vol. 79, pp. 094706–1–094706–4, 2010.
- [15] H. Amitsuka, M. Yokoyama, S. Miyazaki, K. Tenya, T. Sakakibara, W. Higemoto, K. Nagamine, K. Matsuda, Y. Kohori, and T. Kohara, “Hidden order and weak antiferromagnetism in URu₂Si₂,” *Physica B*, vol. 312–313, pp. 390–396, 2002.

-
- [16] D. A. Bonn, J. D. Garrett, and T. Timusk, “Far-Infrared Properties of URu_2Si_2 ,” *Phys. Rev. Lett.*, vol. 61, pp. 1305–1308, 1988.
- [17] J. Levallois, F. Lévy-Bertrand, M. K. Tran, D. Stricker, J. A. Mydosh, Y.-K. Huang, and D. van der Marel, “Hybridization gap and anisotropic far-infrared optical conductivity of URu_2Si_2 ,” *Phys. Rev. B*, vol. 84, pp. 184420–1–184420–6, 2011.
- [18] Martin Dressel and George Grüner, *Electrodynamics of Solids*. CAMBRIDGE UNIVERSITY PRESS, 2nd ed., 2003.
- [19] M. B. Maple, J. W. Chen, Y. Dalichaouch, T. Kohara, C. Rossel, M. S. Torikachvili, M. W. McElfresh, and J. D. Thompson, “Partially Gapped Fermi Surface in the Heavy-Electron Superconductor URu_2Si_2 ,” *Phys. Rev. Lett.*, vol. 56, pp. 185–188, 1986.
- [20] Department of Materials Science and Engineering, University of Virginia, “Imperfections in Solids.” <http://people.virginia.edu/~lz2n/mse209/Chapter4c.pdf>, 2010.
- [21] S. L. Kakani and Amit Kakani, *MATERIAL SCIENCE*. New Age International (P) Ltd., Publishers, 1st ed., 2004.
- [22] William D. Callister, Jr. and David G. Rethwisch, *Materials Science and Engineering An Introduction*. John Wiley & Sons, Inc., 8th ed., 2010.
- [23] VL Ginzburg and EA Andryushin, *Superconductivity*. World scientific Publishing Co. Pte. Ltd., Revised ed., 2004.
- [24] WIKIPEDIA, “Burgers vector.” http://en.wikipedia.org/wiki/Burgers_vector, 2011.
- [25] WIKIPEDIA, “Grain boundary.” http://en.wikipedia.org/wiki/Grain_boundary, 2011.
- [26] Prof. Dr. Helmut Fll, “Stacking Faults.” http://www.tf.uni-kiel.de/matwis/amat/def_en/kap_5/backbone/r5_4_1.html, 2008.
- [27] WIKIPEDIA, “Czochralski Process.” http://en.wikipedia.org/wiki/Czochralski_process, 2012.

-
- [28] T. D. Matsuda, D. Aoki, S. Ikeda, E. Yamamoto, Y. Haga, H. Ohkuni, R. Settai, and Y. Ōnuki, “Super Clean Sample of URu₂Si₂,” *Journal of the Physical Society of Japan*, vol. 77, pp. 362–364, 2008.
- [29] Reza Abbaschian, Lara Abbaschian and Robert E. Reed-Hill, *PHYSICAL METALLURGY PRINCIPLES*. Cengage Learning, 4th ed., 2009.
- [30] R.E. Smallman and A.H.W. Ngan, *PHYSICAL METALLURGY AND ADVANCED MATERIALS*. Elsevier, 7th ed., 2007.
- [31] Vadim S. Zolotarevsky and Nikolai A. Belov and Michael V. Glazoff, *Casting Aluminum Alloys*. Elsevier Ltd., 1st ed., 2007.
- [32] George E. Totten, *STEEL HEAT TREATMENT HANDBOOK*. Taylor & Francis Group, LLC, 2nd ed., 2007.
- [33] A. A. Menovsky, A. C. Moleman, G. E. Snel, T. J. Gortenmulder, H. J. Tan, and T. T. M. Palstra, “CRYSTAL GROWTH AND CHARACTERIZATION OF MT₂Si₂ TERNARY INTERMETALLICS (M=U, RE AND T=3d, 4d, 5d TRANSITION METALS,” *Journal of Crystal Growth*, vol. 79, pp. 316–321, 1986.
- [34] B. Fåk, C. Vettier, J. Flouquet, F. Bourdarot, S. Raymond, A. Vernière, P. Lejay, P. Boutrouille, N. Bernhoeft, S. Bramwell, R. Fisher, and N. Phillips, “Influence of sample quality on the magnetic properties of URu₂Si₂,” *Journal of Magnetism and Magnetic Materials*, vol. 154, pp. 339–350, 1996.
- [35] T. Honma, Y. Haga, E. Yamamoto, N. Metoki, Y. Koike, H. Ohkuni, N. Suzuki, and Y. Ōnuki, “Interplay between Magnetism and Superconductivity in URu₂Si₂ Studied by Neutron Scattering Experiments,” *Journal of the Physical Society of Japan*, vol. 68, pp. 338–341, 1999.
- [36] Infrared Laboratories, Inc., “Cryogenic Solutions, Closed Cycle Dewars, Helium 3 Refrigerator - H3R Series.” http://www.infraredlaboratories.com/H3R_Refrigerator.html, 2010.
- [37] Department of Physics, Brock University, “Helium 3 Refrigerator Outer View.” <http://www.physics.brocku.ca/>, 2011.

-
- [38] Stanislav Očadlík, “Far Infrared Spectroscopy of Heavy Fermion Superconductor CeCoIn₅,” Master’s thesis, Brock University, Canada, 2004.
- [39] Brad Dempsie, “Far Infrared Reflectance Along the C-axis of the Charge Stripe Superconductor La_{1.875}Ba_{0.125}CuO₄,” Master’s thesis, Brock University, Canada, 2010.
- [40] Charles Kittel, *Introduction to Solid State Physics*. John Wiley & Sons, Inc, 8th ed., 2005.
- [41] GUY K. WHITE, *Experimental Techniques in Low-Temperature*, p. 9. CLARENDON PRESS • OXFORD, 3rd ed., 1979.
- [42] Daijiro Yoshioka, *Statistical Physics An Introduction*. Springer, 1st ed., 2007.
- [43] E. Brian Smith, *Basic Chemical Thermodynamics*, p. 46. Imperial College Press, 5th ed., 2004.
- [44] L. J. van der PAUW, “A METHOD OF MEASURING SPECIFIC RESISTIVITY AND HALL EFFECT OF DISCS OF ARBITRARY SHAPE,” *Philips Research Reports*, vol. 13, pp. 1–9, 1958.
- [45] L. J. van der PAUW, “A METHOD OF MEASURING THE RESISTIVITY AND HALL COEFFICIENT ON LAMELLAE OF ARBITRARY SHAPE,” *Philips Technical Review*, vol. 20, pp. 220–224, 1958.
- [46] Mark Lundstrom, *Fundamentals of Carrier Transport*, p. 187. CAMBRIDGE UNIVERSITY PRESS, 2nd ed., 2000.
- [47] Gerald Dennis Mahan, *APPLIED MATHEMATICS*. Springer, 1st ed., 2002.
- [48] Lake Shore Cryotronics, Inc., “Technical Specifications.” <http://www.lakeshore.com/products/Cryogenic-Accessories/Varnish/Pages/Specifications.aspx>, 2012.
- [49] National Instruments, “GPIB (IEEE 488).” <http://www.ni.com/gpib/>, 2012.
- [50] Quantum Design, “SOFTWARE UPGRADES.” <http://www.qdusa.com/techsupport/softwareUpgrades.html>, 2011.

-
- [51] L. K. J. Vandamme, “Noise as a Diagnostic Tool for Quality and Reliability of Electronic Devices,” *IEEE TRANSACTIONS ON ELECTRON DEVICES*, vol. 41, pp. 2176–2187, 1994.
- [52] Terry M. Tritt, *Thermal Conductivity: Theory, Properties, and Applications*. Kluwer Academic/Plenum Publishers, 1st ed., 2004.
- [53] Paul L. Rossiter, *The electrical resistivity of metals and alloys*. Cambridge University Press, 1st ed., 1987.
- [54] The Open University, “Superconductivity.” <http://openlearn.open.ac.uk/mod/oucontent/view.php?id=398540>, 2011.
- [55] J. B. KETTERSON and S. N. SONG, *Superconductivity*. CAMBRIDGE UNIVERSITY PRESS, 1st ed., 1999.
- [56] Michael Tinkham, *INTRODUCTION TO SUPERCONDUCTIVITY*. McGraw-Hill, Inc, 2nd ed., 1996.
- [57] Harry B. Radousky, *Magnetism in Heavy Fermion Systems*. World Scientific Publishing Co. Pte. Ltd., 1st ed., 2000.
- [58] Charles P. Poole, Jr., Horacio A. Farach, Richard J. Creswick and Ruslan Prozorov, *Superconductivity*. Elsevier Ltd., 2nd ed., 2007.
- [59] Quantum Design, *SQUID VSM User’s Manual*. Quantum Design Inc., 7th ed., 2009.
- [60] Mike Mcelfresh, *Fundamentals of Magnetism and Magnetic Measurements*. Quantum Design Inc., 1st ed., 1994.
- [61] R. Okazaki, M. Shimozawa, H. Shishido, M. Konczykowski, Y. Haga, T. D. Matsuda, E. Yamamoto, Y. Ōnuki, Y. Yanase, T. Shibauchi, and Y. Matsuda, “Anomalous Temperature Dependence of Lower Critical Field in Ultraclean URu₂Si₂,” *Journal of the Physical Society of Japan*, vol. 79, pp. 084705–1–084705–7, 2010.
- [62] E. H. Brandt, “Irreversible magnetization of pin-free type-II superconductors,” *Phys. Rev. B*, vol. 60, pp. 11939–11942, 1999.

-
- [63] Y. Arita, K. Terao, S. Mitsuda, Y. Nishi, T. Matsui, and T. Nagasaki, “Thermoelectric properties of URu_2Si_2 and $\text{U}_2\text{Ru}_3\text{Si}_5$,” *Journal of Nuclear Materials*, vol. 294, pp. 206–208, 2001.
- [64] J. Franse, A. Menovsky, A. de Visser, J. van den Berg, and G. J. Nieuwenhuys, “Crystal-field effects in the magnetic and thermal properties of URu_2Si_2 ,” *Journal of Applied Physics*, vol. 61, pp. 3383–3384, 1987.
- [65] J. A. Janik, H. D. Zhou, Y.-J. Jo, L. Balicas, G. J. MacDougall, G. M. Luke, J. D. Garrett, K. J. McClellan, E. D. Bauer, J. L. Sarrao, Y. Qiu, J. R. D. Copley, Z. Yamani, W. J. L. Buyers, and C. R. Wiebe, “Itinerant spin excitations near the hidden order transition in URu_2Si_2 ,” *Journal of Physics: Condensed Matter*, vol. 21, pp. 192202–1–192202–4, 2009.
- [66] A. R. Schmidt, M. H. Hamidian, P. Wahl, F. Meier, A. V. Balatsky, J. D. Garrett, T. J. Williams, G. M. Luke, and J. C. Davis, “Imaging the Fano lattice to ‘hidden order’ transition in URu_2Si_2 ,” *Nature*, vol. 465, pp. 570–576, 2010.
- [67] P. Aynajian, E. H. da Silva Neto, C. V. Parker, Y. Huang, A. Pasupathy, J. Mydosh, and A. Yazdani, “Visualizing the formation of the Kondo lattice and the hidden order in URu_2Si_2 ,” *PNAS*, vol. 107, pp. 10383–10388, 2010.